SISSA **ISAS**

SCUOLA INTERNAZIONALE SUPERIORE DI STUDI AVANZATI
INTERNATIONAL SCHOOL FOR ADVANCED STUDIES

Numerical techniques for the study of wetting on rough surfaces and contact angle hysteresis

Thesis submitted for the degree of
\Doctor Philosophi "

Supervisor
Prof. Antonio DeSimone

Candidate
Livio Fedeli

October 2011

Il presente lavoro costituisce la tesi presentata da Livio Fedeli, sotto la direzione di ricerca del Prof. Antonio DeSimone, al fine di ottenere l'attestato di ricerca post-universitaria *Doctor Philosophiae in Matematica Applicata* presso la S.I.S.S.A.. Ai sensi dell' art. 18, comma 3, dello Statuto della Sissa pubblicato sulla G.U. no 62 del 15.03.2001, il predetto attestato è equipollente al titolo di *Dottore di Ricerca in Matematica*.

Trieste, Ottobre 2011.

Contents

Introduction **i**

1 Capillarity on rough surfaces: homogenization approach **1**

1.1 Mathematical statement of the problem 1

1.1.1 The homogenization formula 1

1.1.2 The analytical statement 3

1.2 Analysis of the problem 4

1.2.1 Existence of a solution 5

1.2.2 Basic regularity properties 5

1.2.3 Equivalent convex formulation 7

1.2.4 Comparison 8

1.2.5 Stability for the cell problem 9

1.3 Numerical Approximation 11

1.3.1 Error estimates 11

1.3.2 The minimization scheme: *ADMM* 13

1.3.3 Finite element discretization 14

1.3.4 Numerical implementation 17

1.4 Examples 20

2 The phase field approach to wetting **25**

2.1 The theoretical review 25

2.2 Numerical implementation 28

2.2.1 The basic numerical scheme 28

2.2.2 A sufficient condition for numerical stability 29

2.2.3 Adaptive mesh refinement 31

2.3 Metastability induced by surface roughness: fakir drops 32

3 Hysteresis of the contact angle **37**
3.1 A phenomenological model for contact angle hysteresis 37
3.2 Vertical plate experiments 42

4 Evaporating droplet on pillars: quasi-Newton methods and continuation methods **49**
4.1 Motivations 49
4.2 Numerical formulation of the problem 53
4.2.1 The Newton method 53
4.2.2 The proposed method 57
4.2.3 Nonlinear systems and unconstrained minimization problem . 60
4.3 The Continuation method 61
4.3.1 Introduction to the scheme 61
4.3.2 Application to quasi-static evolution of droplets 63
4.4 The multigrid structure and SAMRAI 64
4.5 Numerical examples 67

A A brief introduction to BV functions **73**
A.1 Definition 73
A.1.1 An equivalent definition 74
A.1.2 Main properties of the total variation 74
A.1.3 Functions with bounded variation 75
A.2 The perimeter. Sets with finite perimeter 77
A.2.1 Definition, and inequality 77
A.2.2 The reduced boundary, and a generalization of Green's formula 78
A.2.3 The isoperimetric inequality 79
A.2.4 The coarea formula 79
A.3 The derivative of a BV function 80

B Details on the multigrid architecture **85**

Introduction

This thesis is devoted to the study of mathematical and numerical techniques applied to the investigation of the physical phenomena of wetting on rough surfaces and the hysteresis of the static contact angle. In particular, what we have tried to show in this work, is that variational methods coupled with sophisticated numerical schemes for the solution of partial differential equations can provide satisfactory tools for the prediction on the behaviour of several experiments that can be compared with real ones driven in laboratory.
The theory of capillarity and its application to the prediction of equilibrium shapes, of fluid drop, soap films and soap bubbles have been the source of deep problems and spectacular results across disciplinary boundaries for over two centuries, see [16, 26] and [48]. Observations led in nature have picked out that water repellency is a property owned by several materials which makes water hardly stick to them (classical example is the one of the lotus flower leaves); however the natural hydrophobicity/hydrophilicty of a material can be also artificially enhanced even by simple operations (for example a piece of glass that is passed through the yellow part of a flame will be covered by a thin soot layer that prevents small drops to collapse on it). Heterogeneities at microscopic scale, like chemical patterning of the solid, microasperities and dirt, can surprisingly modify the wetting properties of the materials leading to a dramatically amplification of the expected behaviour. The mechanism for which these phenomena are possible relies on the pinning of the liquid/air interface at the level of the contact line with the solid: the presence of an obstacle gives rise to resistance forces that for instance prevent a drop which is increasing its volume

from advancing. The presence of the frictional forces is even more evident in our daily experience: rain drops are able to stick and stand in equilibrium on tilted glass surfaces such as windshields and window panes till gravity does not exceed the pinning resistance. These few examples suggest the study of a topic worthy of special

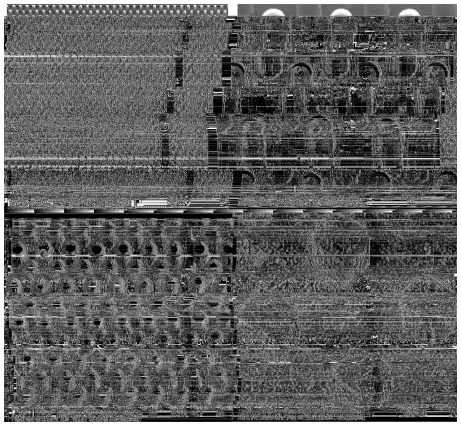

Figure 1: *A thin glassy polymer film covered by a regular array of pillars, as seen by scanning electron microscopy (SEM).* [60]

consideration: metastability, namely, the ability of liquid globules to exhibit stable equilibrium shape that are not minimizers of the capillary energy. A consequence of the existence of metastable states is the possibility of multiple equilibrium under the same external conditions, therefore a drop resting on a macroscopically flat substrate can exhibit a static contact angle that varies in a range: this phenomenon is called *hysteresis of the contact angle*, and reflects the fact that if we think of driving an evolutionary experiment, the equilibrium configuration at the intermediate steps does not depend only on (the same) external conditions, but is influenced also by the path of the evolution. Maybe fakir drops are the most striking example of metastability states: a drop gently deposited on a bed of micro-pillars can be in a stable equilibrium while resting only on the top of the asperities (Cassie-Baxter state) and air remains trapped in the cavities formed by the pillars. If the asperities are very tall, this is the state of minimal capillary energy; this state can be recovered (provided that the radius of the globule is large enough) also when the energetically favorable configuration is the one in which the liquid is in complete contact with the substrates (Wenzel state); however, if the drop is allowed to reduce volume by evaporation, then it falls down. Unfortunately classical theory of capillarity is no longer able to describe properly these new issues, and it has to be integrated in a proper way.

The first part of this project collects the studies about wetting phenomena on rough surfaces; in particular two different variational strategies are described: the first one is a homogenization approach that reduces the problem to determine the

macroscopic contact angle to a cell problem. The second one is a phase field approach, that characterizes the geometry of a drop by the use of a *phase function*; supplying suitable modifications, phase field is a valid model in which the presence of friction can be naturally embedded.

Homogenization is a powerful technique that captures the asymptotic behaviour of problems with increasingly oscillating solutions [9]; in particular it can be applied for the description of static phenomena involving the study of minimum points of some energy functional whose energy density is periodic on a very small scale. In the case of minimum problems of integral type, computing the Γ-limit allows to obtain the " effective" behaviour of these problems by means of "averaged" quantities.

The effect of microscopic surface roughness on the macroscopic angle is easily understood if one realizes that the actual (microscopic) area of the contact may differ from the one that is apparent at the macroscopic scale. Therefore in order to measure interfacial energies correctly within a macroscopic model, it is necessary to perform renormalization of the quantities that provide the correct value for the energy per unit macroscopic area.

While describing metastable states and accounting for contact angle hysteresis in contact line dynamics are still quite challenging, the effect of roughness on the macroscopic contact angle exhibited by energy minimizing capillary drops is well understood, at least in principle. Following Gauss variational formulation of the problem of capillarity, the shape L of a liquid drop of prescribed volume $\mathcal{V}$, sitting on a substrate S and surrounded by vapor environment, is obtained by minimizing

$$E(L) = \sigma_{SL}|\Sigma_{SL}| + \sigma_{SV}|\Sigma_{SV}| + \sigma_{LV}|\Sigma_{LV}| \tag{1}$$

where Σ_{XY} is the interface between phases X and Y, $|\Sigma_{XY}|$ is its area, and σ_{XY} the corresponding interfacial energy density (surface tension). Minimizers of (1) satisfy Laplace's law and Young's law on the contact angle

$$\cos\theta = \frac{\sigma_{SV} - \sigma_{SL}}{\sigma_{LV}}. \tag{2}$$

It has been shown in [1] that, if the rough solid surface is an ϵ-periodic perturbation S_ϵ of a flat surface S, converging to S as $\epsilon \to 0$ (i.e., in the limit in which the scale of roughness is vanishingly small compared to the true size of drop), and if one defines

$$L_\epsilon = \operatorname*{argmin}_{|L|=\mathcal{V}} E_\epsilon(L) \tag{3}$$

$$E_\epsilon = \sigma_{SL}|\Sigma^\epsilon_{SL}| + \sigma_{SV}|\Sigma^\epsilon_{SV}| + \sigma_{LV}|\Sigma_{LV}| \tag{4}$$

then in the limit $\epsilon \to 0$, one has that E_ϵ Γ-converges to the homogenized energy

$$E^{hom} = \sigma_{SL}^{hom}|\Sigma_{SL}| + \sigma_{SV}^{hom}|\Sigma_{SV}| + \sigma_{LV}|\Sigma_{LV}| \tag{5}$$

where σ_{SL}^{hom} and σ_{SV}^{hom} are obtained from suitable cell formulas and are further discussed below, and L_ϵ converges towards L which is given by

$$L = \underset{|L|=\mathcal{V}}{\operatorname{argmin}} E^{hom}(L). \tag{6}$$

In particular the macroscopic contact angle θ^{hom} satisfies

$$\cos\theta^{hom} = \frac{\sigma_{SV}^{hom} - \sigma_{SL}^{hom}}{\sigma_{LV}}. \tag{7}$$

The renormalized surface tension σ_{SV}^{hom} (respectively σ_{SL}^{hom}), represents the minimal energy per unit macroscopic area for a transition layer between the microscopically rough solid and the vapor phase (respectively, the liquid phase). The physical reason why the renormalization is necessary is that, for example, the minimal energy transition between a sufficiently rough solid surface and the liquid phase may be realized by a composite interface in which the troughs near the bottom of the asperities may be filled with vapor. The coefficients σ_{SV}^{hom} and σ_{SL}^{hom} can be characterized in principle as the solutions of well defined variational problems, see Chapter §1. The discussion of a numerical algorithm by which these quantities and hence, by (7), θ^{hom} can be computed for a periodic rough surface of arbitrary complexity is contained in a work [C] developed in collaboration with Prof. Antonin Chambolle and Dr. Simone Cacace. The geometric formulation of the problem is replaced by an equivalent analytical one that counts for the minimization of a new energy in which a *Total variation* term is included. In particular the numerical estimate of the minimum value of this energy will be the cosine of the static (macroscopic) contact angle.

Total variation has been introduced for image denoising and reconstruction and it has revealed particularly efficient because of its capability in preserving the natural discontinuities of an image without the introduction of blurring diffusion. In our case it represents a good choice to be used for the modelization of the cell problem since our task is the identification of a certain set by means its characteristic function; as in the case of image reconstruction, the introduction of diffusivity around the jump set of the solution affects dramatically the accuracy on the right calculation of the energy minimum value, that is the main goal to be achieved. The lack of simple stationarity conditions in the analytical formulation of the cell problem, requires

for the use of numerical algorithms for the minimization of convex functionals, that belong to the family of the augmented Lagrangian methods..

The work on the phase field model is the continuation of the previous research by Dr. Alessandro Turco, done under the supervision of Prof. De Simone, and the results obtained are contained in a Symposium Volume [A] and in a journal paper [B]. The main reason to resorting to a phase field model is to be able to follow merging and splitting of drops, which occur naturally in wetting problems. Furthermore, diffuse interface models have received renewed attention for the simulation of multi-phase and multi-component fluids because different physical effects can be modeled by a suitable modification of the free energy [14]. The classical geometrical formulation of the problem, in which the task of minimizing the energy stored at the interfaces between solid, liquid and air gives rise to a problem of the iso-perimetric type,, is replaced by the description of the shape of the drop through the use of a phase function ϕ that takes the value 1 in the liquid phase, the value 0 in the surrounding vapor, and spans the whole $[0, 1]$ interval in a liquid-vapor transition region. For wetting problems, the capillary energy (1) is replaced by an ϵ-regularized version

$$E_\epsilon(\phi) = \int_\Omega \left(\epsilon |\nabla \phi|^2 + \frac{1}{\epsilon} W(\phi) + \lambda \phi \right) dx \tag{8}$$

where λ is a Lagrange multiplier for the matching of the volume constraint associated with the value that the drop prescribes. The equilibrium shape of the drop is recovered by setting up a steepest descent dynamics

$$\frac{\partial \phi(\tau, x)}{\partial \tau} = -\nabla E_\epsilon(\phi) \tag{9}$$

that leads, as ϵ tends to 0, ϕ toward a critical point of energy (8). In the limit as ϵ tends to 0, one recovers the solution of the capillary problem, with sharp interfaces between the phases [41, 56]. The presence of the solid is modeled by imposing suitable (Dirichlet or Neumann) boundary condition on the phase function ϕ, which are tuned in order to reproduce the Young contact angle (2). For the numerical resolution of the discrete problem deriving from (9), we present an explicit Euler method, coupled with a splitting strategy for the calculation of the Lagrange multiplier λ. Within this scheme, we begin also the description of mesh refinement techniques and C++ libraries, that have been necessary for the three dimensional simulations and that will be described in more detail in Chapter §4.
The model and numerical algorithm described above have already been used in the

study of some model wetting problems [56]. Here we found of interest to explore numerically the issue of metastability induced by surface roughness; in particular, inspired by a laboratory experiment performed by Queré et al. [47], in which drops are carefully deposited on a bed of micro-pillars and are then allowed to evaporate (hence reduce their volume), we have followed the transition from the metastable Cassie-Baxter state to the Wenzel one. Numerical simulations based on our model reproduce this interesting effect, even in absence of additional frictional pinning forces on the contact line. Furthermore, we give a numerical estimate on the minimum radius that a drop in equilibrium over the tallest part of the asperities may exhibit and compare it with the experimentally determined one.

Numerical simulations based on a phenomenological description of contact angle hysteresis complete the theoretical study of wetting. Including frictional pinning forces in a phenomenological description of wetting phenomena requires that one complements the energy of classical capillarity theory with the dissipation associated with the movement of the contact line. The resulting model is described in detail in Chapter §3. When testing a state against varied configurations that displace the contact line, the model augmented with dissipation produces additional terms which can be interpreted as the energy dissipated by frictional forces on the contact line. No such energy term and hence, no pinning forces are present in the classical theory, that therefore allows the drop to assume only a well determined static contact angle. The mathematical description of the phenomenological model relies on the use of the phase field energy, conveniently augmented by a dissipation potential. In particular, we replace the problem of minimizing capillary energy with a family of discrete incremental problems (a one-parameter family parametrized by the evolving loading conditions) in which the sum of the energy change and the dissipation due to the motion of the contact line is minimized. The equilibrium shape of the drop at time $t + \delta t$ is obtained from the one at time t by setting up a steepest descent dynamics that is now driven by capillary energy and dissipation. We present a stringent test of this model by comparing its predictions with experimental results on the maximal size of the drop that can remain in equilibrium on vertical glass plates, subjected to a variety of surface treatments that change their wetting properties.

The numerical solution of the system of semi-linear equations associated with the

steepest descent dynamics (9) is not particularly challenging in two dimension and it is easily solved even with an explicit Euler method [56, 57]. The situation changes if we would like to perform three dimensional simulations: the high number of degrees of freedom, the particular structure of the solution (different from 0 and 1 only in a very narrow region) and the different length scales involved suggest the use of an adaptively refining grid strategy. We use Adaptive Mesh Refining (AMR), a dynamic gridding approach that employs a fine grid only where necessary. Furthermore the severe limitations on the time-step imposed by an explicit strategy suggest for the use of fully implicit schemes for the numerical solution of the phase field problem. In Chapter §4, we present a preliminary study, developing an idea due to Prof. F. Alouges, of a fully adaptive, mesh refinement based method for the solution of the Euler-Lagrange equation associated with (8)

$$\begin{cases} -\epsilon\triangle\phi + \frac{1}{\epsilon}\phi(1-\phi)(1-2\phi) + \lambda = 0 \\ \\ \int_\Omega \phi = \mathcal{V} \end{cases} . \tag{10}$$

The method is based on a quasi-Newton scheme in which we provide an approximation of the Jacobian operator arising from the system of non-linear equations and that follows from the discretization of (10). The discretization of the equation is performed by cell centered finite differences and the system assembled at each Newton iteration is solved on composite grids using multigrid methods, that extend the classical developed on structured grids.

The main application for this new numerical approach is the study of an improved version of the experiment introduced in Chapter §2, concerning the complete evolution of a drop evaporating on a substrate of micro-pillars. Just like in real experiments, our aim is to capture the transition from the Cassie-Baxter to the Wenzel state, after a drop has lost part of its volume by evaporation. Once the drop is in complete contact with the solid, we would also like to characterize the effects that the asperities have in the enhancement of the hydrophilic properties of the solid substrate, because of the pinning action of the tips.

The research of a fast and stable numerical strategy for the accomplishment of our goal, is completed by the use of a *continuation method*, that is very useful when dealing with a family of problems whose solutions depends on a continuously changing parameter. In our case, in which the evolving parameter is the volume of the drop, the continuation method has revealed apt at stabilizing the contact line at the most shocking moment for the system, namely when the volume is decreased, and

therefore in providing a good initial guess for the solution at the intermediate steps of the discretized time-evolution.

References:

[A] A.DeSimone, L.Fedeli, A.Turco *A Phase Field Approach to Wetting and Contact Angle Hysteresis Phenomena*, In: *Symposium on Variational Concepts with Applications to the Mechanics of Materials*, IUTAM Bookseries 21, DOI 10,1007/978-90-481-91-481-9195-6_4, ©Springer Science + Business Media B.V. 2010, Page 51.

[B] L. Fedeli, A. Turco, A. DeSimone: *Metastable equilibria of capillary drops on solid surfaces: a phase field approach.* Continuum Mechanics and Thermodynamics: Volume 23, Issue 5 (2011) , Page 453.

[C] S.Cacace, A. Chambolle, A. DeSimone, L. Fedeli: *Macroscopic contact angle of liquid drops on rough surfaces via homogenization and numerical simulations.* (In preparation)

[D] L. Fedeli: *A Quasi Newton method for the numerical solution of the phase field capillary problem.* (In preparation)

Chapter 1

Capillarity on rough surfaces: homogenization approach

1.1 Mathematical statement of the problem

1.1.1 The homogenization formula

Following Section 2-3 of [1] we introduce the variational formulation of the problem. We will focus our attention on the the study of the hydrophobic case (i.e. $\cos\theta^{hom} < 0$); however the hydrophilic case ($\cos\theta^{hom} > 0$) shares the same mathematical background and its investigation would need only few adjustments.
We denote by S, L and V the three regions of R^d ($d = 2, 3$) occupied by the solid, liquid and vapor phases. The first one is a given, regular closed set, possibly unbounded. The other two are the unknowns of the problem.
We are interested in minimizing the following interfacial energy

$$E(L) = \sigma_{SL}|\Sigma_{SL}| + \sigma_{SV}|\Sigma_{SV}| + \sigma_{LV}|\Sigma_{LV}| + [\text{a.t.}] \tag{1.1}$$

where '[a.t.]' stands for the fact that additional integral terms or constraints may be present (classical examples are the potential energy due to gravity or the constraint on the preservation of the volume of L); Σ_{XY} is the interface between phases X and Y, $|\Sigma_{XY}|$ is its measure. The surface tensions σ_{XY} are assumed to be constant, and to satisfy the *wetting condition*

$$|\sigma_{SL} - \sigma_{SV}| \leq \sigma_{LV}. \tag{1.2}$$

Since ∂S is fixed, we can always renormalize the energy E in (1.1) by subtracting a constant c times $|\Sigma_{SV}| + |\Sigma_{SL}| = |\partial S|$. In other words the configurations of minimal

energy are unaffected by the substitution

$$(\sigma_{LV}, \sigma_{SV}, \sigma_{SL}) \to (\sigma_{LV}, \sigma_{S}$$

Moreover, the

$$(\sigma_{LV}, \sigma_{SV}, \sigma_{SL}) \to (\alpha\sigma_{LV},$$

ly positive real number (in this cas

ied accordingly).

now the angle $\theta \in [0, \pi]$ by

$$\cos\theta := \frac{\sigma_{SV} - \sigma}{\sigma_{LV}}$$

Since the right-hand side of (1.3) belongs to $[-1,$

(1.2), the angle θ is well defined. If $\sigma_{SV} \leq \sigma_{SL}$

$\to (1, 0,$

$$\widetilde{E} = |\cos\theta||\Sigma_{SL}| + |\Sigma_{L}$$

The renormalized energy (1.4) shows that, beside

in '[a.t.]', the only relevant physical parameter in

negative, energy minimization promotes minimiz

interface and ∂S is called hydrophobic.

We assume that the solid surface is macrosco

horizontal plane $x_d = 0$, while it is rough at a s

parameter. More precisely, we define a microsco

$$A_\epsilon := \{\epsilon x : x \in$$

here A is a closed set in $\mathbb{R}^d$ such tha $0\}$

dic in the first $d-1$ di some t

by

the energy density σ_{SL}^{hom} is obtained by solving the cell problem

$$\sigma_{SL}^{hom} := \inf_{V} \frac{E(V, Q_t)}{|\omega_t|}, \tag{1.8}$$

where ω_t is the square of all x in the plane $x_d = 0$ such that $-t/2 < x_i < t/2$ for $i = 1, .., d-1$, Q_t is the open cylinder $\omega_t \times \mathbb{R}$, $E(V, Q_t)$ denotes the energy associated with a test set V within the periodicity cell ω_t, with *no additional terms*, and the infimum is taken over all bounded sets V contained in $Q_t \setminus A$ which are symmetric with respect to the coordinate planes $x_i = 0$ for $i = 1, .., d-1$. Similarly, σ_{SV}^{hom} is given by the cell problem

$$\sigma_{SV}^{hom} := \inf_{L} \frac{E(V, Q_t)}{|\omega_t|}. \tag{1.9}$$

The macroscopic contact angle is then given by the formula

$$\cos\theta^{hom} = \frac{\sigma_{SV}^{hom} - \sigma_{SL}^{hom}}{\sigma_{LV}}. \tag{1.10}$$

Minimization problem (1.8) amounts to finding the (energetically) most convenient way to interpose a vapor layer between the given solid phase A and the liquid phase, within the periodicity cell ω_t. Similarly, problem (1.9) amounts to finding the more convenient way to make a transition from solid to vapor. If we replace the interfacial energy E with the renormalized energy $\widetilde{E}$, the energy that appears in the cell problems is given by

$$\widetilde{E}(L, Q_t) = \widetilde{E}(V, Q_t) = |\cos\theta||\Sigma_{SL}| + |\Sigma_{LV}|$$

and one immediately verifies that the infimum in (1.9) is obtained for L empty, that is, $\sigma_{SV}^{hom} = 0$. Hence (1.10) becomes

$$-\cos\theta^{hom} = |\cos\theta^{hom}| = \tilde{\sigma}_{SL} = \inf_{V} \frac{\widetilde{E}(V, Q_t)}{|\omega_t|}. \tag{1.11}$$

This means that the numerical study of the cell problem (1.9) yields the apparent macroscopic contact angle.

1.1.2 The analytical statement

The problem is a cell problem, in $Q = \omega \times [0, H]$, $H > 0$, where $\omega = \mathbb{R}^{N-1}/\mathbb{Z}^{N-1}$ is the $(N-1)$-dimensional torus.

We choose $A \subset Q$, the "bottom surface", a connected open set which contains $\omega \times \{0\}$, and is at positive distance from $\Gamma = \omega \times \{H\}$ (in practice, a subgraph). To

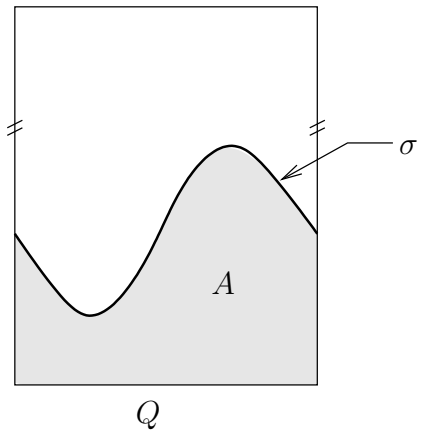

Figure 1.1: *The setting of the cell problem.*

simplify, we assume it has Lipschitz boundary (although this could sometimes be relaxed). We first assume it is regular in the sense that $\mathcal{H}^{N-1}(\partial A \setminus \partial^* A) = 0$. The cell problem consists in finding a set $E \subset \Omega = Q \setminus \overline{A}$, containing Γ, which minimizes

$$\overline{\sigma} \;=\; \min_{E} Per(E,\Omega) \;+\; \int_{\partial A} \sigma \chi_E \, d\mathcal{H}^{N-1} \tag{1.12}$$

where χ_E is the characteristic function of the set E, and $Per(E,\Omega) = \int_\Omega |D\chi_E|$ is the *perimeter* of E in Ω, namely its *Total Variation* (see Appendix A).
Here σ is a constant with $0 < \sigma \leq 1$. More generally, we will also sometimes consider the case where σ is a continuous function, defined on ∂A and with values in $[0,1]$ and positive minimum. The minimum value $\overline{\sigma}$ is the effective contact angle of the homogenized surface.

Observe that the Dirichlet boundary condition $\Gamma \subseteq E$ should be relaxed by adding a term $\int_\Gamma |1-\chi_E(x)| \, d\mathcal{H}^{N-1}(x)$ in the functional, which takes into account (in the "perimeter") the parts of Γ where the trace of χ_E vanishes; with this relaxation we may always assume that E contains a neighborhood of Γ: indeed, since there exists $H' < H$ such that $\omega \times \{H'\}$ is at positive distance from ∂A, if E is any set, the set $E \cup (\omega \times (H', H])$ has an energy lower than or equal to the relaxed energy of E.

1.2 Analysis of the problem

First, let us show that our problem is well-posed.

1.2.1 Existence of a solution

Lemma 1.2.1. *Problem* (1.12) *has a solution.*

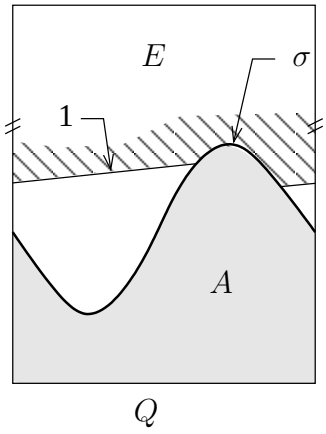

Figure 1.2: *A possible solution E.*

The proof is given in [1]. We give here a quick argument for the reader's convenience. The existence of a solution to (1.12) easily follows from the lower semicontinuity (in L^1) of the functional which is minimized. This property may be shown as follows: we let

$$d_A(x) \;=\; \mathrm{dist}(x, A) \;-\; \mathrm{dist}(x, Q \setminus A)$$

be the signed distance function to ∂A, and we assume that σ is extended to a continuous function $\sigma(x)$ in Q, such that $0 < \sigma < 1$ in $Q \setminus \partial A$. We define $\psi(t) = t^2/(1+t^2)$ if $t \geq 0$, $\psi(t) = t^2$ if $t < 0$. Then, the functional in (1.12) is the supremum

$$\sup_{n\geq 1} \int_Q (\sigma(x) + \psi(n d_A(x))(1-\sigma(x)))\, |D\chi_E| \;+\; \int_\Gamma |1-\chi_E(x)|\, d\mathcal{H}^{N-1}(x) \\ +\; \int_{\omega\times\{0\}} \psi(n d_A(x))\chi_E(x)\, d\mathcal{H}^{N-1}(x)$$

if E is a finite perimeter set in Q (it is $+\infty$ if $E \cap A$ has positive measure). But for finite n, each functional in this supremum is lower semicontinuous.

1.2.2 Basic regularity properties

Observe that the boundary ∂E of any minimizer E is a minimal surface in Ω, hence (if the dimension is not too high), it is analytical. In particular, $\overline{\partial E \cap \Omega} \subset \partial E \cup \partial A$,

hence $\partial E \cup \partial A$ is a closed set of finite measure $\mathcal{H}^{N-1}$. It has therefore the property that, as $\delta \to 0$,

$$\frac{|\{\mathrm{dist}(\cdot, \partial E \cup \partial A) \le \delta\}|}{2\delta} \;\to\; \mathcal{H}^{N-1}(\partial E \cup \partial A) \tag{1.13}$$

(convergence of the Minkowski contents, see [3, 25]). The study of the contact surface $\partial\{x \in \partial A \,:\, \chi_E(x) = 1\}$ would be interesting. In particular, it is likely that if ∂A is smooth enough, then the contact surface will have some regularity [10, 26, 54]. For a piecewise affine ∂A this is less clear, and we leave this point for future study. This would be important, in particular, to get a complete proof of the error estimate in Section 1.3 in dimension higher than $N = 2$.

We observe, however, that a straightforward and standard estimate (see for instance [11]) bounds from below the density of E at $x \in \overline{E}$ (the closure being understood here in Q). To get rid of any ambiguity, we identify E with its points of Lebesgue density 1. The estimate is obtained as follows. We assume (here and in the remainder of the paper) that σ is either a constant or a function bounded from below by $\sigma_0 > 0$. Consider $x \in \overline{E}$, so that $|B(x,r) \cap E| > 0$ for each $r > 0$ (else x is in the interior of the points of density 0 for E). We assume that r is small enough so that $B = B(x,r) \subset Q$ (more precisely, we should consider a ball in the periodic "unfolding" of Q in $\mathbb{R}^{N-1} \times [0,H]$, whose canonical projection onto $\omega \times [0,H]$ is Q, and consider only balls B which lie inside one period (hence, $r \le 1$) but, since we think there is no any ambiguity, we will skip this detail to make the proof more readable).

Then (for a.e. $r \in (0,1)$),

$$Per(E \cap B) \;=\; \mathcal{H}^{N-1}(\partial B \cap E) \,+\, \mathcal{H}^{N-1}(\partial E \cap B \cap \Omega) \,+\, \int_{\partial A \cap B} \chi_E \, d\mathcal{H}^{N-1}\,,$$

but the minimality of E, that is, $\mathcal{E}(\chi_E) \le \mathcal{E}(\chi_{E\setminus B})$, yields (for a.e. $r \in (0,1)$)

$$\mathcal{H}^{N-1}(\partial B \cap E) \;\ge\; \mathcal{H}^{N-1}(\partial E \cap B \cap \Omega) \,+\, \sigma_0 \int_{\partial A \cap B} \chi_E \, d\mathcal{H}^{N-1}\,.$$

Combining the last two inequalities and using the isoperimetric inequality, we get

$$c|E \cap B|^{1-\frac{1}{N}} \;\le\; \frac{\sigma_0 + 1}{\sigma_0} \mathcal{H}^{N-1}(\partial B \cap E)\,.$$

Letting $f(r) := |E \cap B(x,r)|$, so that $f'(r) = \mathcal{H}^{N-1}(\partial B \cap E)$ for a.e. r, we deduce (using Gronwall's technique) that there is a constant $\kappa > 0$, depending only on the dimension and σ_0, such that $f(r)/r^N \ge \kappa > 0$. In particular, if $|E \cap B(x,r)| < \kappa r^N$ for some small radius (≤ 1), x is in the interior of the complement of E.

The same kind of argument would show that if $x \in \Omega \setminus E$ and $B(x,r) \subset \Omega$, then $|B(x,r) \setminus E| \geq \kappa r^N$. In other words if $|B(x,r) \setminus E| < \kappa r^N$, then x is in the interior of E.

Since we have assumed that ∂A is Lipschitz, we can easily deduce (possibly by changing the value of κ) that if $x \in Q \setminus E$ and $|B(x,r) \setminus E| < \kappa r^N$, then x is in the interior of E. Hence the topological boundary of E consists exactly of the points of Q where E has density neither 0 nor 1. In particular, we have $\mathcal{H}^{N-1}(\partial E \setminus \partial^* E) = 0$.

We have shown the following:

Lemma 1.2.2. *Let E solve (1.12). Then E, as a subset of Q, satisfies the two following density estimates: there exists $\kappa > 0$ such that, for r small enough, $r \leq 1$ and such that $B(x,r) \subset Q$),*

- *if $|E \cap B(x,r)| \leq \kappa r^N$, then there is a smaller radius $r' > 0$ such that $|E \cap B(x,r')| = 0$,*
- *if $|B(x,r) \setminus E| \leq \kappa r^N$, then there is a smaller radius $r' > 0$ such that $|B(x,r') \setminus E| = 0$,*

In particular, the points of Lebesgue density 0 or 1 form two open sets, with common topological boundary (denoted ∂E), which coincides $\mathcal{H}^{N-1}$-a.e. with the reduced boundary of E in Q.

1.2.3 Equivalent convex formulation

We show here that our minimization problem is in fact a convex problem (that is, the minimization of a convex functional over a convex domain). The approach is standard.

Let $u \in BV(\Omega)$, and consider the problems

$$\overline{\sigma}_1 \;=\; \min\left\{ \int_\Omega |Du| \;+\; \int_{\partial A} \sigma u \, d\mathcal{H}^{N-1} \;:\; u \in BV(\Omega), u = 1 \text{ on } \Gamma, u \geq 0 \right\} \quad (1.14)$$

and

$$\overline{\sigma}_2 \;=\; \min\left\{ \int_\Omega |Du| \;+\; \int_{\partial A} \sigma |u| \, d\mathcal{H}^{N-1} \;:\; u \in BV(\Omega), u = 1 \text{ on } \Gamma \right\} \quad (1.15)$$

The following proposition shows that $\overline{\sigma}_1 = \overline{\sigma}_2 = \overline{\sigma}$.

Proposition 1.2.1. *We have $\overline{\sigma}_1 = \overline{\sigma}_2 = \overline{\sigma}$. Moreover, given any solution E of (1.12), then χ_E solves both (1.14) and (1.15). Conversely, given any solution u of either (1.14) or (1.15), then for any $s \in (0,1)$, $\{u > s\}$ and $\{u \geq s\}$ are both solutions of (1.12).*

Again, rigorously, we should add a term $\int_\Gamma |1-u(x)|\, d\mathcal{H}^{N-1}(x)$ to the functional to take properly into account the boundary condition on Γ, since, again, if u is any function then $u'(x) = u(x)$ if $x_N < H'$, and $u'(x) = 1$ elsewhere will have lower energy.

The proof of this proposition is an easy consequence of the coarea formula. First, the value $\overline{\sigma}$ of (1.12) is greater than or equal to the solutions of the two other minimization problems. Indeed if E is a set with bounded perimeter in Ω, then the energy of E is the same as the energy of χ_E in (1.14) and (1.15). Then, it is clear that if u is a solution of (1.15), then $u \geq 0$ a.e. (and $u \leq 1$, since $(0 \vee u) \wedge 1$ has lower energy — strictly lower if it differs from u), so that it is a solution of (1.14). Now, one also has

$$\int_\Omega |Du| + \int_{\partial A} \sigma u \, d\mathcal{H}^{N-1} = \int_0^1 \left(Per(\{u > s\}, \Omega) + \int_{\partial A} \sigma \chi_{\{u>s\}} \, d\mathcal{H}^{N-1} \right) ds \geq \overline{\sigma}$$

showing that the value $\overline{\sigma}_1 = \overline{\sigma}_2$ is greater or equal to the value of (1.12). This shows in particular that $\{u > s\}$ solves (1.12) for a.e. $s \in (0,1)$. But since $\{u > s\} = \bigcup_n \{u > s_n\}$ for any sequence $s_n \downarrow s$ while $\{u \geq s\} = \bigcap_n \{u > s_n\}$ for any sequence $s_n \uparrow s$, the proposition is deduced by approximation.

1.2.4 Comparison

We show that our problem is monotonic with respect to σ (in particular, the solution is generically unique, in the sense that, for instance, if we replace σ in (1.12) with $\sigma + t$, $t \in \mathbb{R}$, then there is a unique minimizer E_t for all t but a countable number).

Lemma 1.2.3. *If $\sigma < \sigma'$ on ∂A, and if E solves* (1.12) *with σ and E' solves the same problem with σ replaced with σ', then $\partial E \cap \partial A \supseteq \partial E' \cap \partial A$. In particular, if E is the largest solution corresponding to σ, and E' the smallest corresponding to σ', then $E \supseteq E'$.*

Let u and u' respectively solve (1.14) with σ and σ'. In particular,

$$\begin{aligned} \int_\Omega |Du| + \int_{\partial A} \sigma u \, d\mathcal{H}^{N-1} &\leq \int_\Omega |D(u \vee u')| + \int_{\partial A} \sigma (u \vee u') \, d\mathcal{H}^{N-1} \\ \int_\Omega |Du'| + \int_{\partial A} \sigma' u' \, d\mathcal{H}^{N-1} &\leq \int_\Omega |D(u \wedge u')| + \int_{\partial A} \sigma' (u \wedge u') \, d\mathcal{H}^{N-1} \end{aligned}$$

so that, summing up both inequalities and using the celebrated inequality $\int_\Omega |D(u\vee u')| + |D(u\wedge u')| \le \int_\Omega |Du| + |Du'|$, we find

$$\int_{\partial A} \sigma'(u' - u\wedge u')\, d\mathcal{H}^{N-1} \;\le\; \int_{\partial A} \sigma(u\vee u' - u)\, d\mathcal{H}^{N-1}\,.$$

Since $u'-u\wedge u' = u\vee u'-u = (u'-u)^+$, we deduce that if $\sigma<\sigma'$, $(u'-u)^+ = 0$ $\mathcal{H}^{N-1}$-a.e. on ∂A. In other words, the traces $u'\le u$ on ∂A. Hence, $\partial E'\cap\partial A\subseteq \partial E\cap\partial A$. If u' is a minimal solution and u a maximal solution, we also deduce that $u'\le u$ a.e. in Ω (since otherwise $u'\wedge u\le u'$ is better than u', and $u'\vee u\ge u$ is better than u).

Remark 1.2.4. In dimension $N=2$, if ∂A is a graph and $u=\chi_E$ a solution of the problem, then one shows that ∂E is also a graph. In particular, for a given trace $u=\chi_{\partial E\cap\partial A}$ on ∂A, the graph $\partial E\cap\Omega$ is unique as the solution of a strictly convex problem.

1.2.5 Stability for the cell problem

Let us now show that if ∂A is Lipschitz, the cell problem is "continuous" with respect to variations of ∂A provided that the measure of ∂A is also continuously changed.

Proposition 1.2.2. *Let $A_n\to A$ be such that $\partial A_n\to\partial A$ in the Hausdorff sense, while $\mathcal{H}^{N-1}(\partial A_n)\to\mathcal{H}^{N-1}(\partial A)$, as $n\to\infty$. We assume $\sigma_n : Q\to[0,1]$ is a continuous function, which converges uniformly to σ. We also assume that the boundary ∂A is Lipschitz. We let $\Omega_n = Q\setminus\overline{A}_n$, and*

$$\mathcal{E}_n(u) \;=\; \int_{\Omega_n} |Du| \;+\; \int_{\partial A_n} \sigma_n|u|\, d\mathcal{H}^{N-1}$$

while

$$\mathcal{E}(u) \;=\; \int_{\Omega} |Du| \;+\; \int_{\partial A} \sigma|u|\, d\mathcal{H}^{N-1}.$$

Let $\overline{\sigma}_n = \min_{E\supset\Gamma}\mathcal{E}_n(\chi_E)$ be the effective contact angle for A_n and σ_n. Then $\overline{\sigma}_n\to\overline{\sigma} = \min_{E\supset\Gamma}\mathcal{E}(\chi_E)$ as $n\to\infty$.

In fact, the assumption that ∂A is Lipschitz could here be replaced by slightly weaker assumption, such as the fact of being locally a subgraph at each point.

Proof. We show a Γ-convergence result: first we extend $\mathcal{E}_n$ and $\mathcal{E}$ to $BV(Q)$, by letting $\mathcal{E}_n(u) = \mathcal{E}_n(u_{|\Omega_n})$ if $u=0$ a.e. in A_n, and $+\infty$ else, and $\mathcal{E}(u)=\mathcal{E}(u_{|\Omega})$ if $u=0$ a.e. in A, and $+\infty$ else. Let $u_n\to u$. If $B\subset\subset\Omega$, then $B\subset\Omega_n$ for n large enough and

$$\int_B |Du| \;\le\; \liminf_{n\to\infty}\int_B |Du_n|. \tag{1.16}$$

If B is a neighborhood of ∂A, then it is a neighborhood of ∂A_n for n large enough, and

$$\int_{\partial A} \sigma|u| \;\le\; \int_B \sigma|Du| \;\le\; \liminf_{n\to\infty} \int_B \sigma_n|Du_n| \tag{1.17}$$

$$\le\; \liminf_{n\to\infty} \int_{\partial A} \sigma_n|u_n| \;+\; \int_{B\cap\Omega_n} |Du_n|\,. \tag{1.18}$$

From (1.16) and (1.17) we easily deduce that

$$\mathcal{E}(u) \;\le\; \liminf_{n\to\infty} \mathcal{E}_n(u_n)\,. \tag{1.19}$$

Conversely, let $u \in BV(\Omega;[0,1])$ (identified with $u\chi_\Omega \in BV(Q;[0,1])$), with $u = 1$ on Γ. We want to find a sequence u_n (with also $u_n = 1$ on Γ), converging to u and such that

$$\limsup_{n\to\infty} \mathcal{E}_n(u_n) \;\le\; \mathcal{E}(u)\,. \tag{1.20}$$

From (1.19) and (1.20) will follow the Γ-convergence of $\mathcal{E}_n$ to $\mathcal{E}$, which yields $\overline{\sigma}_n \to \overline{\sigma}$.

First, using Meyers-Serrin's theorem, there exists $u_k \to u$ such that $u_k \in C^\infty(\Omega;[0,1])$ and $\int_\Omega |\nabla u_n|\,dx \to \int_\Omega |Du|$ as $k \to \infty$. Since, by construction, the traces of u_k and u coincide on ∂A (and in any case, since ∂A is Lipschitz, the trace of u_k goes to the trace of u as a consequence of the convergence of the total variations), then $\mathcal{E}(u_k) \to \mathcal{E}(u)$ as $k \to \infty$ and (by a standard diagonal argument) it is enough to show (1.20) for each u_k: hence we assume that u is smooth in Ω.

Since ∂A is Lipschitz, one may extend $u_{|\Omega}$ into a function u' defined on a slightly larger set $\Omega' = \{x \in Q \,:\, \mathrm{dist}(x,\Omega) < \delta\}$ ($\delta > 0$), in such a way that $0 \le u' \le 1$, u' is Lipschitz in Ω' (see for instance [24]).

Let $u_n = u'\chi_{\Omega_n}$, for n large. Clearly,

$$\lim_n \int_{\Omega_n} |\nabla u_n|\,dx = \lim_n \int_{\Omega_n} |\nabla u'|\,dx = \int_\Omega |\nabla u|\,dx\,.$$

Also, $\mathcal{H}^{N-1} \llcorner \partial A_n \rightharpoonup \mathcal{H}^{N-1} \llcorner \partial A$ weakly-$*$ as measures (it follows from the assumption $\mathcal{H}^{N-1}(\partial A_n) \to \mathcal{H}^{N-1}(\partial A)$), while $\sigma_n u' \to \sigma u'$ uniformly in Ω'. Hence,

$$\int_{\partial A_n} \sigma_n u_n\, d\mathcal{H}^{N-1} \;=\; \int_{\partial A_n} \sigma_n u'\, d\mathcal{H}^{N-1}$$

$$\to\; \int_{\partial A} \sigma u'\, d\mathcal{H}^{N-1} \;=\; \int_{\partial A} \sigma u\, d\mathcal{H}^{N-1}$$

as $n \to \infty$. We deduce that $\mathcal{E}_n(u_n) \to \mathcal{E}(u)$, which yields (1.20). □

1.3 Numerical Approximation

1.3.1 Error estimates

We wish to compute $\overline{\sigma}$ as precisely as possible. We assume, for simplicity, that ∂A is a polygonal boundary (by Proposition 1.2.2, any Lipschitz surface ∂A can be replaced by a polygonal set with a small error, provided its total surface $\mathcal{H}^{N-1}(\partial A)$ is precisely approximated: however, the error which is done in this case is quite tricky to estimate).

If ∂A is polygonal, we may find for each $h > 0$ a "triangulation" $\mathcal{T}_h$ of Ω such that each simplex T of $\mathcal{T}_h$ has a diameter less than h. We assume, moreover, some regularity. More precisely: there is a constant K independent of h such that the radius of the largest ball contained in each $T \in \mathcal{T}_h$ is more than the diameter of T, divided by K.

The approximate problem is

$$\overline{\sigma}_h \;=\; \min_{u \in V_h} \mathcal{E}(u) \tag{1.21}$$

where V_h is the set of piecewise affine functions in $C(\Omega)$, affine on each $T \in T_h$, with value 1 on Γ.

Let $u = \chi_E$ be a solution of (1.12). Consider $u^\delta \in C^2(\overline{\Omega})$, with $u = 1$ on Γ and such that for some constant $C > 0$,

$$|D^2 u^\delta| \leq \frac{C}{\delta^2} \;\text{ and } \{u \neq u^\delta\} \subset \{\mathrm{dist}(\cdot, \partial E \cup \partial A) \leq C\delta\} \tag{1.22}$$

(in particular, u and u^δ are constant at some distance from $\partial E \cup \partial A$, which is a closed set of finite measure $\mathcal{H}^{N-1}$). Let $u_h^\delta = \Pi_h(u^\delta)$ be the Lagrange interpolation of u^δ on $\mathcal{T}_h$ ($u_h \in V_h$ and $u_h = u^\delta$ at each vertex of a simplex of $\mathcal{T}_h$). Standard interpolation arguments show that on each simplex $T \in \mathcal{T}_h$,

$$\int_T |\nabla u_h^\delta - \nabla u^\delta|\, dx \;\leq\; c|T| \frac{\mathrm{diam}(T)}{\rho(T)}^2 \|D^2 u^\delta\|_{L^\infty(T)} \;\leq\; cK|T|h\frac{C}{\delta^2} \tag{1.23}$$

where c is a constant (explicit and depending only on the dimension), while $\mathrm{diam}(T)$ and $\rho(T)$ are respectively the diameter of T and the radius of the largest ball contained in T. On the other hand, if Σ is a facet of T,

$$\int_\Sigma |u_h^\delta - u^\delta|\, d\mathcal{H}^{N-1} \;\leq\; c|\Sigma|\mathrm{diam}(\Sigma)^2 \|D^2 u^\delta\|_{L^\infty(\Sigma)} \;\leq\; c|\Sigma|h^2\frac{C}{\delta^2} \tag{1.24}$$

We deduce that

$$\mathcal{E}(u_h^\delta) \;\leq\; \mathcal{E}(u^\delta) \,+\, cK|\{u \neq u_h^\delta\}|\frac{Ch}{\delta^2} \,+\, c\mathcal{H}^{N-1}(\partial A)\frac{Ch^2}{\delta^2}$$

Now, since $u_h^\delta = u^\delta = u$ at distance larger than $C\delta + h$ of $\partial A \cup \partial E$, and using (1.22) and (1.13), we get that

$$|\{u \neq u_h^\delta\}| \leq 4\mathcal{H}^{N-1}(\partial E \cup \partial A)(C\delta + h)$$

if $C\delta + h$ is small enough. Assuming also $h \leq \delta$, we find that there exists a constant (still denoted c), depending on K, on the dimension, on C, and on the energy of χ_E, such that

$$\mathcal{E}(u_h^\delta) \;\leq\; \mathcal{E}(u^\delta) \,+\, c\frac{h}{\delta} \tag{1.25}$$

Assume now that we can build u^δ such that, for some constant $c > 0$,

$$\mathcal{E}(u^\delta) \;\leq\; \mathcal{E}(u) \,+\, c\delta \;=\; \overline{\sigma} \,+\, c\delta\,. \tag{1.26}$$

As shown later this will be the case in dimension $N = 2$ and, under some regularity assumptions, in higher dimension as well. Then, from (1.25) and (1.26), we deduce that the optimal choice of δ (to minimize the global error) is $\delta = \delta_h \simeq \sqrt{h}$, and letting $u_h = u_h^{\delta_h}$, we eventually get the error estimate

$$\overline{\sigma} \,\leq\, \mathcal{E}(u_h) \;\leq\; \overline{\sigma} \,+\, c\sqrt{h} \tag{1.27}$$

It is easy to build u^δ in a few situations. First, if $N = 2$, since ∂A is piecewise affine, one easily shows that $\partial E \cap \Omega$ is a finite union of straight lines connecting two points of ∂A. In this case, we can find $\delta > 0$ small such that we can add a small segment of length δ to both extremities of each of these lines, in such a way that the segment is in the interior of A (except for its end which is common with ∂E). This allows to extend the set E into a set E^δ defined in the whole set $\{x \in Q \,:\, \mathrm{dist}(x, \Omega) < c\delta\}$ for some constant $c > 0$ depending only on ∂A (which is piecewise affine). We mollify χ_{E^δ} by convolution with a radially symmetric kernel $(1/\delta'^N)\eta(x/\delta')$, with support inside the ball of radius $\delta' = c\delta$ centered at the origin: the result, restricted to Ω, is a function u^δ which satisfies both (1.22) and (1.26).

Remark 1.3.1. In higher dimension, the situation is more complicated. If for instance we know that there is a constant c such that $\mathcal{H}^{N-1}(\partial E \cap \{0 < dist(x, \partial A) < \delta\}) \leq c\delta$, then by standard technique we can reflect E across ∂A and the proof will follow as in dimension 1.

Remark 1.3.2. Even if the error estimate (1.27) has been derived on simplexes, for the numerical implementation we found more efficient to use a quads mesh. However we believe that an estimate similar to the previous one is still valid on this kind of triangulation.

1.3.2 The minimization scheme: *ADMM*

From a numerical point of view, the major issue in finding the solution of the equivalent convex formulation is the boundedness requirement $u \geq 0$; this constraint can be "plainly" matched if we work with the functional (1.15). We found the ADMM (alternating direction method of multipliers) algorithm to be very flexible and efficient in this kind of problem. This is a Lagrangian-based technique which is very popular in problems of TV-l_1 minimization (like image restoration). Following [23], we give a brief sketch of the method.
Consider the problem

$$\min_{\substack{u\in\mathbb{R}^m \\ Ku=f}} J(u)$$

and assume that $J(u)$ has separable structure in the sense that it can be written as

$$J(u) = H(u) + \sum_{i=1}^{M} G_i(\widehat{A}_i u + b_i)$$

where H and G are closed proper convex functions $G_i : \mathbb{R}^{n_i} \to (-\infty, \infty]$, $H : \mathbb{R}^m \to (-\infty, \infty]$, $f \in \mathbb{R}^s$, $b_i \in \mathbb{R}^{n_i}$, each $\widehat{A}_i$ is a $n_i \times m$ matrix and K is a $s \times m$ matrix. Introducing new variables $p_i = \widehat{A}_i u + b$

$[-\infty, \infty)$ defined by

$$q_\delta(\mu) = \inf_{\substack{u\in\mathbb{R}^m \\ p\in\mathbb{R}^n}} L_\delta(p, u, \mu)$$

The dual problem to (1.28) is

$$\max_{\mu\in\mathbb{R}^d} q_\delta(\mu) \tag{1.29}$$

Since (1.28) is a convex programming problem with linear constraints, if it has an optimal solution (p^*, u^*) then (1.29) also has an optimal solution μ^* and

$$F(p^*) + H(u^*) = q_\delta(\mu^*)$$

which is to say that the duality gap is zero. So finding an optimal solution of (1.28) and (1.29) is equivalent to finding a saddle point of L_δ. More precisely, (p^*, u^*) is an optimal primal solution and μ^* is an optimal dual solution if and only if

$$L_\delta(p^*, u^*, \mu) \leq L_\delta(p^*, u^*, \mu^*) \leq L_\delta(p, u, \mu^*) \qquad \forall\, p, u, \mu$$

At the step $(k+1)$ the *ADMM* iterations are given by:

$$\begin{aligned} p^{k+1} &= \operatorname*{argmin}_{p\in\mathbb{R}^n} L_\delta(p, u^k, \mu^k) \\ u^{k+1} &= \operatorname*{argmin}_{u\in\mathbb{R}^m} L_\delta(p^{k+1}, u, \mu^k) \\ \mu^{k+1} &= \mu^k + \delta(b - \widehat{A}u^{k+1} - Bp^{k+1})\,. \end{aligned} \tag{1.30}$$

1.3.3 Finite element discretization

We begin the definition of the numerical scheme by introducing the spatial discretization of the domain Ω, on which we will define the finite dimensional spaces V_h and $\mathrm{W_h}$. Let $\mathcal{T}_h$ be a subdivision of Ω into quadrilaterals if $d = 2$, hexaedra $d = 3$, and let K_l be an element of the mesh. Besides, let ∂A_h a polygonal approximation of the boundary of the solid ∂A. In order to simplify the notation, from this point forward we identify the triangulated domain with Ω and the approximation ∂A_h with the boundary ∂A. We then consider two finite dimensional subspaces V_h and $\mathrm{W_h}$; our choice of the discrete spaces for u and Du is the so called Q1-P0 finite element pair, defined as:

$$\begin{aligned} V_h &= \{v \in C^0(\Omega) : v|_{K_l} \in \mathcal{Q}^1(K_l),\, l = 1, .., N_e\} \\ \mathrm{W_h} &= \{\mathrm{w} \in L^2(\Omega)^d : \mathrm{w}|_{K_l} \in \mathcal{P}^0(K_l)^d,\, l = 1, .., N_e\} \end{aligned}$$

where we indicated with N_e the number of elements of the mesh, $\mathcal{P}^0(K_l)^d$ stands for d-dimensional piecewise constant polynomials on the element K_l and $\mathcal{Q}^1(K_l)$ is the space of piecewise polynomials of degree 1 in each coordinate direction. Notice that a basis for such a kind of finite element is given by $\{1, x, y, xy\}$ (the degrees of freedom are identified with the vertexes of the quads) and that obviously the space of the gradient is discontinuous.
In the discretized form (1.15) can be read as:

$$\overline{\sigma}_2 \;=\; \min\left\{\int_\Omega |\nabla u| \;+\; \int_{\partial A} \sigma|u| \;:\; u \in V_h, u = 1 \text{ on } \Gamma\right\}. \tag{1.31}$$

Now we can write the augmented Lagrangian associated with the energy (1.31); we introduce $p_1 \in \mathrm{W_h}$ and $p_2 \in V_h$ as auxiliary variables for the two components of the functional, and in accordance with the notation of the previous section (if n_1 is the number of dofs in $\mathrm{W_h}$ and n_2 is the number of dofs in V_h) we take:

$$K = 0, \quad f = 0, \quad H = 0, \quad n = n_1 + n_2, \quad p = (p_1, p_2)^T, p \in \mathbb{R}^n, \quad b = (0,0)^T$$
$$F(p) = F(p_1, p_2) = G_1(p_1) + G_2(p_2) = \int_\Omega |p_1| + \sigma \int_{\partial A} |p_2|$$
$$\mu = (\mu_1, \mu_2),\ \mu_1 \in \mathrm{W_h}, \mu_2 \in V_h, \quad B = -I, \quad \widehat{A} = \begin{bmatrix} \nabla \\ I \end{bmatrix}.$$

Remember that the operator ∇ is a discrete version of the gradient operator (we give more details about this in the implementation section); so we can write:

$$\begin{aligned} L_\delta(p, u, \mu) = &\int_\Omega |p_1| + \int_\Omega \mu_1 \cdot (p_1 - \nabla u) + \frac{\delta}{2}\int_\Omega |p_1 - \nabla u|^2 \\ &+ \sigma \int_{\partial A} |p_2| + \int_{\partial A} \mu_2(p_2 - u) + \frac{\delta}{2}\int_{\partial A} |p_2 - u|^2 \end{aligned}$$

Now following the scheme (1.30), we define the alternating steps. We minimize first in p, which means that given initial guesses $p^0 = \mu^0 = 0$, u^0 arbitrary, and $\delta > 0$ we find:

$$\begin{aligned} p^{k+1} = \underset{p \in \mathbb{R}^n}{\operatorname{argmin}} &\int_\Omega |p_1| + \int_\Omega \mu_1^k \cdot (p_1 - \nabla u^k) + \frac{\delta}{2}\int_\Omega \left|p_1 - \nabla u^k\right|^2 \\ &+ \sigma \int_{\partial A} |p_2| + \int_{\partial A} \mu_2(p_2 - u^k) + \frac{\delta}{2}\int_{\partial A} |p_2 - u^k|^2 \end{aligned}$$

This is equivalent to finding

$$p^{k+1} = \operatorname{argmin} \int_\Omega \left[|p_1| + \frac{\delta}{2}\left|p_1 - \nabla u^k + \frac{\mu_1}{\delta}\right|^2\right] + \sigma \int_{\partial A} \left[|p_2| + \frac{\delta}{2}\left|p_2 - u^k + \frac{\mu_2}{\delta}\right|^2\right] \tag{1.32}$$

Then we can split the global minimization in two sub-problems for p_1 and p_2 and argue that (with little abuse of notation):

$$\begin{aligned} p^{k+1} &= \underset{p\in\mathbb{R}^n}{\operatorname{argmin}} L_\delta(p, u^k, \mu^k) = \left(\underset{p_1\in\mathbb{R}^{n_1}}{\operatorname{argmin}} L_\delta(p, u^k, \mu^k), \underset{p_2\in\mathbb{R}^{n_2}}{\operatorname{argmin}} L_\delta(p, u^k, \mu^k) \right) \\ &= (p_1^{k+1}, p_2^{k+1}) \end{aligned}$$

We look at the first term of (1.32) and define $a = \nabla u^k - \dfrac{\mu_1^k}{\delta}$; we get the following chain of inequalities:

$$\begin{aligned} \widehat{T}(p_1) := \int_\Omega \left[|p_1| + \frac{\delta}{2}|p_1 - a|^2 \right] &= \int_\Omega \left[|p_1| + \frac{\delta}{2}|p_1|^2 - \delta(p_1 \cdot a) + \frac{\delta}{2}|a|^2 \right] \\ &\geq \int_\Omega \left[|p_1| + \frac{\delta}{2}|p_1|^2 - \delta|p_1||a| + \frac{\delta}{2}|a|^2 \right] \\ &= \int_\Omega \left[\frac{\delta}{2}|p_1|^2 + \frac{\delta}{2} - |p_1|(-1 + \delta|a|) \right] \end{aligned} \tag{1.33}$$

Now, if $(-1 + \delta|a|) \leq 0$, we conclude that (1.33) $\geq \displaystyle\int_\Omega \frac{\delta}{2}|a|^2$ $\forall p_1 \in \mathrm{W_h}$ and the minimum value is attained for $p_1 = 0$.
If $(-1 + \delta|a|) \geq 0$, we calculate the differential of $\widehat{T}(p_1)$

$$\nabla\widehat{T}(p_1) = \int_\Omega \left[\frac{p_1}{|p_1|} + \delta(p_1 - a) \right]$$

which is 0 for $p_1 = \dfrac{a}{|a|}\left(|a| - \dfrac{1}{\delta}\right)$.
So, we conclude that $p_1^{k+1} = \left(1 - \dfrac{1}{\max(1, \delta|a|)}\right) a$. Introducing the *shrinkage* operator $\mathcal{S}_\lambda : v \longmapsto \dfrac{v}{|v|}(|v| - \lambda)^+$ we have:

$$p_1^{k+1} = \mathcal{S}_{\frac{1}{\delta}}\left(\nabla u^k - \frac{\mu_1^k}{\delta} \right).$$

The procedure for the minimization in p_2 is completely similar to the one just described and we get:

$$p_2^{k+1} = \mathcal{S}_{\frac{\sigma}{\delta}}\left(u^k - \frac{\mu_2^k}{\delta} \right).$$

It remains only to perform the minimization in u: omitting the terms that contain p_1^{k+1}, p_2^{k+1}, μ_1^k and μ_2^k since they don't affect the calculation (they are constant with

respect to u) we have:

$$\begin{aligned} u^{k+1} &= \text{argmin } \frac{\delta}{2}\int_\Omega \left|\nabla u - p_1^{k+1} - \frac{\mu_1^k}{\delta}\right|^2 + \frac{\delta}{2}\int_{\partial A}\left|u - p_2^{k+1} - \frac{\mu_2^k}{\delta}\right|^2 \\ &= \text{argmin } \frac{\delta}{2}\int_\Omega \left[|\nabla u|^2 + \left|p_1^{k+1} + \frac{\mu_1^k}{\delta}\right|^2 - 2\Big(p_1^{k+1} + \frac{\mu_1^k}{\delta}\Big)\cdot\nabla u\right] + \\ &\quad \frac{\delta}{2}\int_{\partial A}\left[|u|^2 + \left|p_2^{k+1} + \frac{\mu_2^k}{\delta}\right|^2 - 2u\Big(p_2^{k+1} + \frac{\mu_2^k}{\delta}\Big)\right] \end{aligned} \tag{1.34}$$

Let us call $c_{p_1} := p_1^{k+1} + \dfrac{\mu_1^k}{\delta}$ and $c_{p_2} := p_2^{k+1} + \dfrac{\mu_2^k}{\delta}$, then the stationarity condition for (1.34) reads as:

$$\delta\int_\Omega \Big[\nabla u\cdot\nabla v - c_{p_1}\cdot\nabla v\Big] + \delta\int_{\partial A}\Big[uv - c_{p_2}v\Big] = 0 \quad \forall v \in V_h \tag{1.35}$$

As we will see, (1.35) will give rise to a standard linear system whose solution converges to the numerical solution of our problem.

The last step is the update of the Lagrangian multipliers, that has been done in a standard way:

$$\begin{aligned} \mu_1^{k+1} &= \mu_1^k + \delta(p_1^{k+1} - \nabla u^{k+1})\,, \\ \mu_2^{k+1} &= \mu_2^k + \delta(p_2^{k+1} - u^{k+1})\,. \end{aligned}$$

1.3.4 Numerical implementation

The implementation involves three main steps: the first one is the representation of Du, the second one is the representation of p (i.e. the numerical counter-part of the shrinkage operation) and the last one the representation of u (i.e. the solution of a linear system deriving from the discretization of an elliptic equation).

Step 1: Since u and p are defined over different finite element spaces, each one with its own degrees of freedom and set of basis functions, the first issue of the implementation is to find a right representative for ∇u in $\mathrm{W_h}$, once a representation of u in $\mathrm{V_h}$. So, given $u = \sum_i u_i\phi_i$, with $\{\phi_i\}$ a basis for V_h and $u_i \in \mathbb{R}^{n_1}$, we represent Du through the projection $\Pi(\nabla u)$ onto $\mathrm{W_h}$. Let $\{\psi_j\}$ be a basis for $\mathrm{W_h}$; the problem now is to find $\widehat{u_j} \in \mathbb{R}^{n_2}$ such that $\Pi(\nabla u) = \sum_j \widehat{u_j}\psi_j$; we are requiring that pointwise

$$\sum_j \widehat{u_j}\psi_j(x) = \sum_i u_i\nabla\phi_i(x)$$

We multiply each side of the equation with $\psi_k(x)$ and perform a summation over k

$$\sum_k\left(\sum_j \widehat{u_j}\psi_j(x)\psi_k(x)\right) = \sum_k\left(\sum_i u_i\nabla\phi_i(x)\psi_k(x)\right).$$

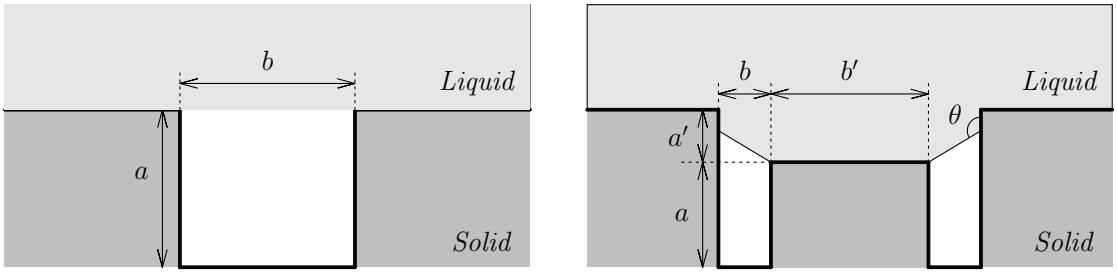

Figure 1.3: *Benchmark configuration: on the left side the pillars have the same height, the geometry on the right leads to a configuration intermediate between the Wenzel and the Cassie-Baxter one.*

Figure 1.4: *Numerical visualization of the mixed configuration.*

Finally, integrating on Ω we get the following linear system:

$$\mathbf{M}^{\psi}\widehat{\mathbf{u}} = \mathbf{b}$$

where the mass matrix $\mathbf{M}^{\psi}$ is given by

$$M^{\psi}_{jk} = \int_{\Omega} \psi_j(x) \cdot \psi_k(x),$$

$\widehat{\mathbf{u}}$ is the unknown vector and $\mathbf{b} = \widehat{\mathbf{B}}\mathbf{u}$, where $\widehat{\mathbf{B}}$ is a $n_1 \times n_2$ matrix, whose the ik-term is given by

$$\widehat{B}_{ik} = \int_{\Omega} \nabla\phi_i(x) \cdot \psi_k(x)$$

and $\mathbf{u}$ is the vector representing the expansion of u on V_h.

Step 2: The second issue of the implementation is to perform the minimization in p_1 and in p_2; since we can compute them by the use of a pointwise formula, what we need is to project the result of the *shrinkage* operation on the finite element spaces that we have defined. Taking into account that the auxiliary variables live in the same space of the associated primal variable and proceeding as before, we get for p_1 (remember the former definition of a):

$$\sum_j \widehat{p_{1_j}}\psi_j(x) = \left(1 - \frac{1}{\max(1, \delta|\sum_l \widehat{a}_l\psi_l(x)|)}\right)\sum_j \widehat{a}_j\psi_j(x)$$

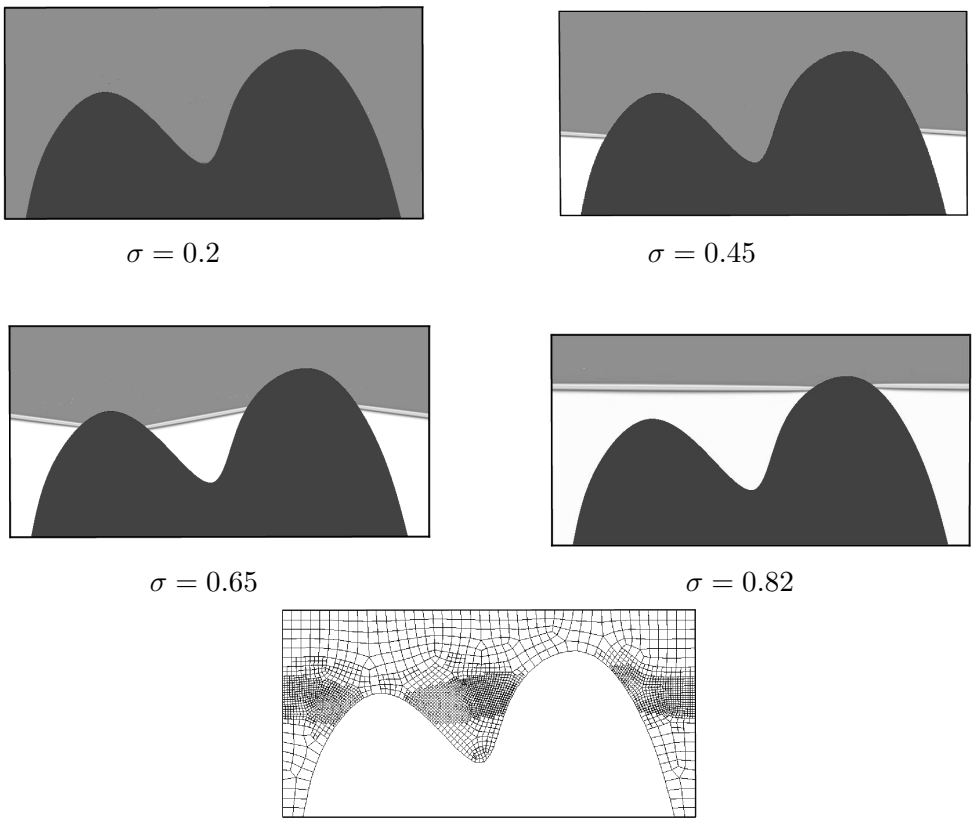

Figure 1.5: *Equilibrium configurations with increasing values of σ, on a spline geometry. The last snapshot shows the adaptive mesh.*

We deduce the following linear system from it:

$$\mathbf{M}^{\psi}\widehat{\mathbf{p_1}} = \widehat{\mathbf{b}}$$

where $\mathbf{M}^{\psi}$ is the mass matrix, $\widehat{\mathbf{p_1}}$ is the vector unknown and $\widehat{\mathbf{b}} = \widehat{\mathbf{M}}^{\psi}\mathbf{a}$ with

$$\widehat{M}^{\psi}_{jk} = \int_{\Omega} \left(1 - \frac{1}{\max(1, \delta|\sum_l \widehat{a}_l \psi_l(x)|)}\right) \psi_j(x) \cdot \psi_k(x)$$

and $\mathbf{a}$ the vector representing the expansion of a on $\mathrm{W_h}$.
The procedure for p_2 is similar but considering $\mathbf{M}^{\phi}$ and $\widehat{\mathbf{M}}^{\phi}$.
Step 3: The last step is standard and deals with the minimization in u; using classical arguments, it is easy to see that (1.35) defines a bilinear form $\mathcal{L}$ and a linear and continuous functional $\mathcal{F}$:

$$\mathcal{L}(u, v) := \delta \int_{\Omega} \nabla u(x) \cdot \nabla v(x) + \delta \int_{\partial A} u(x) v(x)$$
$$\mathcal{F}(v) := \delta \int_{\Omega} c_{p_1}(x) \cdot \nabla v(x) + \delta \int_{\partial A} c_{p_2}(x) v(x)$$

Solving the associated linear system completes the iterative scheme.

1.4 Examples

We begin showing some benchmark experiments in **2-D** in order to check the performance of the method. We consider configurations in which the minimum can be plainly calculated and compared with our numerical results, and indicate with the superscript '*num*' the quantities that are numerical estimates of the real mathematical ones. In particular, for the example on the left of Figure 1.3 (equally spaced pillars all of the same height) we would like to give an estimate of the critical σ above which the liquid prefers to fill the space between the asperities. It is easy to see that such a geometry allows only two possible minimum configurations: one has the transition at the level of the top of the pillars (Cassie-Baxter configuration), in the other one, the cavities are filled by the fluid (Wenzel configuration.) So, if we choose $a = 0.3333$ and $b = 0.3334$, the critical σ that establishes the switch, is given by $\sigma_{crit} = 0.3334$. The numerical results are very satisfactory; we obtain (within five minutes using a laptop PC) the following estimates: $\sigma_{crit}^{num} \approx 0.335$. In Table 1.1 the real quantities are compared with their numerical approximations, using different values for σ. We should specify that the result depends on the size of the mesh; it could be possible, exploiting adaptive refinement and obviously more computing resources, to reach even much better estimates.

In the second example we consider (right panel of Figure 1.3) the possible behaviour is more complicated, indeed even equilibrium configurations of the liquid that mix features of Wenzel's model (complete contact on tall asperities) with features of the Cassie-Baxter model (composite contact on short asperities) are allowed. It is easy

Table 1.1: *Numerical results of the first benchmark experiment, left picture of Figure 3. Recall that* $\sigma_{crit} = 0.3334$.

Surface tension	Behaviour	TV	TV^{num}	*Energy* $\mathcal{E}$	$\mathcal{E}^{num}$	θ	$\theta^{hom;num}$
$\sigma = 0.32$	*Wenzel*	0	$1 \cdot e^{-5}$	0.5333	0.5333	108°	122°
$\sigma = 0.34$	*Cassie Baxter*	0.3334	0.3339	0.56	0.5619	110°	124°

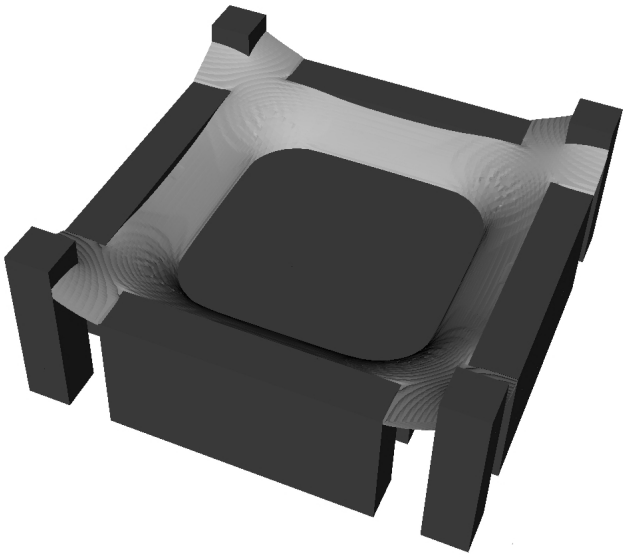

Figure 1.6: *Square cross section pillars in 3-D.*

to show that this intermediate configuration is the optimal one if:

$$\frac{a'}{b'} \leq \frac{1-\sigma}{2\sigma} \leq \frac{a}{b}$$

Here $\sigma = |\cos\theta|$, where σ is the contact angle at the microscopic scale which is fixed. If we choose $a = 0.2$, $b = 0.1$, $a' = 0.2$ and $b' = 0.3$, we have that the upper bound of the inequality is violated for $\sigma^u_{crit} = 0.2$, while the bottom one for $\sigma^d_{crit} = 0.4285$ (even if also this one is an approximation since in the inequality we replaced the length of the slightly tilted liquid-vapor interface with the length of its horizontal projection). For $\sigma \geq \sigma^u_{crit}$ the liquid touches only the tallest faces of the pillars, instead for $\sigma \leq \sigma^d_{crit}$ it fills all the cavities. Also in this case the numerical results are very satisfactory, we obtained the following estimates: $\sigma^{d,num}_{crit} \approx 0.455$ and $\sigma^{u,num}_{crit} \approx 0.2$ (as mentioned above, the analytical critical values are affected by a simplification).

The third example deals with more complicated geometries: the choice of optimal geometries is no longer in a discrete set (for example only two for the case of pillars at the same height), but there is a continuous range of possible liquid-vapor interfaces that are determined by the value of σ.

Fig. 1.5 shows different equilibrium configurations as σ is varied. We notice that in this case the periodic condition is not "naturally" matched as before (since the

Table 1.2: *Numerical results of the second benchmark experiment, right picture of Figure 3. Recall that* $\sigma^u_{crit} = 0.2$ *and* $\sigma^d_{crit} = 0.4285$.

Surface tension	Behaviour	TV	TV^{num}	*Energy* $\mathcal{E}$	$\mathcal{E}^{num}$	θ	$\theta^{hom;num}$
$\sigma = 0.2$	*Wenzel*	0	$1 \cdot e^{-5}$	0.44	0.44	101.5°	116°
$\sigma = 0.205$	*Mixed*	0.2044	0.2043	0.4417	0.4435	102°	116°
$\sigma = 0.455$	*Mixed*	0.2246	0.226	0.7241	0.7256	117°	136.5°
$\sigma = 0.46$	*Cassie Baxter*	0.5	0.5	0.73	0.7316	117°	137°

Table 1.3: *Numerical results of the configuration with spline basement.*

Surface tension	Behaviour	TV^{num}	$\mathcal{E}^{num}$	θ	$\theta^{hom;num}$
$\sigma = 0.2$	*Wenzel*	$1 \cdot e^{-7}$	0.3307	101.5°	109°
$\sigma = 0.45$	*Mixed*	0.2293	0.7365	116.7°	137.5°
$\sigma = 0.65$	*Mixed*	0.5826	0.9203	130.5°	157°
$\sigma = 0.85$	*Cassie Baxter*	0.8722	0.9884	148°	171°

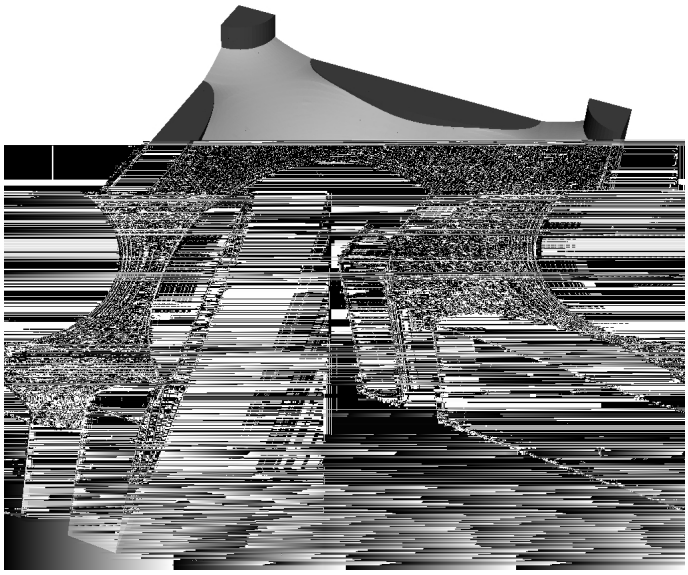

Figure 1.7: *Cylindrical cross section pillars in 3-D.*

lateral position and the same height of the pillars forced the solution to be periodic) but now it is a real forcing feature for the solution and because of it the liquid-vapor interfaces do not lie on straight lines but have to follow diagonal trajectories. For this set of simulations we introduced a gradient detector refinement method in order to make the mesh finer only in the regions where it is required (that is where the liquid-vapor interface is localized).

Finally we consider some three-dimensional examples. Our aim has been to recover also in a three dimensional environment the configurations of intermediate type seen

Figure 1.8: *Diagonal section of the solution.*

Table 1.4: *Numerical results for the 3D simulations*

Surface tension	Pillars type	Behaviour	TV^{num}	$\mathcal{E}^{num}$	θ	$\theta^{hom;num}$
$\sigma = 0.42$	*Cylindrical cross section*	*Mixed*	0.561	0.8092	115°	144°
$\sigma = 0.42$	*Square cross section*	*Mixed*	0.43027	0.761	115°	139.5°

Figure 1.9: *Horizontal section of the solution.*

in **2-D**. In the **3-D** case, however, the calculations are more complicated because the liquid-vapor interfaces are no longer straight: they are instead portions of minimal surfaces. We have considered both cubic and cylindric pillars at different height, that in sections (parallel to the coordinate axes) present the peculiar sizes that in two dimensions let us see the intermediate states (neither Cassie-Baxter nor Wenzel).

As we can see in Fig. 1.6 and in Fig. 1.7 (where we plotted the solutions isosurfaces at level 0.5) also in three dimensions there is a set of optimal solutions that can both touch the lateral part of the pillars and make the liquid-vapor transition. Notice that, as predicted in the theoretical part, the boundary of the geometrical solution ∂E, is a minimal surface and, especially in the case of cubic pillars, the change of curvature close to the asperities is evident. In Fig. 1.8, where a diagonal section of the analytical solution is showed, it is easy to see how the transition region is bended.

Chapter 2

The phase field approach to wetting

In this chapter we start the description of the phase field model for the investigation of wetting phenomena. In particular we will introduce the classical geometric theory of capillarity and will explain its connection with analytical formulation, showing the Γ-convergence results that guarantee the identification of the liquid region by means the *phase function*. This part of the thesis is the natural continuation of a previous work began by Dr. Alessandro Turco. In particular, developing the material that has constituted the core of the paper [56], we have tested it for the study of capillarity on rough substrates. The last part of the chapter is focused on the description of a numerical experiment regarding the transition from a Cassie-Baxter state to a Wenzel one.

2.1 The theoretical review

In the classical (geometric) theory of capillarity, the energy of a liquid drop ω in contact with a solid S and surrounded by vapor is given by [16, 26]:

$$\begin{aligned} E(\omega,t) &= \int_{\partial_S\omega}\sigma_{SL}(x)dA_x+\int_{\partial_V\omega}\sigma_{LV}(x)dA_x+\int_{\partial S\setminus\partial_S\omega}\sigma_{SV}(x)dA_x \\ &+ \int_{\omega}\rho_L(x)G(x,t)d\mathcal{V}_x \end{aligned} \tag{2.1}$$

where $\partial_S\omega$ is the interface between liquid and solid, also denoted by Σ_{SL}, $\partial_V\omega = \partial\omega\setminus\partial_S\omega$ is the liquid-vapor interface Σ_{LV} and $\partial S\setminus\partial_S\omega$ is the solid-vapor one, Σ_{SV}. Since we consider a homogeneous fluid, ρ_L is set equal to 1, while $G(x,t)$ stands for

a generic potential related to an external force field (in our case this will typically be gravity). The terms $\sigma_{XY}(x)$ are the surface tensions at a point x on the XY interface. When S represents a homogeneous solid, σ_{SL} and σ_{SV} are constant and (2.1) simplifies to

$$\begin{aligned} E(\omega,t) &= \sigma_{SL}|\Sigma_{SL}| + \sigma_{LV}|\Sigma_{LV}| + \sigma_{SV}|\Sigma_{SV}| + \int_\omega G(x,t)d\mathcal{V}_x \\ &= (\sigma_{SL}-\sigma_{SV})|\Sigma_{SL}| + \sigma_{LV}|\Sigma_{LV}| + \int_\omega G(x,t)d\mathcal{V}_x + k \end{aligned} \tag{2.2}$$

where $|T|$ denotes the measure of the set T and k is a constant that does not affect the search for the minima of the functional, and so it will be omitted.

Dropping, for simplicity, the time dependence until further notice, and given a fixed volume $\mathcal{V} > 0$, the (geometric) problem of capillarity is to find

$$\omega^* = \underset{|\omega|=\mathcal{V}}{\operatorname{argmin}}\{E(\omega)\}. \tag{2.3}$$

This constraint on the volume $\mathcal{V}$ of the liquid derives from the hypothesis of incompressibility. To deal with such constraint, we introduce a Lagrange multiplier p and we consider a modified energy:

$$\bar{E}(\omega) = E(\omega) + p\mathcal{V} \tag{2.4}$$

The first variation of this functional produces [26] the well known laws of Laplace and Young. The first one prescribes the mean curvature H of the surface Σ_{LV}:

$$2H_{\Sigma_{LV}}(x) = \frac{p}{\sigma_{LV}} + \frac{1}{\sigma_{LV}}G(x). \tag{2.5}$$

The constant p has the physical meaning of pressure jump across the surface of the drop.

Young's law fixes the contact angle the drop forms with the solid surface as the one which makes the capillary energy (2.4) stationary. The resulting value for the contact angle (measured from the inside as in Figure 3.1), denoted by θ_Y, is given by

$$\cos\theta_Y = -\frac{\sigma_{SL}-\sigma_{SV}}{\sigma_{LV}}. \tag{2.6}$$

The geometric formulation described above is not suitable to simulate numerically wetting experiments where drops may split or merge. Phase field methods have been devised precisely to overcome this difficulty and have been already used in [56] to reproduce drop splitting phenomena. Consider, then, a bounded region $\Omega \subset \mathbb{R}^3$ (the container) whose boundary $\partial\Omega$ describes a homogeneous solid surface and let

$W(s) = a^2 s^2 (1-s)^2$ be a non-negative potential (with $a > 0$ to be specified later). A phase field formulation for the capillary problem is obtained by considering an energy of the type

$$E_\epsilon(\phi) = \int_\Omega \left(\epsilon |\nabla \phi|^2 + \frac{1}{\epsilon} W(\phi) + \phi G(x) + \lambda \phi \right) dx \tag{2.7}$$

where ϕ is the phase function. The potential W, that vanishes only for the values 0 and 1 of ϕ representing the vapor and the liquid phases, has to be tuned in order to produce the correct surface tension values from the corresponding interphase transition layers in the limit as $\epsilon \to 0$. We recall the results concerning the asymptotic behavior of ϕ as ϵ goes to zero obtained in a previous work [56]. There we proved rigorously the $\Gamma-$convergence of the phase field functional (2.7) to the (geometric) capillary energy (2.4) (with $p = \lambda$), provided that the correct Dirichlet or Neumann boundary condition are imposed to ϕ on $\partial\Omega$. This kind of variational convergence guarantees convergence of the minimizers of the corresponding functionals. In other words, we can work with the phase field model being sure that, when ϵ is small enough, the $\epsilon-$solutions we find are good approximations for the minimizers of (2.4), and converge to them in the limit $\epsilon \to 0$.

The theory fixes parameter a to the value $3\sigma_{LV}$. The Dirichlet boundary condition $\phi_{|\partial\Omega} = \phi_S$ that enforces Young's contact angle is recovered by solving the algebraic equation

$$\cos\theta_Y = -4\phi_S^3 + 6\phi_S^2 - 1 \qquad 0 \le \phi_S \le 1. \tag{2.8}$$

Notice that equation (2.8) has always exactly one solution in the range of variability of the physical parameters involved [16]. Alternatively, Young's contact angle may be enforced by imposing a Neumann condition on ϕ, namely, $-2\epsilon \frac{\partial \phi}{\partial \lambda}$ ation]TJg57(con)n332

2.2 Numerical implementation

We typically work in situations where it is a-priori known that the liquid will occupy a small part of the container Ω appearing in (2.7). We thus set the problem in a computational domain $\Omega^* \subset \Omega$, a bounded subset of $\mathbb{R}^3$ with piecewise $\mathcal{C}^2$ and Lipschitz boundary. We decompose $\partial\Omega^*$ into two parts: $\partial\Omega^* = \partial_S\Omega^* \cup \partial_V\Omega^*$. The set $\partial_S\Omega^*$ is the part of $\partial\Omega^*$ which is common with the solid surface, denoted by ∂S in (2.1) and by $\partial\Omega$ a few lines above (2.7), and it is a proper subset of $\partial\Omega$. The set $\partial_V\Omega^*$ is the part of $\partial\Omega^*$ contained in the interior of Ω that we can assume to be occupied by the vapor phase. Notice that when the computational domain is much smaller than the mathematical one, the effects of the boundary parts of Ω far from the liquid phase are negligible. The Euler-Lagrange equations for the phase-field model are (here we assume $G = 0$, $a = 1$ for simplicity, and Neumann boundary condition on the solid):

$$\begin{cases} -\epsilon\triangle\phi + \dfrac{1}{\epsilon}\phi(1-\phi)(1-2\phi) + \lambda = 0 & \text{in } \Omega^* \qquad (2.10a) \\ \dfrac{\partial\phi}{\partial n} = -\dfrac{N}{2\epsilon} & \text{on } \partial_S\Omega^* \qquad (2.10b) \\ \phi = 0 & \text{on } \partial_V\Omega^* \qquad (2.10c) \end{cases}$$

where λ is a Lagrange multiplier whose value has to be calculated in order to meet the volume constraint $\int_{\Omega^*}\phi = \mathcal{V}$. When Dirichlet, rather than Neumann boundary conditions are imposed on the solid, we replace equation (2.10b) on $\partial_S\Omega^*$.

2.2.1 The basic numerical scheme

To solve the equilibrium equations (2.10), we transform the problem into a parabolic PDE generated by a gradient flow [6], and we follow an artificial relaxation dynamics until the system reaches the equilibrium configuration. The gradient flow is introduced by setting $\phi = \phi(\tau, x)$, where τ is a fictitious time, and solving

$$\phi_\tau = \epsilon\triangle\phi - \frac{1}{\epsilon}\phi(1-\phi)(1-2\phi) - \lambda. \qquad (2.11)$$

Here the Laplacian is with respect to the space derivatives and the subscript τ denotes a time derivative. Since along the flow (2.11) the energy is decreasing in time

$$\frac{d}{d\tau}E_\epsilon = -2\int_{\Omega^*}|\phi_\tau^2|dx \leqslant 0\,,$$

we will obtain in the limit $\lim_{\tau\to+\infty}\phi(\tau,\cdot)$ a solution of our original equilibrium equation (2.10) which is a (local) minimizer for (2.7).

For the time integration of the equation, we have used a forward Euler scheme, which is stable only for sufficiently small values of $d\tau$. A stability analysis leading to the crucial estimate of the stable time increment is given in the next sub-section. In order to find at each iteration the correct value for the Lagrange multiplier λ, we have implemented a splitting method: given an initial guess ϕ_0 that satisfies the appropriate boundary condition on the derivatives, we follow the scheme:

$$\phi^{N+\frac{1}{2}} = d\tau\left(\epsilon\triangle\phi^N - \frac{1}{\epsilon}\phi^N(1-\phi^N)(1-2\phi^N)\right) + \phi^N$$

$$\lambda^N = \frac{\mathcal{V} - \int_{\Omega^*}\phi^{N+\frac{1}{2}}}{\int_{\Omega^*}1}$$

$$\phi^{N+1} = \phi^{N+\frac{1}{2}} + \lambda^N$$

where $\mathcal{V} = \int_{\Omega^*}\phi^0$. By construction we have that $\int_{\Omega^*}\phi^N = \mathcal{V}$ stays constant during the iterations; the space derivatives have been calculated by means of a seven-point finite differences stencil which guarantees a second order accuracy.

2.2.2 A sufficient condition for numerical stability

The gradient flow technique shows a very stable behavior, provided the parameter of the simulations are well tuned. If ϵ is too small with respect to the grid spacing h, then the level curves of ϕ lose smoothness and mobility. If the volume of the drop is too small with respect to the transition width (and hence with respect to ϵ), the algorithm is unstable. If the time step $d\tau$ is too large, the scheme diverges. A sufficient condition for the stability of the algorithm is

$$d\tau \leq \frac{\epsilon h^2}{12\epsilon^2 + 2Kh^2}. \tag{2.12}$$

To prove this we follow [34]. We will omit the λ term, because it is known that low order terms do not affect the stability of the scheme (see, [53] for example). The

algorithm can be rewritten in a compact form:

$$\frac{\phi^{n+1}_{i,j,k} - \phi^{n}_{i,j,k}}{d\tau} = -\frac{1}{\epsilon} f(\phi^{n}_{i,j,k}) + \\ + 2\epsilon \left(\frac{-6\phi^{n}_{i,j,k} + \phi^{n}_{i+1,j,k} + \phi^{n}_{i-1,j,k} + \phi^{n}_{i,j+1,k} + \phi^{n}_{i,j-1,k} + \phi^{n}_{i,j,k+1} + \phi^{n}_{i,j,k-1}}{h^2} \right), \tag{2.13}$$

where f is the derivative of our potential $W(x) = Kx^2(1-x)^2$, K is the factor that have to match the physical parameter σ_{LV} in the Γ-convergence. The error r due to round-off and approximation satisfies:

$$\frac{r^{n+1}_{i,j,k} - r^{n}_{i,j,k}}{d\tau} = \left(-\frac{12\epsilon}{h^2} - \frac{1}{\epsilon} f'(\phi^{n}_{i,j,k}) \right) r^{n}_{i,j,k} + \\ + \frac{2\epsilon}{h^2} \left(r^{n}_{i+1,j,k} + r^{n}_{i-1,j,k} + r^{n}_{i,j+1,k} + r^{n}_{i,j-1,k} + r^{n}_{i,j,k+1} + r^{n}_{i,j,k+1} \right) \tag{2.14}$$

where a Taylor expansion of $f(\phi + r) \simeq f(\phi) + f'(\phi)r$ has been used assuming that r is small. Rearranging we obtain:

$$r^{n+1}_{i,j,k} = \left(1 - \frac{12\epsilon d\tau}{h^2} - \frac{d\tau}{\epsilon} f'(\phi^{n}_{i,j,k}) \right) r^{n}_{i,j,k} + \\ + \frac{2\epsilon d\tau}{h^2} \left(r^{n}_{i+1,j,k} + r^{n}_{i-1,j,k} + r^{n}_{i,j+1,k} + r^{n}_{i,j-1,k} + r^{n}_{i,j,k+1} + r^{n}_{i,j,k+1} \right) \tag{2.15}$$

At this point the analysis splits into two parts: the liquid and the vapor zone will be considered first, and then the interface. If $\phi \simeq 0$ (vapor) or $\phi \simeq 1$ (liquid), then $f'(\phi) = 2K(1 - 6\phi + 6\phi^2) > 0$ and $f'(\phi) \simeq 2K$. Hence the equation for r^{n+1} can be seen as a weighted sum: since the sum of the coefficients is $1 - \frac{d\tau}{\epsilon} f'(\phi^{n}_{i,j,k}) < 1$, if they are all positive, the following inequality holds

$$r^{n+1}_{i,j,k} \leq \left(1 - \frac{d\tau}{\epsilon} f'(\phi^{n}_{i,j,k}) \right) \max_{i,j,k} \{ r^{n}_{i,j,k} \}, \tag{2.16}$$

which implies stability. Therefore the algorithm is stable if all the coefficients of the sum are positive, and we obtain (2.12).

The interface does not enter in the stability condition, unless it is too wide with respect to the computational box. The worst possible case for the previous estimate is a situation in which $\phi = 0.5$ in the whole interface and hence $f'(\phi) = -K$. Supposing $r^{n}_{i,j,k} = r^n$ for all i, j, k and denoting with N the number of computational nodes and M the number of nodes in the interface, we have:

$$\sum r^{n+1} = \left(N \left(1 - \frac{2Kd\tau}{\epsilon} \right) + 3K \frac{d\tau}{\epsilon} M \right) r^n. \tag{2.17}$$

The stability is maintained if $\sum r^{n+1} < \sum r^n = N r^n$ and this is true if $M < \frac{2}{3}N$. This condition is always satisfied in typical applications ($N = 10^6$, $M \simeq 4\sqrt[3]{N} = 400$).

Because of the simplifications made in its derivation, the bound (2.12) is only a sufficient condition for the stability of the algorithm. Indeed, we ran stable simulations with higher values of the time increment. However, used as an equality, (2.12) gives a formula yielding for each grid spacing h and each transition thickness ϵ, a stable time increment $d\tau$. As described in the Appendix B, this information plays a crucial role in setting up a multigrid algorithm, in which the grid spacing h (and hence the stable time step $d\tau$) varies with the refinement level.

2.2.3 Adaptive mesh refinement

In the simulations of interest for applications, several widely separated length scales occur simultaneously: the size of the drop, the size of the asperities of the solid (more generally, the size of the heterogeneities of the solid surface), the size of the diffuse interface that resolves the liquid-vapor interface. A natural idea is then to pursue adaptive mesh refinement within a multigrid scheme.

We use static refinement in the region close to the solid, and dynamic refinement close to the liquid-vapor interface Σ_{LV}. The criterion for dynamic refinement is the following: we regrid using up to two levels of refinement in the regions where $0.05 \leq \phi \leq 0.95$. Accuracy needs to be preserved across boundaries of regions where the computational mesh changes from coarse to fine. This is done using interpolation techniques which preserve the second order accuracy of the Laplacian across a level boundary, and is handled using ghost cells (a layer of fictitious nodes that contribute to the seven-point stencil at the boundary of real cells).

The update of the solution must preserve synchronization over the different levels of the composite grid. For this purpose, we adopted a *V-type* scheme: an iterative cycle that prescribes at each step to update first the solution on the finest level, then to pass the new information down to the coarsest, so to update ϕ, and finally to come back up. The stability estimate (2.12) demands smaller time steps for finer grids, and synchronization forces us to use small time steps in the coarse grid as well.

The complex structure of the grid hierarchy, with its ghost and real cells, the interpolations, the indexing of such a large number of degrees of freedom, and the parallelization of the code was made possible by the use of an existing ad hoc library:

SAMRAI, a C++ library specifically developed for adaptive mesh refinement [59]. In particular, for the parallelization of the code, **SAMRAI** manages a set of so-called *patches*: a partitioning of the computational domain in smaller disjoint sub-domains which at the moment of calculation can be distributed to the components of a cluster of processors. The simulations were performed on the high performance computing grid available at SISSA (International School for Advanced Studies, Trieste). Further details of the implementation are given in the Appendix B, and in [56, 57].

2.3 Metastability induced by surface roughness: fakir drops

We now present the results obtained using the algorithm described in the previous section. The first example concerns the stability of equilibrium states on micropillars, a topic that has received considerable attention in the recent literature, see [13, 31, 32]. In such as study, we will rely on the fact that the proposed gradient flow algorithm will arrest at any stationary point of the phase field energy functional (2.7), namely, at any solution of the equilibrium equations (2.10), even when this is not a global minimum.

In fact, it is worth emphasizing that the $\Gamma-$convergence analysis above guarantees that global minimizers of the phase field energy (2.7) converge to global minimizers of the classical (geometric) capillarity problem. Hence numerically computed global minimizers of the phase field problem are good approximations of global minimizers of classical capillarity theory. To the best of our knowledge, similar convergence results for critical points are not available. Nevertheless, we will accept on a heuristic basis that, for small enough ϵ, solutions of the equilibrium equations (2.10a) provide a good description of equilibrium configurations of capillary drops.

For drops resting on rough surfaces, two distinct equilibrium states are available: either the drop touches only the top of the asperities or it wets completely the solid surface. The first scenario is known as a Cassie-Baxter state, in which vapor is trapped at the bottom of asperities: a drop in such a regime is reminiscent of a fakir lying on a bed of nails. The second one corresponds to the Wenzel state. More details about these equilibrium states can be found in [1, 16].

We consider here a drop over a hydrophobic solid surface, with Young contact angle $\theta_Y = 120^\circ$, textured with pillars of height $12\mu m$, with square cross-section of edge length $2\mu m$, interpillar distance of $18\mu m$. Therefore the ratio between the area

of the top of the asperities and the area of the whole horizontal projection is 1%. In this situation, it is known that the Wenzel configuration is the energy minimizer but metastable fakir drops can be observed, for example if they are gently deposited over the surface, provided that their size is large enough. After some evaporation, when the size of the drop is sufficiently decreased, this configuration becomes unstable and the Wenzel state is suddenly recovered [13].

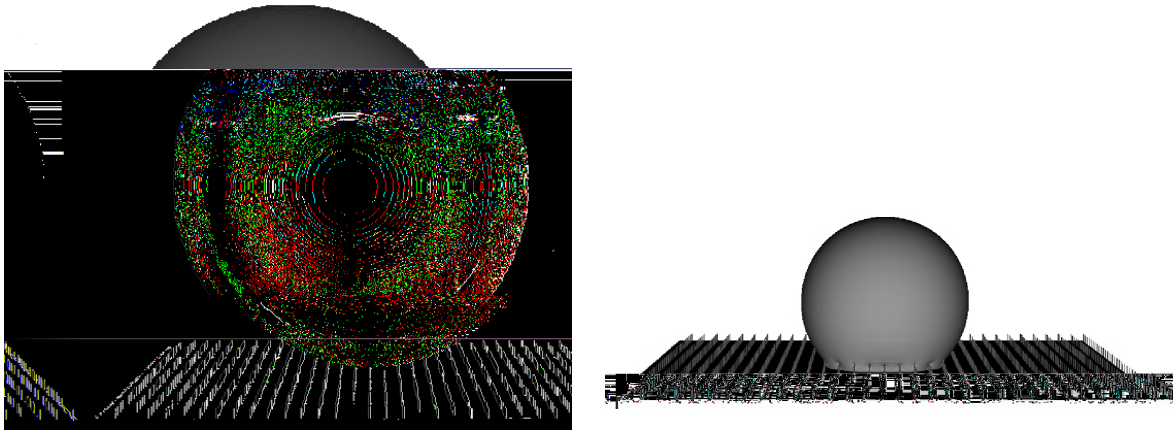

Figure 2.1: *If the radius of the drop is large enough, then a metastable Cassie-Baxter state can be produced (left). Upon evaporation, a Wenzel state is produced (image on the right), the configuration providing the global minimum of the capillary energy.*

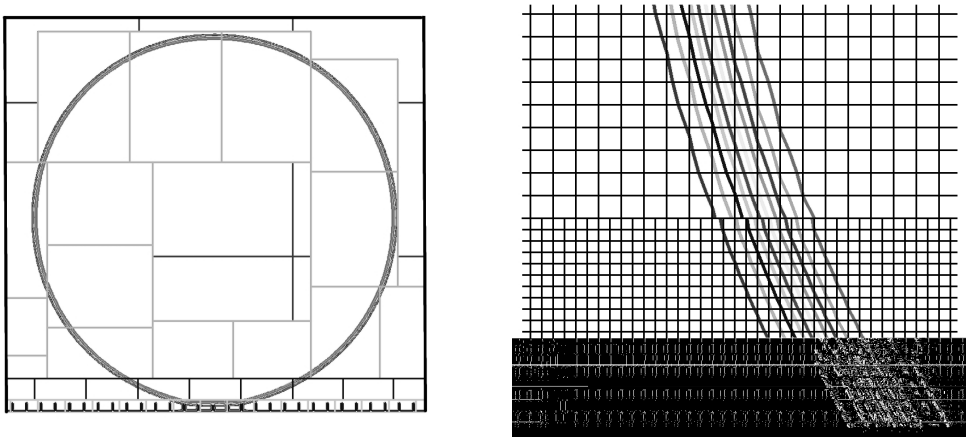

Figure 2.2: *Vertical section of the solution level curves. We can appreciate the partitioning of the domain in patches (left) and the continuity of the solution between two boxes of the composite grid at refinement levels three and four, just over the basis of the pillars (right).*

Our results are shown in Figure 2.1. We place a drop inside a cubic computational cell of edge length $d = 0,32\ mm$. The Cassie-Baxter configuration on the left is attained with a drop whose volume is 0,56 μl (this is the volume of a spherical drop

with radius 0,51 mm). When the volume is further decreased by evaporation, a Wenzel configuration is reached. We decrease the volume in steps of about 0.1 μl and observe a Cassie-Baxter state up to 0.16 μl and a jump to a Wenzel state at 0.058 μl. This leads to an estimate of the critical radius for the transition of 0.24 mm. The experimental value reported in [13] for such transition on a surface with the same properties as the one we simulate is around 0.2 mm. This means that we slightly under-estimate the stability of the Cassie-Baxter state with respect to experiments. Notice that, consistently with the fact that the *capillarity length* for pure water (at standard pressure and temperature) is about 2 mm, gravity plays a negligible role in our simulations.

The simulations were performed using four levels of refinement near the solid, where the most complex geometries are expected, three around the liquid-vapor interface and two and one for the remaining regions; this led us to run numerical experiments also involving about 40 millions of computational cells. The typical CPU time on 64 processors in order to generate an equilibrium configuration is a couple of days, during which at least 80000 iterations of the V-cycle are performed. As it is evident looking at Figure 2.2, the computation is not affected by the division of the computational domain in boxes with a different grid-spacing; in particular the solution remains continuous also along the patches at different refinement levels. We remark that the typical interface thickness is about $10h$, where h is the smallest grid spacing. (Table 2.1)

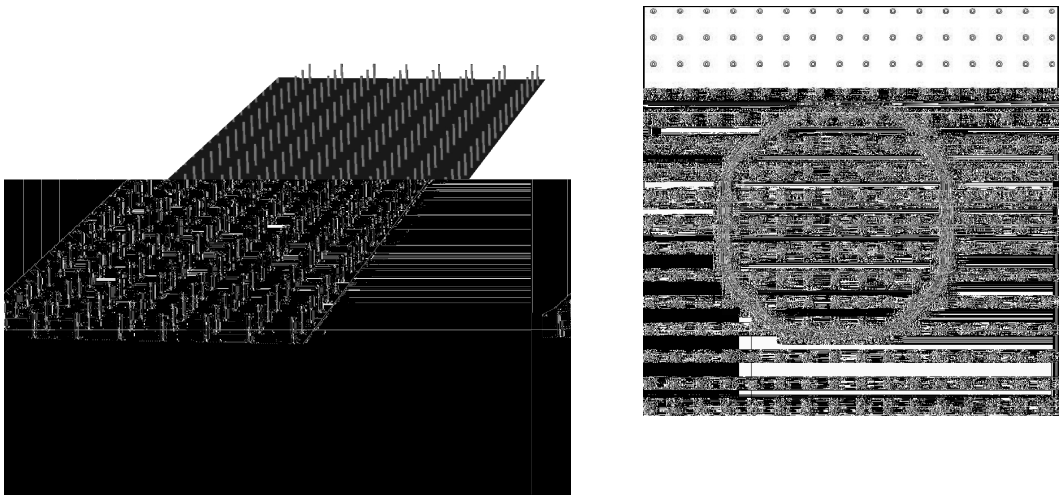

Figure 2.3: *A snapshot of the pillars (left) and contour lines of a Wenzel drop at the level of the textured solid (right).*

Table 2.1: *Parameters used in the pillars simulations.*

Description	Notation in the thesis	Value
Edge length of the computational cube	d	0.32 mm
Interface thickness	$\sim \epsilon$	2.56 μm
max num of levels		4
Smallest grid spacing	h	0.4 μm
Geometry of the pillars	edge length	$5h = 2\,\mu m$
	height	$30h = 12\,\mu m$
	lateral distance	$45h = 18\,\mu m$
Volume increments	$\delta\mathcal{V}$	$-0.1\,\mu l$

Chapter 3

Hysteresis of the contact angle

3.1 A phenomenological model for contact angle hysteresis

Topographical and chemical imperfection on the solid surface at the sub-micron scale generate frictional forces that are able to pin the contact line. This is the origin of the phenomenon of *contact angle hysteresis* (see [16, Chapter 3]), namely, the possibility that equilibrium drops adopt contact angles different from the one given by Young's law (2.6). We focus on quasi-static evolutions, namely, evolutions through equilibria driven either by slowly varying time-dependent constraints (as in the case of an evaporating droplet), or by slowly varying time-dependent external forces (as in the case of a drop subject to gravity and resting on a surface which is initially horizontal and then tilted), or both. In these cases, solutions at time t depend not only on the instantaneous values of the data, but also on their entire time history. We approach such problems by defining a one-parameter family of incremental minimization problems in which, based on the knowledge of the unknowns at time t, we determine their values at time $t + \delta t$, with δt small.

Following [2, 19], we begin by considering the following discrete incremental formulation for the problem of quasistatic evolution of a drop whose volume changes according to the prescribed law $|\omega| = \mathcal{V}(t)$. For simplicity, we neglect gravity in this first example, i.e., we set $G = 0$ in (2.2), and we illustrate the behavior of a small droplet on a horizontal solid surface. Given the configuration $\omega^*(t)$ of a drop at time t, the one at time $t + \delta t$ is given by

$$\omega^*(t + \delta t) = \operatorname*{argmin}_{|\omega| = \mathcal{V}(t+\delta t)} \{E(\omega) + D(\omega, \omega^*(t))\} \tag{3.1}$$

where E is capillary energy defined in Section 2 and the dissipation $D(\omega_1, \omega_2)$ is given by

$$D(\omega_1, \omega_2) = \mu |\partial_S \omega_1 \triangle \partial_S \omega_2|. \tag{3.2}$$

Here $\alpha \triangle \beta = (\alpha \setminus \beta) \cup (\beta \setminus \alpha)$ denotes the symmetric difference of the sets α and β; $\mu > 0$ is a parameter giving the dissipated energy per unit variation of the wetted area. Clearly δt must be chosen sufficiently small, so that small changes of the time-dependent data (in this case, the prescribed volume) occur during one time-step.

For $\omega^*(t)$ a spherical cap, energy and dissipation can be written simply as

$$E = (\sigma_{SL} - \sigma_{SV})\pi a^2 + \sigma_{LV} A \tag{3.3}$$

$$D(\omega_1, \omega_2) = D(a_1, a_2) = \mu\pi |a_1^2 - a_2^2| \tag{3.4}$$

where $A = 2\pi Rh$ is the area of the spherical cap of radius R and height h, while a is the radius of the wetted area, namely, the interface between the solid and the liquid (see Figure 3.1).

The derivation of optimality condition from (3.1) requires some care because of the non-differentiability of the function $a \mapsto D(a, a^*(t))$ at $a = a^*(t)$, and the presence of the volume constraint. The first difficulty is usually handled using the notion of sub-differential from convex analysis. In order to provide a more intuitive derivation, we write

$$\tfrac{d}{da} D(a, a^*(t)) da = \begin{cases} 2\mu\pi a \, da & \text{if } a = a^*(t),\ da \geq 0 \quad \text{(3.5a)} \\ -2\mu\pi a \, da & \text{if } a = a^*(t),\ da \leq 0 \quad \text{(3.5b)} \end{cases}$$

while, since $a \mapsto D(a, a^*(t))$ is differentiable whenever $a \neq a^*(t)$, we have

$$\tfrac{d}{da} D(a, a^*(t)) da = \begin{cases} 2\mu\pi a \, da & \text{if } a > a^*(t) \quad \text{(3.6a)} \\ -2\mu\pi a \, da & \text{if } a < a^*(t) \quad \text{(3.6b)} \end{cases}$$

with da of arbitrary sign. In addition, we observe that the volume constraint

$$\frac{\pi}{6}(3a^2 h + h^3) = \frac{\pi h^2}{3}(3R - h) = given$$

constrains variations of R, h and a, so that

$$dh = -\frac{a}{R} da, \quad dR = \left(1 - \frac{2a}{h}\right) dh = -\left(1 - \frac{2a}{h}\right) \frac{a}{R} da.$$

We thus obtain

$$dA|_{|\omega| = \mathcal{V}(t+\delta t)} = 2\pi(R - h)\frac{a}{R} da = 2\pi a \cos\theta da \tag{3.7}$$

Using (3.5), (3.6) and (3.7) in the unilateral minimality condition

$$dE|_{|\omega|=\mathcal{V}(t+\delta t)} + \frac{d}{da}D(a, a^*(t))da \geq 0$$

which must hold for every admissible pair (a, da), we deduce the following inequalities

$$2\pi a(\sigma_{SL} - \sigma_{SV} + \sigma_{LV}\cos\theta + \mu)da \geq 0 \begin{cases} \forall\, da, & \text{if } a > a^*(t) \\ \forall\, da \geq 0, & \text{if } a = a^*(t) \end{cases}$$

$$2\pi a(\sigma_{SL} - \sigma_{SV} + \sigma_{LV}\cos\theta - \mu)da \geq 0 \begin{cases} \forall\, da \leq 0, & \text{if } a = a^*(t) \\ \forall\, da, & \text{if } a < a^*(t) \end{cases}$$

leading to

$$\begin{aligned} &\cos\theta_Y + \cos\theta + \mu = 0 && \text{if } a > a^*(t) \\ &\left.\begin{aligned} &\cos\theta_Y + \cos\theta + \mu \geq 0 \\ &\cos\theta_Y + \cos\theta - \mu \leq 0 \end{aligned}\right\} && \text{if } a = a^*(t) \\ &\cos\theta_Y + \cos\theta - \mu = 0 && \text{if } a < a^*(t) \end{aligned}$$

This shows that the drop contact angle θ satisfies

$$\cos\theta \in \begin{cases} \{\cos\theta_R\} & \text{if } a < a(t) \quad (3.8a) \\ [\cos\theta_R, \cos\theta_A] & \text{if } a = a(t) \quad (3.8b) \\ \{\cos\theta_A\} & \text{if } a > a(t) \quad (3.8c) \end{cases}$$

where the *advancing contact* θ_A and the *receding contact angle* θ_R are given by

$$\cos\theta_A = \cos\theta_Y - \frac{\mu}{\sigma_{LV}},$$

$$\cos\theta_R = \cos\theta_Y + \frac{\mu}{\sigma_{LV}}.$$

The meaning of condition (3.8) is the following. Any value of the contact angle θ such that $\cos\theta \in [\cos\theta_R, \cos\theta_A]$ can be seen in an equilibrium configuration. However, at a point of the contact line which is advancing (resp., receding), the contact angle must be θ_A (resp., θ_R). Using these angle conditions, and the fact that a drop which is initially a spherical cap always remains a spherical cap, the solutions to (3.1) can be computed analytically for any given volume history $t \mapsto \mathcal{V}(t)$. A pictorial representation of the histories $t \mapsto a(t)$ and $t \mapsto \theta(t)$ resulting from a non-monotone history of prescribed volumes $t \mapsto \mathcal{V}(t)$ is shown in Figure 3.2.

The use of incremental minimization problems to study the quasistatic evolution

of a dissipative system is quite common in solid mechanics and, in particular, in plasticity theory ([37, 40, 52]). This can be regarded as an extension to the case of non-smooth dissipative potentials (such as (3.5) and (3.6)) of the Rayleigh dissipation principle of Classical Mechanics ([33, 55]).

In applying this principle to wetting problems we are neglecting the viscous dissipation in the fluid. The problem of coupling bulk dissipation with the one occurring at the contact line has been considered, e.g., in [44, 46, 51]. We neglect the viscous dissipation in the fluid because we are considering problems in which time-dependence is introduced by slowly varying data. These produce histories of configurations where fluid velocities and viscous dissipation are vanishingly small. These configurations will approach a history of equilibria with volume $t \mapsto \mathcal{V}(t)$ and under "loads" $t \mapsto G(t)$, in the quasistatic limit of infinitely slow changes of prescribed volume $\mathcal{V}$ and loads G. Because of the non-uniqueness introduced by the non-smooth dissipation potential, and reflected by the existence of an interval of stable contact angles (3.8b), solutions will not only depend on the instantaneous values of the data, but also on their entire time history. A more rigorous discussion of the mathematical properties of this model can be found in [2].

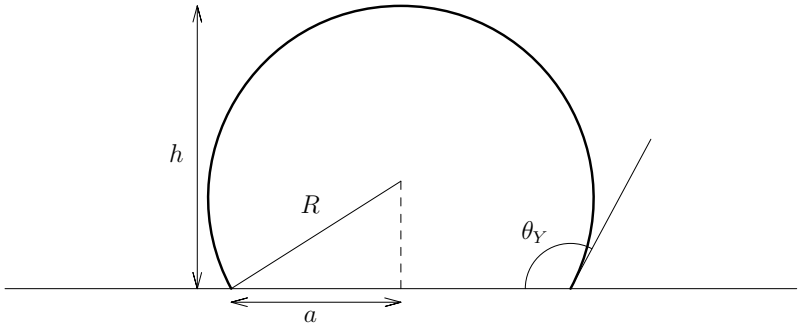

Figure 3.1: *Sketch of a spherical cap.*

Considering now the general case (2.2), in which time-dependent external forces may be present, we look for solutions $\omega = \omega^*(t + \delta t)$ minimizing the functional:

$$E(\omega, t + \delta t) + D(\omega, \omega^*(t)) \tag{3.9}$$

where

$$\begin{aligned} E(\omega, t + \delta t) &= (\sigma_{SL} - \sigma_{SV})|\partial_S \omega| + \sigma_{LV}|\partial_V \omega| + \int_\omega G(x, t + \delta t) dV_x \\ D(\omega, \omega^*(t)) &= |\partial_S \omega \triangle \partial_S \omega^*(t)| \end{aligned}$$

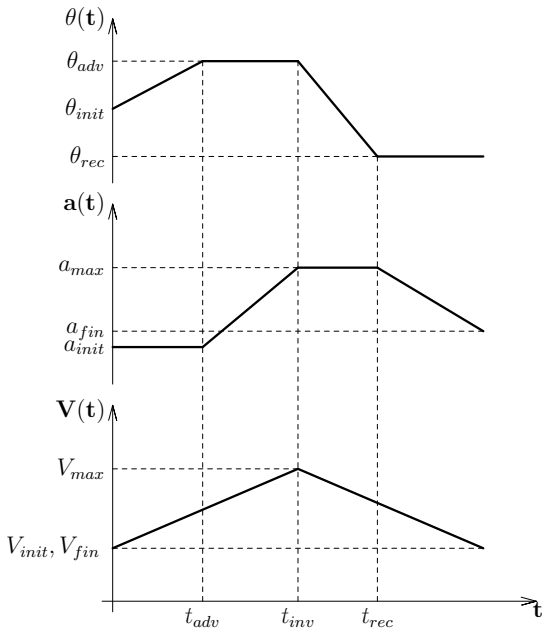

Figure 3.2: *Contact angle $\theta(t)$ and wetted area radius $a(t)$ resulting from a non-monotone history of prescribed volumes $\mathcal{V}(t)$.*

among all configurations ω with volume $|\omega| = \mathcal{V}(t+\delta t)$, using the phase field method discussed in the previous section. In practice, this means to solve

$$\phi_\epsilon^*(t+\delta t) = \operatorname{argmin}\left\{ E_\epsilon(\phi, t+\delta t),\ \text{subject to} \int_\Omega \phi = \mathcal{V}(t+\delta t) \right\} \tag{3.10}$$

with

$$-2\epsilon \frac{\partial \phi_\epsilon^*}{\partial n} = \begin{cases} N_A & \text{on } \partial\Omega_A^\epsilon \\ N_R & \text{on } \partial\Omega_R^\epsilon \end{cases} \tag{3.11}$$

where N_A and N_R are the Neumann boundary conditions associated with the advancing and receding angle respectively, computed by the use of (2.9). The regions $\partial\Omega_R^\epsilon$ and $\partial\Omega_A^\epsilon$ are ϵ-approximations of the parts of the solid which are wet and dry at time t, defined as appropriate super- and sub-level sets of $\phi_\epsilon^*(t)$.
The Dirichlet boundary conditions case is completely similar, imposing the suitable values on $\partial\Omega_A^\epsilon$ and $\partial\Omega_R^\epsilon$ by the use of the equation (2.8).

We remark that (3.10)-(3.11) can be regarded as the phase field formulation of a standard capillarity problem on a heterogeneous surface whose properties are, however, "time-dependent". In view of this remark, the numerical scheme presented in Section 3 can be easily adapted to the incremental problem introduced above in order to model contact angle hysteresis. Within one time increment δt, the external loads and the constraints are frozen at their value at time t. We can obtain that the

drop advance (resp., recede) with contact angle θ_A (resp., θ_R) by imposing through eq. (3.11) that in the regions that are dry (resp., wet) at time $t + \delta t$ the contact angle be the advancing (resp., the receding) one, as shown in Figure 3.2, in the case of a spherical cap.

Thus, our algorithm is easily adapted to accommodate the presence of frictional forces at the contact line: we solve a one-parameter family of standard capillarity problems obtained by replacing the Neumann boundary condition (2.10b) by (3.11), in which $\partial\Omega_A^\epsilon$ and $\partial\Omega_A^\epsilon$ are ϵ-approximations of the parts of the solid which are dry and wet at time t.

Our first application of this algorithm is the study of the volume-driven evolution of a spherical cap in the presence of hysteresis. This is a benchmark case for which an exact solution is available, as discussed above. We run simulations with Neumann boundary conditions associated with the following parameters: $\theta_Y = 120°$, $\theta_A = 135°$, $\theta_R = 105°$. Figures 3.3 and 3.4 show a satisfactory agreement with the known analytical solutions. Notice, in particular, that the solution is continuous across patches with different levels of mesh refinement.

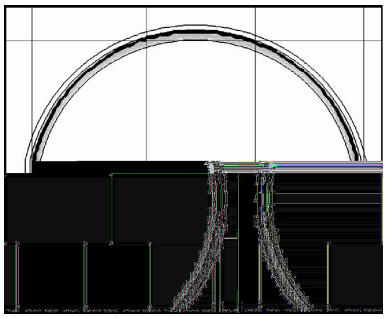

Figure 3.3: *A slice of an advancing drop and the sub-division of the computational domain into patches. The thick line represents the analytical solution of the associated problem, the thin lines are the level curves of the phase function.*

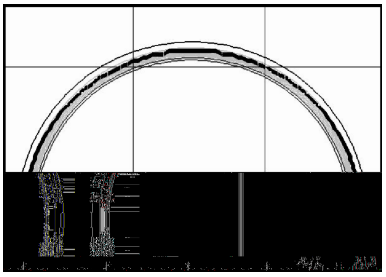

Figure 3.4: *A slice of a receding drop. The phase field solution (thin lines) is compared with the analytical one (thick line).*

3.2 Vertical plate experiments

Consider, for the sake of simplicity, the two-dimensional geometry of Fig.3.5. The drop is in equilibrium if

$$\rho g A + \sigma_{LV} \cos\theta_A - \sigma_{LV} \cos\theta_R \leq 0, \tag{3.12}$$

where we recall that σ_{LV} is the surface tension (now more conveniently interpreted as a force per unit length), ρ is the liquid density, g is gravity acceleration, and θ_A and θ_R are the advancing and the receding contact angles. These are the maximal and minimal contact angle the drop can exhibit in equilibrium, at the onset of advancing and receding motion of the contact line. The maximum value A_{crit} of A compatible with (3.12) is

$$A_{crit} = \frac{\sigma_{LV}}{\rho g} \left(\cos\theta_R - \cos\theta_A\right). \tag{3.13}$$

Formula (3.13) prompts two remarks. The first is that necessary condition for adhesion is that $\cos\theta_R \neq \cos\theta_A$ (this implies that Young's law is violated, i.e. the drop in Fig. 3.5 is not a stationary point for the energy of capillary surfaces). The second one is that the critical area is proportional to the difference $(\cos\theta_R - \cos\theta_A)$.

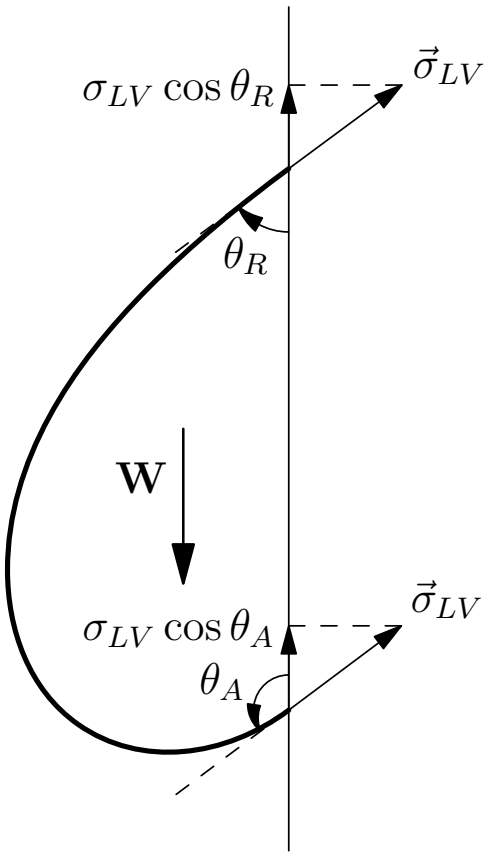

Figure 3.5: *Forces on a capillary drop. The drop can stick if gravity is balanced by surface tension forces. This is possible only if the drop can exhibit different contact angles at the receding and at the advancing edge.*

The three dimensional case, which is the one of interest for applications, is more complex. Dussan describes in [21] the critical configuration of a drop on a tilted

plane, with small hysteresis (i.e. $\cos\theta_R - \cos\theta_A$ small), by studying its dynamics in the limit of vanishing gravitational force. In this way, he estimates that the largest drop that can stick to the surface of the solid inclined at a given angle γ is

$$\mathcal{V}_{crit} \sim \left(\frac{96}{\pi}\right)^{\frac{1}{2}} \left(\frac{\sigma_{LV}(\cos\theta_R - \cos\theta_A)}{\rho g \sin\gamma}\right)^{\frac{3}{2}} \frac{(1+\cos\theta_A)^{\frac{3}{4}}\left(1 - \frac{3}{2}\cos\theta_A + \frac{1}{2}\cos^3\theta_A\right)}{(\cos\theta_A + 2)^{\frac{1}{2}}\,(1-\cos\theta_A)^{\frac{3}{4}}}. \tag{3.14}$$

The 3/2 power in the second factor in the right hand side of (3.14) is obvious from dimensional analysis. However, the critical volume depends on $\cos\theta_R$ and $\cos\theta_A$ not only through their difference, but also through a non-dimensional correction factor depending on $\cos\theta_A$ alone.

Interestingly, experimental results by Carre and Shanahan [12] are available for critical volumes of water drops in equilibrium on differently treated vertical glasses plates. By simulating numerically drops of increasing volume, we can estimate the maximal size a drop can have before gravity wins over pinning forces and obtain a very stringent test of our model. This is done below, where we compare our computational results with the data in [12] and with those deduced by the application of Dussan's formula (3.14).

As it is common in the study of hysteretic evolutions, solutions depend not only on the instantaneous value of the data, but also on their entire time history and, in particular, on the initial conditions. Our protocol to initialize the simulations is the following. We first set $\theta_A = \theta_Y = \theta_R$, where the value of θ_Y is taken from the data in [12], and let the system relax to an equilibrium configuration in the absence of gravity. In these conditions, the equilibrium configuration of the drop is a spherical cap meeting the solid surface at an angle given by Young's law. Then we "switch on" gravity and hysteresis simultaneously, and record whether the drop remains in equilibrium with the full value of the gravitational force, or it starts sliding. A typical equilibrium configuration of a drop, just before it starts sliding is shown in Figure 3.6.

The meaning of the confidence interval we have used to present our results is the following: the minimum value of the specified range is the volume of the largest drop that we have observed to be stable; the maximum is the size of the smallest drop we saw rolling down. The critical volume belongs to this interval. The level of accuracy reached in this evaluation depends mostly on the computational time spent to reduce the error that affects the solution. A preliminary version of these

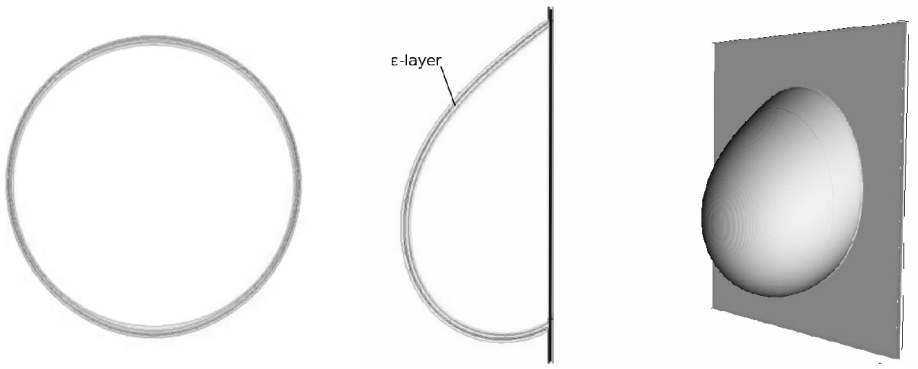

Figure 3.6: *A phase field drop: a slice parallel and close to the solid surface (left), a slice perpendicular to the solid (center) and a 3D snapshot (right). Note the ϵ-layer representing the liquid-vapor interface.*

Table 3.1: *Parameters used in the vertical plate simulations.*

Description	Notation in the thesis	Value
Edge length of the computational cube	d	Variable between 3 mm and 7 mm
Interface thickness	$\sim \epsilon$	$0.005 \cdot d$
max num of levels		3
Smallest grid spacing	h	$0.00125 \cdot d$

calculations has been presented in [18]. We have now narrowed considerably the width of our confidence interval, and obtained a more precise estimate of the critical volume.

In Table 3.2 we report the contact angles measured for water drops on the different materials, subjected to several surface treatments. Table 3.3 shows the critical volume obtained with the different approaches, which are also plotted in Figure 3.7 as a function of $(\cos\theta_R - \cos\theta_A)$.

Looking at Figure 3.7, the agreement of the experimental data with both Dussan's formula and with our numerical simulations is satisfactory. In particular, with reference to (3.14), it is interesting to observe that, in a 3-D framework, the threshold on the volume beyond which motion can start doesn't depend only on the difference

Table 3.2: *Contact angle data (θ_Y, θ_A, θ_R) for untreated glass plates (control) and those treated with a commercial anti-rain composition (CAC) and with the Corning surface treatment (CST), before and after ageing in boiling water and before and after ageing in running water.*

Glass treatment	No ageing	After 1 hr in $100°C$–H_2O	After 30 hr in running water
Control	$\theta_Y = 42.5$ $\theta_A = 51$ $\theta_R = 32.5$	$\theta_Y = 51.5$ $\theta_A = 61$ $\theta_R = 41$	$\theta_Y = 44$ $\theta_A = 54$ $\theta_R = 32$
CAC	$\theta_Y = 108$ $\theta_A = 113$ $\theta_R = 103$	$\theta_Y = 72$ $\theta_A = 91$ $\theta_R = 51$	$\theta_Y = 96.3$ $\theta_A = 111$ $\theta_R = 82$
CST	$\theta_Y = 105$ $\theta_A = 111$ $\theta_R = 99.5$	$\theta_Y = 99.5$ $\theta_A = 105$ $\theta_R = 94$	$\theta_Y = 103$ $\theta_A = 113$ $\theta_R = 94$

Table 3.3: *Critical volume data in μl; $\mathcal{V}_c^D$ is the one deduced from Dussan's formula (3.14), $\mathcal{V}_c^E$ is the experimental value and $\mathcal{V}_c^C$ is our computational result.*

Glass treatment	No ageing	After 1 hr in $100°C$–H_2O	After 30 hr in running water
Control	$\mathcal{V}_c^D = 6.34$ $\mathcal{V}_c^E = 4.9$ $\mathcal{V}_c^C \in (5.12, 5.45)$	$\mathcal{V}_c^D = 7.68$ $\mathcal{V}_c^E = 6.3$ $\mathcal{V}_c^C \in (6.15, 6.51)$	$\mathcal{V}_c^D = 7.92$ $\mathcal{V}_c^E = 6.5$ $\mathcal{V}_c^C \in (5.12, 5.45)$
CAC	$\mathcal{V}_c^D = 1.83$ $\mathcal{V}_c^E = 1.5$ $\mathcal{V}_c^C \in (0.89, 1.01)$	$\mathcal{V}_c^D = 19.74$ $\mathcal{V}_c^E = 17.7$ $\mathcal{V}_c^C \in (16.25, 17.03)$	$\mathcal{V}_c^D = 9.89$ $\mathcal{V}_c^E = 8.6$ $\mathcal{V}_c^C \in (9.13, 9.67)$
CST	$\mathcal{V}_c^D = 2.56$ $\mathcal{V}_c^E = 1.8$ $\mathcal{V}_c^C \in (1.14, 1.27)$	$\mathcal{V}_c^D = 2.55$ $\mathcal{V}_c^E = 2.0$ $\mathcal{V}_c^C \in (1.42, 1.58)$	$\mathcal{V}_c^D = 4.95$ $\mathcal{V}_c^E = 4.0$ $\mathcal{V}_c^C \in (3.03, 3.29)$

$(\cos\theta_R - \cos\theta_A)$ like in the 2-D scheme, but also on a second term, a correction factor which depends on θ_A. Using a Taylor expansion centered in $\frac{\pi}{2}$ and defined for convenience on the interval $[50°, 120°]$ (that is the range where θ_A varies in our

examples), (3.14) can be rewritten as:

$$\mathcal{V}_{crit} \sim C\,(\cos\theta_R - \cos\theta_A)^{\frac{3}{2}} \left(1 - \frac{3}{4}t + \frac{3}{16}t^2 - \frac{45}{64}t^3\right) \tag{3.15}$$

where $t = (\theta_A - \frac{\pi}{2})$. When the term $\left(1 - \frac{3}{4}t + \frac{3}{16}t^2 - \frac{45}{64}t^3\right)$ is far from 1, namely, when θ_A is far from $\frac{\pi}{2}$, then V_{crit} deviates from the monotone curve $C(\cos\theta_R - \cos\theta_A)^{\frac{3}{2}}$, hence explaining the non-monotone behavior of the data in Figure 3.7.

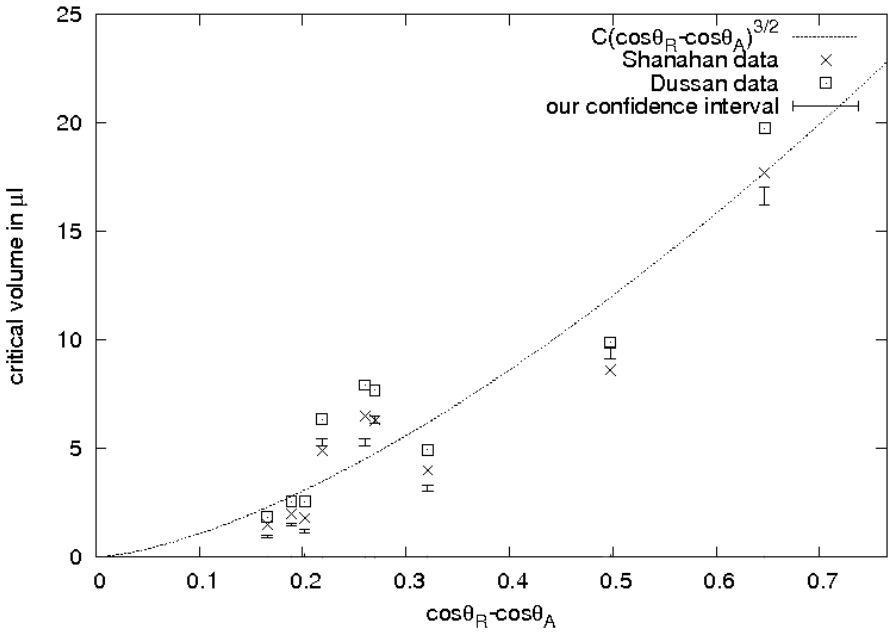

Figure 3.7: *Comparison of the results of simulations based on our model with the experimental data in [12] and with Dussan's formula (3.14).*

Chapter 4

Evaporating droplet on pillars: quasi-Newton methods and continuation methods

We present in this section the numerical results obtained for the phase field simulation of a drop that is decreasing its volume, while resting on a substrate of micro-pillars. Differently from the experiment performed in Chapter §2, we would like to follow its entire evolution and apply the quasi-static procedure, in which the configuration at an intermediate step depends directly on the one before it. The computational complexity involved and some technical difficulties, like the update of the changing volume parameter, require for the use of new numerical devices and of a complete restyle of the strategy for the solution of the stationarity condition for the functional (2.7). In particular we would like to solve directly the equation (2.10a) without the implementation of the fictitious descent dynamics. Clearly we are now in the case of a system of non linear equations and this demands for the use of Newton-like methods. Furthermore multigrid techniques on a locally refined grid and a special scheme (continuation method) for the updating of the initial guess at each step of the evolution are presented.

4.1 Motivations

What we would like to show in this section is an overview of the methods and possible strategies could be adopted in order to solve the equilibrium equation for (2.10); in particular it would be interesting to point out pros and cons of the different

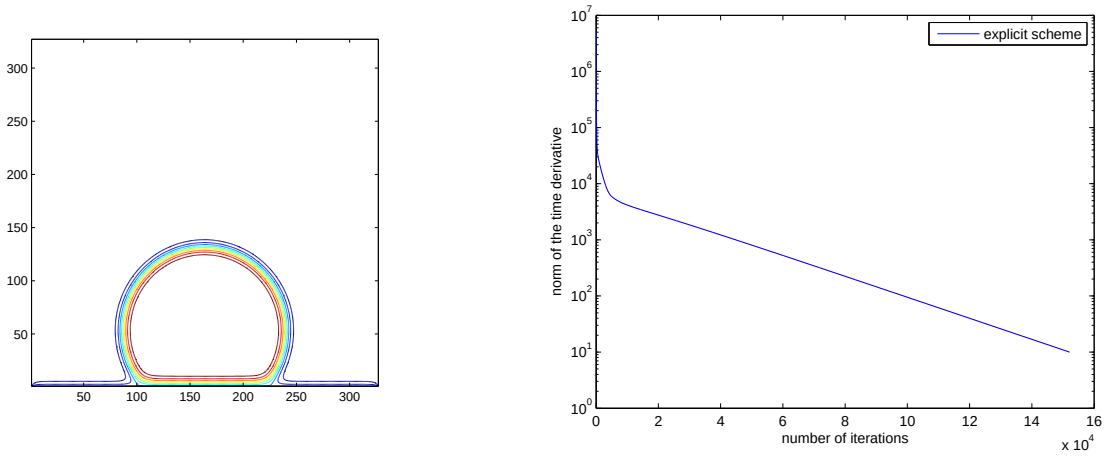

Figure 4.1: *In the left the contour lines of a two dimensional phase field drop are represented. The right panel shows the convergence history for the explicit Euler-method. The x-axis represents the number of the iterations performed while the y-axis the norm of the time-derivative*

approaches, and then collect all these informations in order to choose the instruments that could provide a stable, accurate and fast strategy.

The leading experiment we perform throughout the section and that we use as benchmark for the comparison is the one of a drop in contact with an homogeneous solid, with no additional external forces. For convenience the grid has 327 nodes in each direction. Furthermore we found of interest to choose as grid space $h = 0.00125$ and in (2.7), $\epsilon = 0.004$: values close to these ones provide the right resolution for the description of wetting phenomena on rough surfaces.

The first method we take in exam is the explicit Euler, we have used in Chapter §2. If one implements a gradient flow, a solution for (2.10) can be recovered, and following this approach the equation has to be solved is:

$$\phi_\tau = \epsilon \triangle \phi - \frac{1}{\epsilon}\phi(1-\phi)(1-2\phi) - \lambda. \tag{4.1}$$

The scheme we have used for the resolution is the one described in Section 2.2.1, in which we provided a splitting strategy for the calculation of the Lagrange multiplier. The criterion we have taken into account to measure the order of convergence relies on the norm of the discrete time derivative

$$\left\| \frac{\phi^{N+1} - \phi^N}{d\tau} \right\|$$

in which $d\tau$ is the time-step that leads the evolution. If we recall the estimate on the maximum time-step allowed for the stability of the explicit Euler method (2.12), we

get that the parameters we have chosen, impose $d\tau \leq 0.000032$. As consequence a high number of iterations are requested in order to get an admissible approximation of the solution (Figure 4.1). This obviously influences also the effective time needed for the simulation, and, in particular, we have spent about 2500 wall clock seconds to perform the benchmark experiment.

Following [14], methods based on a semi-implicit splitting, in which linear leading order terms are extracted and discretized implicitly are very effective when dealing with Cahn-Hilliard type equations as (4.1). Amohmark13(the)-3icug27(e)-3clasionsof semi-implicng

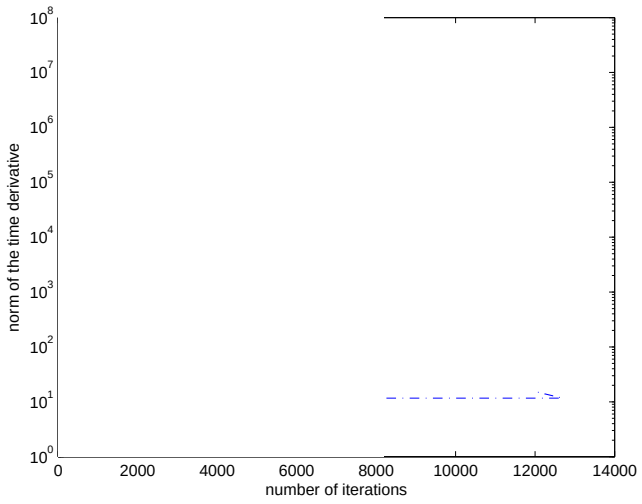

Figure 4.2: *In this picture we show the performance of the* SBDF *scheme and the improvement obtained when it is coupled with a multigrid technique.*

ever slower on domains whose boundary $\partial\Omega$ is highly irregular as in the case of simulations of micro-textured solids. In particular, some experiments have pointed out that both the speed of convergence and the amplitude of $d\tau$ are penalized.
Since the non-linearity is quite simple (a polynomial in ϕ) and affects only the the lowest order terms, it seems reasonable the application of Newton methods directly to the Euler-Lagrange equations:

$$\begin{cases} -\epsilon\triangle\phi + \frac{1}{\epsilon}\phi(1-\phi)(1-2\phi) + \lambda = 0 \\ \\ \int_\Omega \phi = \mathcal{V} \end{cases} \tag{4.4}$$

If now we use as stopping criterion the norm

$$\left\| -\epsilon\triangle\phi + \frac{1}{\epsilon}\phi(1-\phi)(1-2\phi) + \lambda \right\|$$

we have noticed that the Newton iterations converge very quickly (about 130 seconds and 18 iterations) to the numerical solution of (4.4) (Figure 4.3). The requirement (that a priori cannot be satisfied) on the initial guess to be close enough to the exact solution makes the method unstable (the intermediate steps oscillate before they converge to the right solution). Furthermore iterative solvers (e.g. conjugate gradient) needed for the solution of the linear system associated with the Newton step, converge slowlier (and in some cases just diverge) because of the values assumed by the derivative of the non linear term $g(\phi) = \frac{1}{\epsilon}\phi(1-\phi)(1-2\phi)$ (this will be

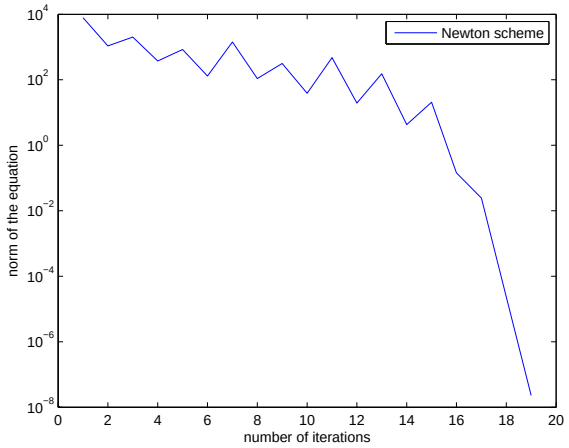

Figure 4.3: *Convergence history of Newton method applied to the equation* (4.4)

discussed more in details in the next section). These considerations suggest for the replacement of the Newton method with a proper quasi-Newton one.

4.2 Numerical formulation of the problem

For simplicity our description, and the basic results we are going to state, are thought in two dimensions and on a uniform square grid, since the three dimensional case and the study on a locally refined grid would require a deeper investigation that is outside from the purposes of the work. At this level we would like to put attention on the numerical reasons that also in the simplest cases taken in consideration have motivated the choice to move from Newton methods to quasi Newton schemes, and to justify, at least from an heuristic point of view, the advantages of the proposed method.

4.2.1 The Newton method

In order to solve numerically (4.4), we use finite differences to approximate the Laplacian operator. Then, the discretized system deriving from (4.4) is:

$$\begin{cases} -\frac{\epsilon}{h^2} L \cdot \phi + \frac{1}{\epsilon} g(\phi) + \lambda C = 0 \\ \\ C^T \cdot \phi - \mathcal{V} = 0 \end{cases} \tag{4.5}$$

where h is the grid space (for simplicity it is the same in each direction), $g(\phi)$ is the vector whose i-th value is given by the evaluation of the non linear term in the i-th

node, C is a vector with all components equal to 1 (notice that we have rescaled the second equation for convenience) and L is the usual three-block diagonal matrix arising from the use of finite differences (see [49]). So we have a non linear system of equations F_h in the unknown $\psi = \begin{bmatrix} \phi \\ \lambda \end{bmatrix}$ and we want to find

$$F_h(\psi) = 0. \tag{4.6}$$

The $k+1$ step of the Newton method is defined as:

$$\psi^{k+1} = \psi^k - J_h^{-1}(\psi^k) F_h(\psi^k) \tag{4.7}$$

where J_h is the Jacobian operator of F_h. Writing (4.6) in vector form we have

$$F_h(\psi^k) = \begin{pmatrix} -\frac{\epsilon}{h^2}L & C \\ C^T & 0 \end{pmatrix} \cdot \begin{pmatrix} \phi^k \\ \lambda^k \end{pmatrix} + \begin{pmatrix} +\frac{1}{\epsilon}g(\phi^k) \\ -\mathcal{V} \end{pmatrix}. \tag{4.8}$$

The linear system deriving from (4.7), in the unknown $\delta\phi^k$ (i.e. the correction to be supplied at the $(k+1)$-th iteration) is

$$J_h(\psi^k)\delta\psi^k = -F_h(\psi^k)$$

that is, looking at (4.8):

$$\begin{pmatrix} -\frac{\epsilon}{h^2}L + \frac{1}{\epsilon}g'(\phi^k)I & C \\ C^T & 0 \end{pmatrix} \cdot \begin{pmatrix} \delta\phi^k \\ \delta\lambda^k \end{pmatrix} = - \begin{pmatrix} -\frac{\epsilon}{h^2}L \cdot \phi^k + \frac{1}{\epsilon}g(\phi^k) + \lambda^k C \\ C^T \cdot \phi^k - \mathcal{V} \end{pmatrix} \tag{4.9}$$

where for convention $\frac{1}{\epsilon}g'(\phi^k)I$ is a diagonal matrix with values $\frac{1}{\epsilon}g'(\phi^k)$. If we call $B^k := -\frac{\epsilon}{h^2}L + \frac{1}{\epsilon}g'(\phi^k)I$, $v^k := -\frac{\epsilon}{h^2}L \cdot \phi^k + \frac{1}{\epsilon}g(\phi^k) + \lambda^k C$ and $p^k := C^T \cdot \phi^k - \mathcal{V}$, (4.9) becomes:

$$\begin{cases} B^k \cdot \delta\phi^k + \delta\lambda^k C = -v^k \\ C^T \cdot \delta\phi^k = -p^k \end{cases} \tag{4.10}$$

Performing the trivial substitutions, we obtain:

$$\begin{cases} \delta\phi^k = (B^k)^{-1}(-v^k - \delta\lambda^k C) \\ C^T \cdot [-(B^k)^{-1}v^k - (B^k)^{-1}(\delta\lambda^k C)] = -p^k \end{cases} \tag{4.11}$$

From the second equation we get:

$$\delta\lambda^k = \frac{p^k - C^T(B^k)^{-1}v^k}{C^T(B^k)^{-1}C}$$

If we call $x_1 = (B^k)^{-1}v^k$ and $x_2 = (B^k)^{-1}(C)$, finally we obtain:

$$\delta\phi^k = -x_1 - \delta\lambda^k x_2$$

Then the numerical core of the problem is to find the solution of the two linear systems:

$$B^k x_1 = v^k \tag{4.12}$$

$$B^k x_2 = C \tag{4.13}$$

that are the discrete versions of two elliptic equations.
From the theory we know that, if we denote with ψ^* a solution for (4.6), the Newton method locally converges with quadratic rate of convergence if $\exists\, r > 0$ and a neighborhood $N(\psi^*, r)$ such that in N the operator J_h is Lipschitz and if $J_h(\psi^*)$ is invertible.
What we want to do now is to establish sufficient conditions for the local convergence of the Newton method applied to our equation. For this purpose we will use the l_1 vector norm and the matrix norm induced by it.
If $v \in \mathrm{R}^n$ and $A = (a_{ij}) \in \mathrm{R}^{n\times n}$:

$$\|v\|_1 = \sum_{i=1}^{n} |v_i|$$

$$\|A\|_1 = \max_{1\le j\le n} \{\|a_{.j}\|_1\}$$

Here $a_{.j}$ denotes the $j-$th column of A. Then the induced l_1 matrix norm is the maximum of the l_1 vector norm of the columns of A.

Definition 4.2.1. *Let $n > 0$, $G : \mathrm{R}^n \longrightarrow \mathrm{R}^{n\times n}$, $x \in \mathrm{R}^n$, let $\|\cdot\|$ a norm on R^n, and $|||\cdot|||$ a norm on $\mathrm{R}^{n\times n}$. G is said to be Lipschitz continuous at x if there exists an open set $D \subset \mathrm{R}^n$, $x \in D$ and a constant γ such that for all $v \in D$,*

$$|||G(v) - G(x)||| \le \gamma\|v - x\|. \tag{4.14}$$

If (4.14) holds for every $x \in D$, then $G \in \mathrm{Lip}_\gamma(D)$.

Proposition 4.2.1. *If D is any bounded set in R^n, then $J_h : \mathrm{R}^n \longrightarrow \mathrm{R}^{n\times n}$ is Lipschitz continuous in $\forall\psi^1 \in D$, with respect to the l_1 vector norm and the induced matrix norm.*

Proof. If we take ψ^1, $\psi^2 \in D$ we have the following chain of inequalities (where c_i are suitable constant):

$$\begin{aligned}
\|J_h(\psi^1) - J_h(\psi^2)\|_1 &= c_1 \| \underbrace{g'(\phi^1)I - g'(\phi^2)I}_{G} \|_1 = \max_{1\le j\le n-1} \|\{G_{\cdot j}\}\| \\
&= \max_{1\le j\le n-1} \{|g'(\phi_j^1) - g'(\phi_j^2)|\} \\
&\le c_1 \max_{s\in D} |g''(s)| \max_{1\le j\le n-1} |\phi_j^1 - \phi_j^2| \\
&\le c_2 \max_{1\le j\le n} |\psi_j^1 - \psi_j^2| \le c_2 \|\psi^1 - \psi^2\|_\infty \\
&\le c_3 \|\psi^1 - \psi^2\|_1
\end{aligned}$$

□

Proposition 4.2.2. *Let $\psi^c = (\phi^c, \lambda^c)$ the (continuous) solution of the equation (4.4) and denote with $J_h(\psi^c)$ the discrete Jacobian matrix evaluated in ψ^c. Then there exists a neighborhood N_ϵ of $\hat{\epsilon} = 1$ where $J_h(\psi^c)$ is invertible.*

Proof. If by contradiction $J_h(\psi^c)$ is not invertible, there would be a non null $x = (x', x_n) \in \mathrm{R}^n$ (with x' we denote its first $n-1$ components), such that:

$$\begin{pmatrix} \tilde{L} & C \\ C^T & 0 \end{pmatrix} \cdot \begin{pmatrix} x' \\ x_n \end{pmatrix} = \begin{pmatrix} 0 \\ 0 \end{pmatrix}$$

where $\tilde{L} = -\epsilon L + \frac{1}{\epsilon} g'(\phi^c) I$. This means that

$$\begin{cases} \tilde{L} \cdot x' + x_n C = 0 \\ C^T \cdot x' \overset{\Rightarrow}{=} 0 \end{cases}$$

Then, since $-L$ is positive definite (it has positive eigenvalues, [8]), and $|g'(\phi^c)| \leq 1$, if we indicate with $\lambda_{\min}$ the smallest magnitude eigenvalue of $-L$ (that on a square domain is equal to $8\sin^2\left(\frac{\pi\epsilon^\alpha}{2}\right)$), we get:

$$\begin{aligned} v^T\big(-L+\epsilon^{2(\alpha-1)}g'(\phi^c)I\big)v &= -v^TLv + v^T\epsilon^{2(\alpha-1)}g'(\phi^c)Iv \\ &\geq \lambda_{\min} - \epsilon^{2(\alpha-1)} = 8\sin^2\left(\frac{\pi\epsilon^\alpha}{2}\right) - \epsilon^{2(\alpha-1)} \end{aligned} \tag{4.15}$$

The last term in (4.15) can be written as

$$\frac{8\sin^2\left(\frac{\pi\epsilon^\alpha}{2}\right)}{(\epsilon^\alpha)^2} - \frac{1}{\epsilon^2}. \tag{4.16}$$

For $\epsilon = 1$, (4.16) is > 0, and for continuity the statement is true. □

Remark 4.2.1. Notice that for $\epsilon \to 0$, (4.16) $\to -\infty$.

Remark 4.2.2. If we refer to [45], thanks to the Lipschitz continuity of the Jacobian operator J_h, the consistence of the problem and a simple stability requirement on $J_h(\psi^c)^{-1}$ that can be derived from Lemma 4.2.3 (see Section 4.2.2), we can assess the existence of a solution ψ^* of the discrete problem (4.5) and also derive an estimate on $\|\psi^c - \psi^*\|$. Furthermore, with arguments similar to the ones used in Proposition 4.2.2, it could be proved also the invertibility of $J_h(\psi^*)$. In this conditions we would have convergence of Newton method and also numerical stability when solving the linear systems (4.12) and (4.13). Unfortunately for $\epsilon \approx 1$ the phase field energy does not describe properly the transition layer between liquid and vapor, and the grid space $h = \epsilon^\alpha$ is absolutely inadequate for a good resolution of the approximated solution. Actually, the values we used to perform our tests do not ensure the desired properties, on the contrary it can be calculated numerically that with the usual values we take for our simulations (i.e. $\epsilon \propto 10^{-3}$, $h = \epsilon/2$), the iteration matrix B^k has negative eigenvalues. In these cases Newton method is no longer stable, and it could diverge.
From now on, we would have to suppose the existence of a solution of (4.5) and the non-singularity of its Jacobian, and in order to stabilize numerically the problem, we would move to quasi Newton methods.

4.2.2 The proposed method

If one has the system of non-linear equations $F : \mathrm{R}^n \longrightarrow \mathrm{R}^n$ continuously differentiable, the basic idea of quasi Newton methods is to provide an approximation

A to the real Jacobian matrix of F, J, and use it at each iteration. The reasons to do this can be of different nature: in cases as ours this is useful for numerical stability issues, but in other situations it could happen that J is not available (and one has to estimate it by finite differences), or in cases when the Jacobian matrix is very huge, it is convenient to calculate only how it acts on vectors, and also this process gives raise to approximations. Obviously, the introduced deterioration not only does not change the local nature of the method (the initial guess must be still close enough to the real solution), but in almost the cases the quadratic convergence is compromised.
Following [17], the algorithm is:

QUASI-NEWTON ALGORITHM FOR NONLINEAR EQUATIONS

Given $F : \mathrm{R}^n \longrightarrow \mathrm{R}^n$ continuously differentiable , and $x_0 \in \mathrm{R}^n$.
At each iteration k:

1. Compute $F(x_k)$, if it is not already done. and decide whether to stop or continue.
2. Compute A_k to be $J(x_k)$ or an approximation to it.
3. Apply a factorization technique to A_k and estimate its condition number. If A_k is ill-conditioned, perturb it in appropriate manner.
4. Solve $A_k s_k^N = -F(x_k)$.
5. Decide whether to take a Newton step, $x_{k+1} = x_k + s_k^N$, or to choose x_{k+1} by a global strategy. This step often furnishes $F(x_k)$ to step 1.

We will focus our attention on the second step of the procedure. Since the crucial point in our numerical implementation is that $\frac{1}{\epsilon}g'(x) = \frac{1}{\epsilon}(6x^2 - 6x + 1)$ can assume negative values (it has minimum -$\frac{1}{2\epsilon}$ for $x = \frac{1}{2}$), and this is the reason why, unless choosing suitable ϵ and h, B^k looses its positive definiteness, we propose to weaken

the non-linearity under a certain threshold $K \leq 0$, that is we consider:

$$\frac{1}{\epsilon}\bar{g}'(x) = \begin{cases} \frac{1}{\epsilon}g'(x) & \text{if} \quad \frac{1}{\epsilon}g'(x) > K \\ \\ K & \text{otherwise} \end{cases} \tag{4.17}$$

Then the approximation A_k to $J(\psi^k)$ we are considering is:

$$A_k = \begin{pmatrix} -\frac{\epsilon}{h^2}L + \frac{1}{\epsilon}\bar{g}'(\phi^k)I & C \\ \\ C^T & 0 \end{pmatrix}. \tag{4.18}$$

We will show that, if K is chosen in a proper way, the quasi Newton-method converges. However we will give also an heuristic motivation of the fact that whatever $K \leq 0$ we choose for the approximation of the Jacobian, the quasi Newton-method converges towards a zero of (4.6).

Definition 4.2.2. *Let $x^* \in \mathrm{R}^n$, $k = 0, 1, 2, ...$ Then the sequence $x_k = x_0, x_1, x_2, ...$ is said to be* q-linearly convergent *to x^* if there exists a constant $c \in [0, 1)$ and an integer $\hat{k} > 0$ such that $\forall\ k > \hat{k}$*

$$\|x_{k+1} - x^*\| \leq c\|x_k - x^*\|$$

Lemma 4.2.3. *Let $\|\cdot\|$ be any norm on $\mathrm{R}^{n\times n}$ such that $\|XY\| \leq \|X\|\|Y\|$ and $\|I\| = 1$, and let $E \in \mathrm{R}^{n\times n}$. If $\|E\| < 1$, then $(I - E)^{-1}$ does exist and*

$$\|(I - E)^{-1}\| \leq \frac{1}{1 - \|E\|}.$$

If Y is non singular and $\|Y^{-1}(X - Y)\| < 1$, then X is non singular and

$$\|X^{-1}\| \leq \frac{\|Y^{-1}\|}{1 - \|Y^{-1}(X - Y)\|}$$

Lemma 4.2.4. *Let $F : \mathrm{R}^n \longrightarrow \mathrm{R}^n$ be continuously differentiable in the open convex set $D \subset \mathrm{R}^n$, $x \in D$, and let J be Lipschitz continuous at x in the neighborhood D, using a vector norm and the induced matrix operator norm and the constant γ. Then for any $x + p \in D$,*

$$\|F(x + p) - F(x) - J(x)p\| \leq \frac{\gamma}{2}\|p\|^2.$$

Proposition 4.2.3. *Assume that there exists ψ^* such that $F_h(\psi^*) = 0$ and $J_h(\psi^*)^{-1}$ exists with $\|J_h(\psi^*)^{-1}\|_1 \leq \beta$. Then there exist $\eta > 0$, $K > -\frac{1}{2\epsilon}$ and $\psi^0 \in N(\psi^*, \eta)$ such that if A_k is defined as in* (4.18)*, the sequence generated by*

$$\psi^{k+1} = \psi^k - A_k^{-1}F_h(\psi_k)$$

is well defined and converges q-*linearly to ψ^*.*

Proof. The proof is similar to that of Theorem 5.4.1 in [17]. Let us denote with γ the Lipschitz constant of J_h and let $M > 0$ be such that:

$$\|A_0 - J_h(\psi^0)\|_1 = \max_{1\leq j\leq n-1}\{|K - \frac{1}{\epsilon}g'(\phi_j^0)|\} \leq M \tag{4.19}$$

Then we will choose η and K so that

$$\beta(\eta\gamma + 2M) \leq \frac{1}{2}.$$

We will show by induction on k that at each step

$$\|\psi^{k+1} - \psi^*\| \leq \frac{1}{2}\|\psi^k - \psi^*\| \tag{4.20}$$

For $k = 0$ first let us prove that A_0 is non-singular. From the triangular inequality, the Lipschitz continuity of J_h and $\|\psi^0 - \psi^*\| < \eta$, we get

$$\begin{aligned}\|J_h(\psi^*)[A_0 - J(\psi^*)]) &\leq \|J_h(\psi^*)\|\,\|[A_0 - J_h(\psi^0)] + [J_h(\psi^0) - J_h(\psi^*)]\| \\ &\leq \beta(M + \gamma\eta) \leq \frac{1}{2}\end{aligned}$$

From Lemma 1 we get that A_0 is non singular and $\|(A_0)^{-1}\| \leq 2\beta$. Therefore ψ^1 is well defined and:

$$\begin{aligned}\psi^1 - \psi^* = A_0^{-1}A_0(\psi^0 - \psi^*) - A_0^{-1}F_h(\psi^0) + A_0^{-1}F_h(\psi^*)+ \\ + A_0^{-1}J_h(\psi^0)(\psi^* - \psi^0) - A_0^{-1}J_h(\psi^0)(\psi^* - \psi^0)\end{aligned}$$

Therefore, by the use of Lemma 2

$$\begin{aligned}\|\psi^1 - \psi^*\| &\leq \|A_0^{-1}\|\,\left[\|F_h(\psi^*) - F_h(\psi^0) - J_h(\psi^0)(\psi^* - \psi^0)\| + \|A_0 - J_h(\psi^0)\|\|\psi^* - \psi^0\|\right] \\ &\leq 2\beta\left[\frac{\gamma}{2}\|\psi^* - \psi^0\|^2 + M\|\psi^0 - \psi^*\|\right] \\ &\leq (\beta\gamma\eta + 2\beta M)\|\psi^0 - \psi^*\| \leq \frac{1}{2}\|\psi^0 - \psi^*\|.\end{aligned}$$

The proof of the induction step is completely similar. □

4.2.3 Nonlinear systems and unconstrained minimization problem

Given the system of non linear equations

$$F : \mathrm{R}^n \longrightarrow \mathrm{R}^n \tag{4.21}$$

the problem of finding x^* such that $F(x^*) = 0$ can be seen as the corresponding unconstrained minimization problem

$$\min_{x\in\mathrm{R}^n} f(x) = \frac{1}{2}F(x)^T F(x) \tag{4.22}$$

Note that each 0 of (4.21) is a solution for (4.22), but in general the symmetric relation is not true. Given a point x_t, a descent direction for (4.22) in x_t is any direction p for which $\nabla f(x_t) \cdot p < 0$, where the j-th component of the vector $\nabla f(x_t)$ is given by

$$[\nabla f(x_t)]_j = \frac{\partial}{\partial x_j} \sum_{i=1}^{n} \frac{1}{2}(F_i(x_t))^2 = \sum_{i=1}^{n} \left[\frac{\partial}{\partial x_j} F_i(x_t) \right] \cdot F_i(x_t) = [J(x_t)^T \cdot F(x_t)]_j$$

where again $J(x_t)$ is the Jacobian of F in x_t. Therefore, the steepest-descent direction for (4.22) is along $-J(x_t)^T F(x_t)$. Furthermore, the Newton direction along $s = -J(x_t)^{-1} F(x_t)$ is a descent one, since

$$\nabla f(x_t)^T \cdot s = -F(x_t)^T J(x_t) J(x_t)^{-1} F(x_t) = -F(x_t) \cdot F(x_t) < 0 \tag{4.23}$$

as long as $F(x_t) \neq 0$.

These considerations are used to widen the domain of convergence of Newton methods exploiting several techniques developed in the field of unconstrained minimization [17]. For our aims it is interesting to point out, that in almost total the cases described in literature (for instance Broyden's method), quasi-Newton approximation A of the Jacobian operator J defines a direction $s = -A^{-1}(x_t)F(x_t)$, that even if it is not guaranteed to be a descent direction, actually does not change property (4.23). In particular, in small experiments where the calculation of the inverse is not too much computational challenging, we numerically tested that (4.18) keeps setting a descent direction for (4.7). These benchmark experiments tell us that in general the quasi-Newton method we implemented, provides a Jacobian approximation that is not too far from the real one.

4.3 The Continuation method

4.3.1 Introduction to the scheme

As stressed several times so far, Newton methods converge to a solution x^* of $F(x) = 0$ only if the initial approximation is sufficiently close to x^*. The *continuation method* may be considered as an attempt to widen the domain of convergence of a given method, or, alternatively, as a procedure to obtain sufficiently close starting points. Furthermore, in typical scientific and engineering problems not only a single isolated nonlinear system is to be solved, but a family of problems depending on one or more parameters $\gamma \in \mathrm{R}^p$, $p \geq 1$. We can suppose $p = 1$. In fact, parameter dependent

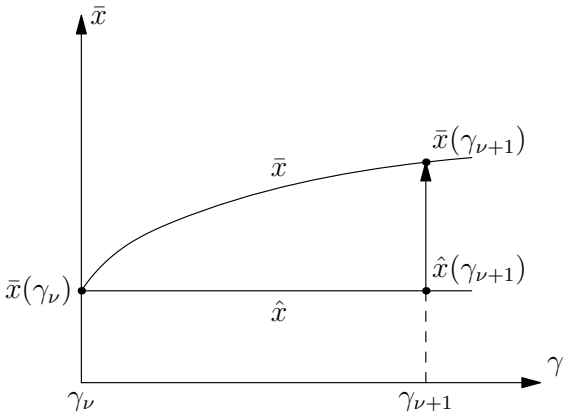

Figure 4.4: *Classic continuation method*

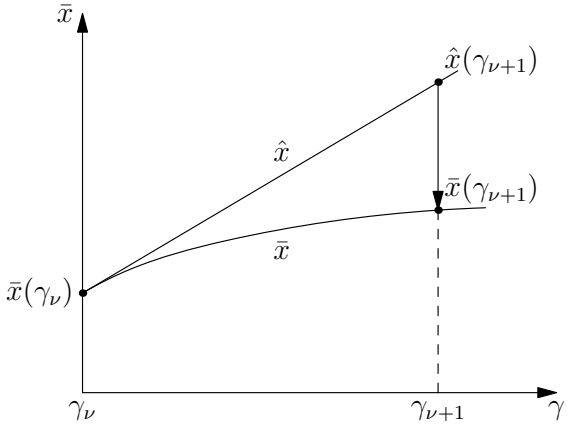

Figure 4.5: *Tangent continuation method*

systems of nonlinear equations

$$F(x,\gamma) = 0,\ x \in D \subset \mathrm{R}^n,\ \gamma \in [0, L] \tag{4.24}$$

are the basis for *parameter studies* in *systems analysis* and *systems design*, but, as anticipated, if one provides suitable modifications when F does not depend naturally on some parameter γ, can also be differently exploited for the globalization of local Newton or Gauss-Newton methods, if only poor initial guesses are available (see [20, 42] for a complete presentation).
In order to treat the problem family (4.24) a sequence of problems

$$F(x,\gamma_\nu) = 0, \quad \nu = 0, 1, .., \tag{4.25}$$

is solved instead, where the interval $[0, L]$ is replaced by the subdivision

$$0 = \gamma_0 < \gamma_1 < \cdots < \gamma_N = L.$$

In order to solve each problem (4.25) by a local Newton method, "sufficiently good" starting points are required, which should be supplied by some suitable *prediction method*. Formally speaking, any starting points will lie on some prediction path $\hat{x}(\gamma)$ for $\gamma = \gamma_\nu$. Then the local Newton method would work as a *correction method* that, from the given starting point $\hat{x}(\gamma_\nu)$ supplies a solution $\overline{x}(\gamma_\nu)$. The task therefore involves the choice of a suitable prediction method.
The first and most natural way to provide a starting point $\hat{x}(\gamma_{\nu+1})$ is just take the previous solution point $\overline{x}(\gamma_\nu)$. This is the so-called *classical continuation method* and the prediction path for it is defined as

$$\hat{x}(\gamma) = \overline{x}(\gamma_\nu), \quad \gamma \geq \gamma_\nu$$

A refinement of the above idea is to proceed along the tangent of the path $\bar{x}$ in γ_ν. This is the so-called *tangent continuation method*, sometimes also called *method of incremental load* or *Euler continuation*, and the prediction path is defined by

$$\hat{x}(\gamma) = \overline{x}(\gamma_\nu) + (\gamma - \gamma_\nu)\dot{\overline{x}}(\gamma_\nu), \;\; \gamma \geq \gamma_\nu \tag{4.26}$$

wherein

$$\dot{\overline{x}}(\gamma_\nu) = -F_x\left(\overline{x}(\gamma_\nu), \gamma_\nu\right)^{-1} F_\gamma\left(\overline{x}(\gamma_\nu), \gamma_\nu\right) \tag{4.27}$$

4.3.2 Application to quasi-static evolution of droplets

Continuation method is a natural approach for the study of the family of discrete incremental problems described in Chapter §2. In particular, if we think of the case of an evaporating drop on a substrate of micropillars, the driving parameter for (4.24) is the volume $\mathcal{V}$. Following the classical continuation method, in which the initial guess for the $N+1-th$ step is given by the solution at the $N-th$ step, the change of volume led to dramatic deteriorations on the solution: even for small variation of the loading parameter we had instability around the region of the contact line, drop was prone to spring up from the pillars, loosing the informations about the wetting history stored previously.

Tangent continuation method has revealed the right tool for the updating of the initial guess, once the volume was decreased. In particular, as for the description of the phenomenological model in Chapter §3, we are following the quasi-static evolution of a drop whose volume changes according to a prescribed law $|\omega| = \mathcal{V}(t)$ with $t \in [0,1]$; $\mathcal{V}(1)$ is the decreased final volume we want to reach.

In order to simplify the notation, we leave the dependence on ϵ, even if now we are looking at a solution $\phi^*_\epsilon(t+\delta t)$ as in (3.10). If we consider (4.4) and suppose the differentiability in t of $\phi(t)$ and $\lambda(t)$ we can write:

$$\begin{cases} -\epsilon\triangle\dfrac{\partial\phi}{\partial t} + \dfrac{1}{\epsilon}g(\phi(t))\dfrac{\partial\phi}{\partial t} + \dfrac{\partial\lambda}{\partial t} = 0 \\ \\ \displaystyle\int_\Omega \frac{\partial\phi}{\partial t} = \frac{\partial\mathcal{V}}{\partial t} \end{cases} \tag{4.28}$$

We now replace the interval $[0,1]$ in a subdivision

$$0 = t_{in} < \cdots < t_N < t_{N+1} \cdots < t_{fin} = 1$$

and call

$$\frac{\partial\phi}{\partial t} = y, \quad dt = (t_{N+1} - t_N) \quad \text{and} \quad \frac{\partial\lambda}{\partial t} = \mu$$

Following (4.26) and (4.27), if we indicate with ϕ_0 and λ_0 the couple solution at time 0 in the evolution, a good initial guess for $\phi(t_{N+1})$ and $\lambda(t_{N+1})$ will be given by

$$\begin{cases} \phi(t_{N+1}) = \phi(t_N) + dt \cdot y(t_N) \\ \phi(0) = \phi_0 \end{cases} \qquad \begin{cases} \lambda(t_{N+1}) = \lambda(t_N) + dt \cdot \mu(t_N) \\ \lambda(0) = \lambda_0 \end{cases} \tag{4.29}$$

where $y(t_N)$ and $\mu(t_N)$ are the couple solution of the system

$$\begin{cases} -\epsilon \triangle y + \dfrac{1}{\epsilon} g(\phi(t_N)) y + \mu = 0 \\ \\ \displaystyle\int_\Omega y = \frac{\partial \mathcal{V}}{\partial t}(t_N) \end{cases} \tag{4.30}$$

4.4 The multigrid structure and SAMRAI

The purpose of testing the model and the numerical method with experiments as much as possible close to reality (i.e. to take in consideration 3D experiments) requires for the use of adaptive mesh refinement (AMR) techniques in order to increase the spatial resolution only in special region of the domain. This approach favors both a more clever use of the computational resources and a better description of the solution where it is needed. In particular, the extremely different length scales we have to take into account for wetting phenomena on substrates heterogeneous at microscopic scale and the particular structure of the phase-field drop (constant on the entire domain but in a narrow region of width proportional to ϵ) enforce this necessity. Structured adaptive mesh refinement (SAMR) is an AMR strategy in which the computational mesh is organized as a hierarchy of nested levels, each one composed by the union of logically rectangular regions (patches) (see also Section 2.2.3). Let

$$h = \bigcup_{k=0}^{L-1} h_k$$

denote a set of mesh spacing such that $h_{k+1} \leq h_k$. If we call Ω^{h_k} the set of the patches at the same resolution h_k a SAMR grid can be represented in the following way:

$$\Omega^{h_0} \supset \Omega^{h_1} \cdots \supset \Omega^{h_{L-1}}$$

where Ω^{h_0} covers the entire computational domain and Ω^k is the hierarchy till the level k (therefore $\Omega^{L-1} \equiv \Omega^h$ is the entire hierarchy). The solution is defined only in the cells that have not been refined, that is only on $\Omega^{h_{L-1}}$ and in the subregions

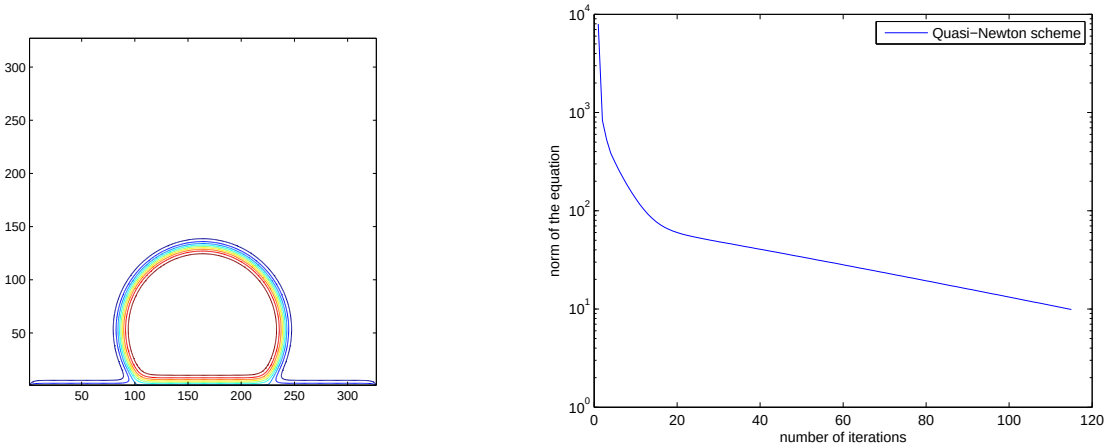

Figure 4.6: *In the left the contour lines of the two dimensional phase field drop are represented. The right panel shows the convergence history for the proposed method. As usual, the x-axis represents the number of the iterations performed.*

of each level Ω^h

FAC ALGORITHM

INITIALIZE $r^h = f^h - \mathcal{L}^h u^h$

FOR $k = L-1, ..., 1$ {
  SET $f^{h_k} = \mathcal{I}_k^{h_k} r^k$
  SOLVE/SMOOTH $\mathcal{L}^{h_k} u^{h_k} = f^{h_k}$
  CORRECT $u^k = u^k + \mathcal{I}_{h_k}^k u^{h_k}$
  UPDATE $r^k = f^k - \mathcal{L}^k u^k$
  }
SOLVE $\mathcal{L}^{h_0} u^{h_0} = f^{h_0}$

FOR $k = 1, ..., L-1$ {
  CORRECT $u^k = u^k + \mathcal{I}_{k-1}^k u^{k-1}$
  SET $f^{h_k} = \mathcal{I}_k^{h_k}(f^k - \mathcal{L}^k u^k)$
  SOLVE/SMOOTH $\mathcal{L}^{h_k} u^{h_k} = f^{h_K}$
  CORRECT $u^k = u^k + \mathcal{I}_{h_k}^k u^{h_k}$
  }

Notice that FAC only provides a general scheme for the solution of a partial differential equation on a hierarchical domain and the operations included within the procedure (such as interpolation/prolongation operator, type of iterative solver used for the smoothing step) depend on the particular multigrid solver. In details, the operators $\mathcal{I}_{k-1}^k : \Omega^k \longrightarrow \Omega^{k-1}$ play the role of prolongation in classical multigrid, since they interpolate data in $\Omega^{h_k} \cap \Omega^{h_{k-1}}$ (at level h_{k-1}) to Ω^{h_k}; additional transfer operators $\mathcal{I}_k^{h_k} : \Omega^k \longrightarrow \Omega^{h_k}$ and $\mathcal{I}_{h_k}^k : \Omega^{h_k} \longrightarrow \Omega^k$, serve to extract a level from Ω^k and insert a level into Ω^k. These are only operations of copying but for the filling of the ghost cells (a layer of fictitious nodes that enter in the calculation of the differential operators, see also Section 2.2.3) in the regions where there is a change of resolution. Differently from the case of the explicit resolution scheme, the use of triquadratic interpolation is no longer necessary when filling ghost cells, but it is sufficient the use of linear one.

For solving (4.12) and (4.13) we used an existent package in SAMRAI that imple-

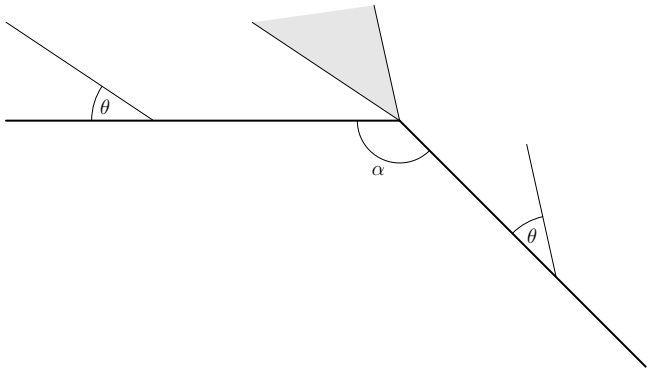

Figure 4.7: *Apparent pinning of a contact line on an edge. The Young condition stipulates that liquid meets the solid with a contact angle θ. Hence the contact angle at the edge can take any value (if the horizontal direction is considered as the reference one) between θ and $\pi - \alpha + \theta$, as illustrated by the colored region.*

ments the method FAC for the resolution on a AMR grid of the Poisson equation

$$-\nabla \cdot (D_1 \nabla u) + D_2 u = f$$

where the vector D_1 represents the diffusion coefficient and the vector D_2 is a cell centered scalar field. The operations of solving and of data moving described in the FAC procedure exploit the methods defined by the SMG (Semicoarsening Multigrid) algorithm introduced by Schaffer [50] which, in the class of multigrid solvers, it is appreciated for its stability and robustness.

4.5 Numerical examples

The first example we would like to show is the benchmark test we have used in Section 4.1 for the comparison of the numerical methods. In Figure 4.6 the convergence history of the proposed method is represented. The result is pretty satisfactory: we have reached the same degree of convergence of the previous simulations with only 104 iterations and and 148 seconds of wall clock computing. In particular we have chosen as threshold to weaken the non linearity $K = (\frac{1}{16\epsilon} \min g(x))$; we can appreciate that the quasi Newton-method is more stable of the pure Newton one (there are no longer dramatic oscillations before reaching a guess that falls toward the zero) but unfortunately, as predicted by theory, the convergence is only linear. The rest of the section is devoted to the presentation of the three dimensional results obtained for real capillary problems with the use of the proposed method and the

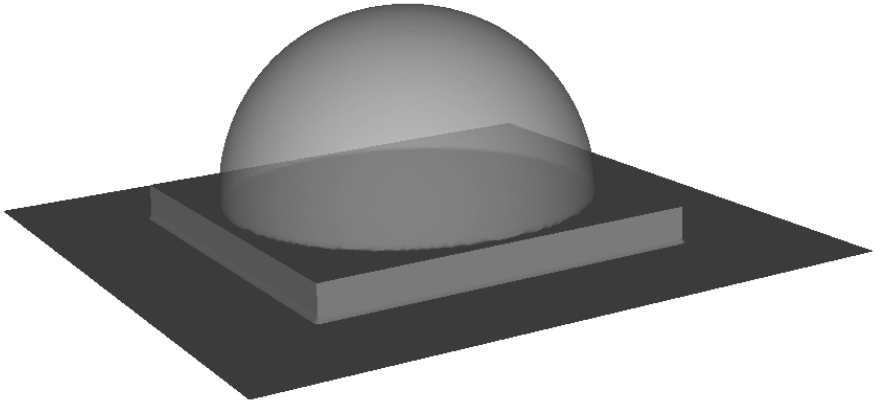

Figure 4.8: *A Drop that is increasing its volume on a basement.*

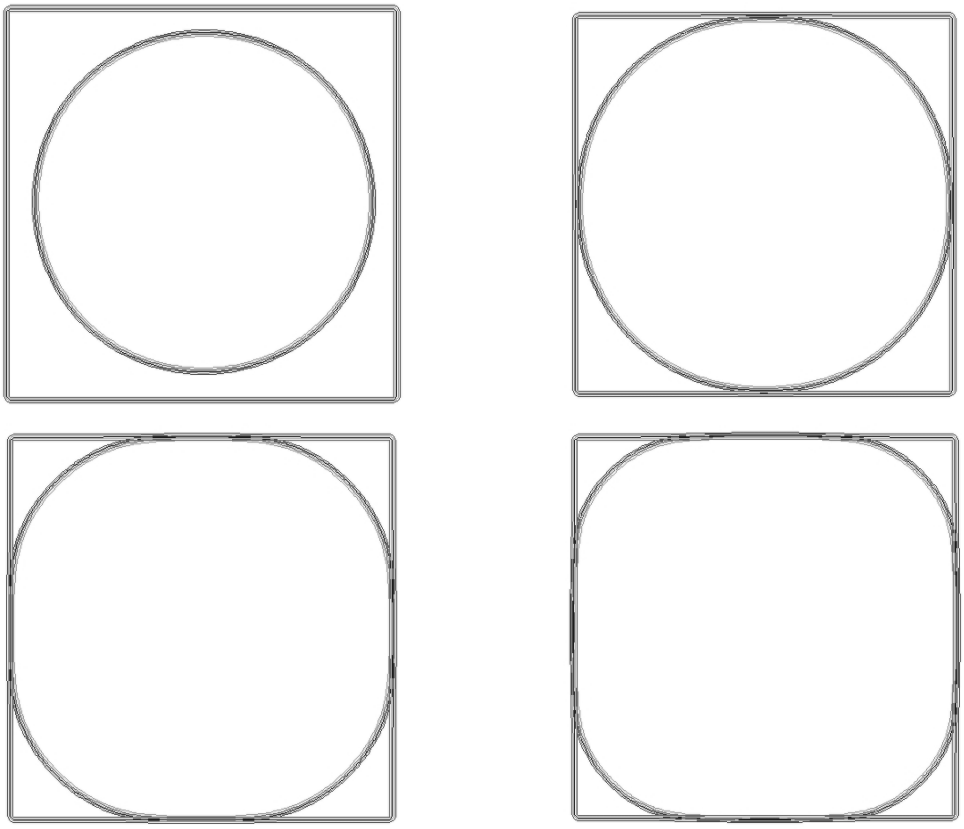

Figure 4.9: *In this sequence of panels the imprint left by the drop during the evolution is represented. Notice the pinning effect of the basement edges, which determines the progressive change in a squared shape of the circular imprint.*

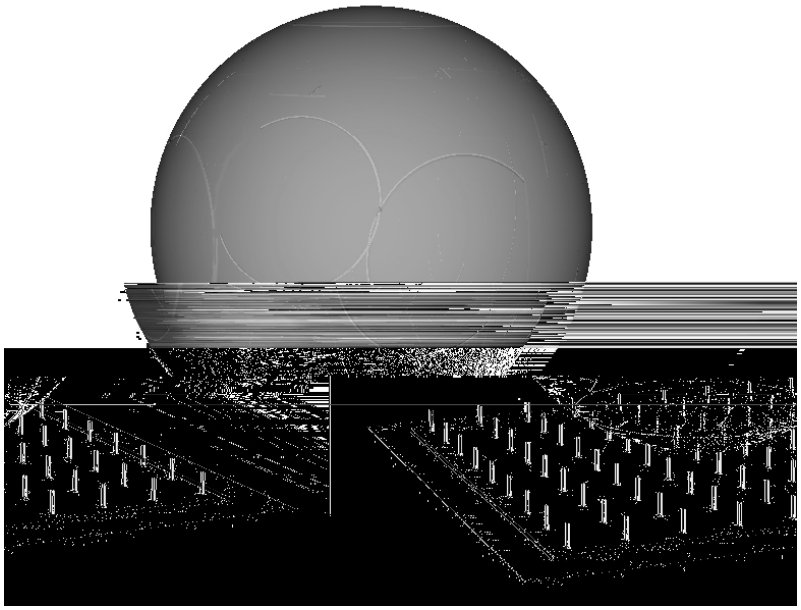

Figure 4.10: *The drop at the begin of the evolution on the micro-pillars.*

described devices. We focus our attention on the effects that geometrically heterogeneous surfaces induce on wetting phenomena. It is well known that defects on a solid can pin a contact line, and as consequence droplets on incline stay at rest. In particular the edge of the defect (of characteristic angle α) makes the contact angle flexible at this place. One measures a (Young) angle θ before the edge and a (Young) angle $\pi - \alpha + \theta$ at the edge (Figure 4.7), considering the horizontal as reference. A groove can thus stop the front of a liquid drop (as if it were non wetting) and a tip will act in the opposite way so that a solid decorated with both kinds of defects yields both small and large apparent angles. The first experiment we show tries to reproduce this effect. In absence of any external forces, we placed a drop over a basement that is upturned with respect to the level of the rest of the solid. The homogeneous condition we put on the solid induces a Young angle of $\theta = 90°$ and the characteristic angle of the defect is $\alpha = 90°$. Then we increased the volume of the drop and looked at the contact line; the imprint that the globule leaves on the substrate is circular till it meets the edge of the basement: here, as willed, the front of the liquid finds a resistance and the value of the (Young) angle begins to increase. The imprint is no longer circular and only the zone at the corners are rounded off. This effect can be appreciated only till the Young angle the drop exhibits is below the threshold $\theta + \alpha = 180°$; once this barrier is exceeded, the globule is able to win

the resistance and begin to flood also over the lateral walls of the basement.

The second experiment we would like to show describes the transition from the Cassie-Baxter state to the Wenzel one of a drop that is evaporating on a substrate of micropillars. In the literature these two models of wetting on rough surfaces are deeply investigated. A drop that is in a Wenzel state fills all the cavities formed by the micro-asperities, that is, follows the profile of the solid. In this situation, the mechanism of the contact line pinning is similar to the one just described, and it should be evident the reason why a drop increasing its volume enhances its static contact angle. Therefore also the hydrophobicity of the solid is increased. Furthermore, if a drop begins to evaporate, the resistance due to the tips, acts in the opposite way: this means that the contact line remains stuck and an enhancement of the hydrophilic properties of the substrate is observable. If the asperities are enough tall, the most favorable energetical configuration is the Cassie-Baxter one, in which, as explained in Chapter §2, the drop rests on the top of the pillars, leaving vapor in the cavities. The increase of the hydrophobic properties is striking and it is not exaggerated to speak of super-hydrophobicity. This state can be recovered even when the minimal energetical configuration is the Wenzel configuration: in these cases Cassie-Baxter drops are metastable, that is, small perturbation of the external conditions are sufficient to produce the collapse of the globule and a recover of the Wenzel state.
We have followed the entire evolution of a drop that, starting from a Cassie-Baxter state, after some evaporation, falls in the cavities. As predicted by the physical model, the mechanism for which this transition is possible relies on a progressive invasion of the liquid between the micro troughs. The simulation of the volume changing has been particularly challenging because of the instability at the level of the contact line, that this process introduces in the numerical drops. However the results is satisfactory; furthermore, also the pinning effects due to the presence of the tips is recovered by our experiments, and the enhancement of the hydrophilicity is observable in the Wenzel state.

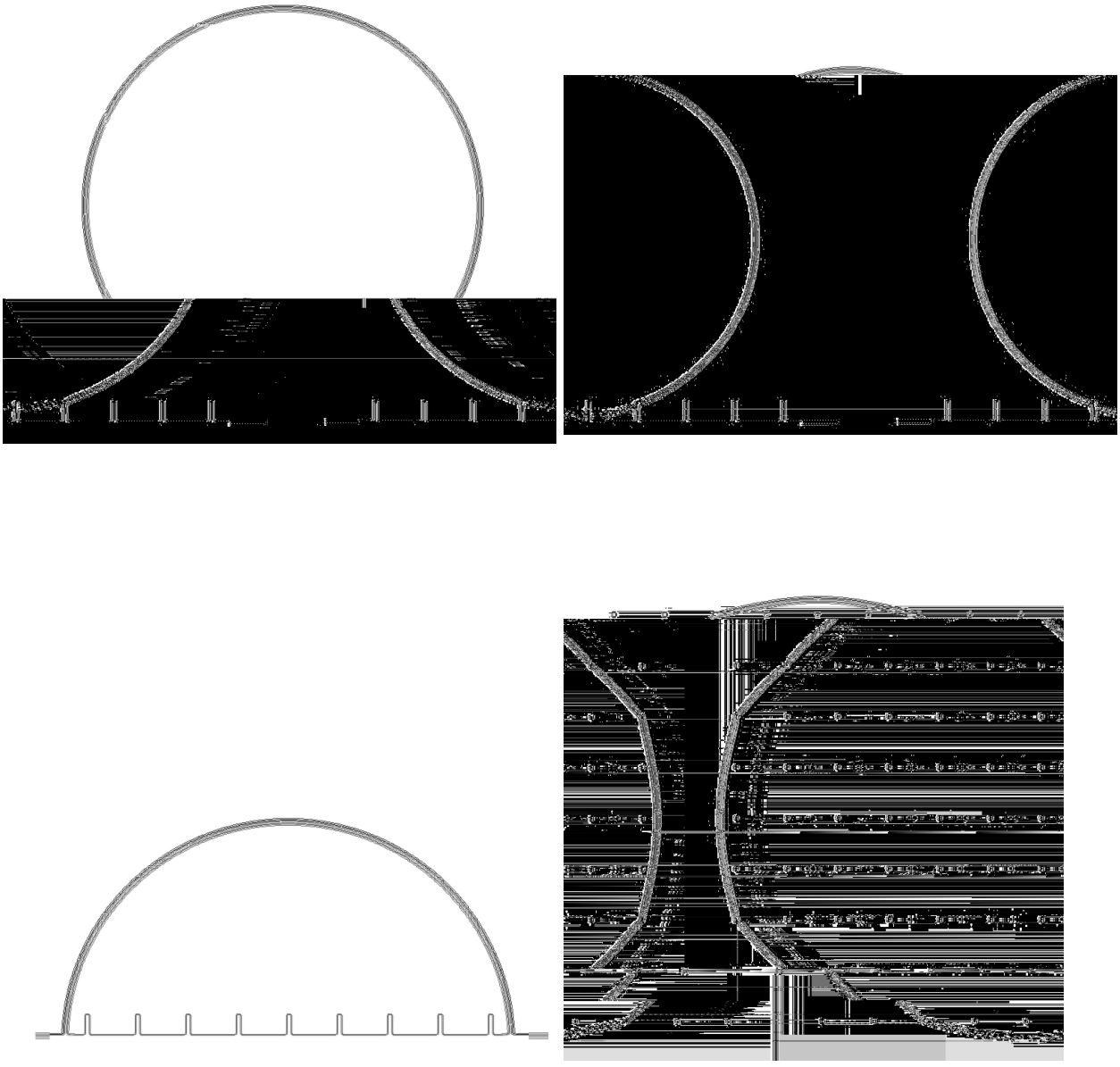

Figure 4.11: *Different sections of the numerical drop during the evaporation. Notice the progressive invasion of the cavities between the pillars that leads toward a sudden collapse in the Wenzel state. In the last picture on the right we can appreciate the pinning effect of the pillars at the level of the contact line with the solid.*

Appendix A

A brief introduction to BV functions

The material we show in this appendix section is taken from the first part of a collection of lecture notes for the study of Total Variation in Image Analysis [15]; Several reviewed here concepts are useful for a better understanding of the material presented in Chapter §1.

A.1 Definition

Let us consider $\Omega \subset \mathrm{R}^N$ any (bounded) open set.

Definition A.1. *The* total variation *of a function is defined by duality: for* $u \in L^1_{\mathrm{loc}}(\Omega)$ *it is given by*

$$J(u) = \sup \left\{ -\int_\Omega u \mathrm{div}\phi \, dx \ : \ \phi \in C_c^\infty(\Omega; \mathrm{R}^N), |\phi(x)| \leq 1 \, \forall x \in \Omega \right\} \qquad (TV)$$

A function is said to have Bounded Variation whenever $J(u) < +\infty$. Typical examples include

- A smooth function $u \in C^1(\Omega)$ (or in fact a function $u \in W^{1,1}(\Omega)$): in this case,
$$-\int_\Omega u \mathrm{div}\phi \, dx = -\int_\Omega \phi \cdot \nabla u \, dx$$
and the sup over all ϕ with $|\phi| \leq 1$ is $J(u) = \int_\Omega |\nabla u| dx$
- The characteristic function of a set with smooth (or $C^{1,1}$) boundary: $u = \chi_E$, in this case
$$-\int_\Omega u \mathrm{div}\phi \, dx = -\int_{\partial E} \phi \cdot \nu_E \, d\sigma$$

and one can reach the sup (which correspond to $\phi = -\nu_E$, the outer normal to ∂E, on $\partial E \cap \Omega$, while $\phi = 0$ on $\partial E \cap \partial\Omega$) by smoothing in a neighborhood of the boundary, the gradient of the signed distance function to the boundary. We obtain that $J(u) = \mathcal{H}^{N-1}(\partial E \cap \Omega)$, the *perimeter* of E in Ω.

Here, $\mathcal{H}^{N-1}$ is the $(N-1)$-dimensional Hausdorff measure, see for instance [25] for details.

A.1.1 An equivalent definition

It is well known that any $u \in L^1_{\text{loc}}(\Omega)$ defines a *distribution*

$$\begin{aligned} T_u : \mathcal{D} &\to \mathrm{R} \\ \phi &\mapsto \int_\Omega \phi(x)u(x)\,dx \end{aligned}$$

where here $\mathcal{D}(\Omega)$ is the space of smooth functions with compact support ($C_c^\infty(\Omega)$) endowed with a particular topology, and T_u is a continuous linear form on $\mathcal{D}(\Omega)$, that is, $T_u \in \mathcal{D}'(\Omega)$. We denote by $\langle T, \phi\rangle_{\mathcal{D}',\mathcal{D}} \in \mathbb{R}$ the duality product between a linear form $T \in \mathcal{D}'$ and a vector $\phi \in \mathcal{D}$. The derivative of T_u is defined as $(i = 1, .., N)$

$$\left\langle \frac{\partial T_u}{\partial x_i}, \phi \right\rangle_{\mathcal{D}',\mathcal{D}} := -\left\langle T_u, \frac{\partial \phi}{\partial x_i} \right\rangle_{\mathcal{D}',\mathcal{D}} = -\int_\Omega u(x)\frac{\partial \phi}{\partial x_i}(x)\,dx$$

(which clearly extends the integration by parts: if u is smooth, then $\partial T_u/\partial x_i = T_{\partial u/\partial x_i}$).We denote by Du the (vectorial) distribution $(\partial T_u/\partial x_i = T_{\partial u/\partial x_i})_{i=1}^N$.
Then, if $J(u) < +\infty$, it means that for all vector field $\phi \in C_c^\infty(\Omega; \mathrm{R}^N)$

$$\langle Du, \phi\rangle_{\mathcal{D}',\mathcal{D}} \le J(u) \sup_{x\in\Omega} |\phi(x)|.$$

This means that Du defines a linear form on the space of continuous vector fields, and by Riesz's representation Theorem it follows that it defines a Radon measure (precisely, a vector-valued (or signed) Borel measure on Ω which is finite on compact sets), which is globally bounded, and its norm (or *variation* $|Du|(\Omega) = \int_\Omega |Du|$) is precisely the total variation $J(u)$.

A.1.2 Main properties of the total variation

Lower semi-continuity The Definition A.1 has a few advantages. It can be introduced for *any* locally integrable function (without requiring any regularity or derivability). But also, $J(u)$ is written as a sup of linear forms

$$L_\phi : u \mapsto -\int_\Omega u(x)\mathrm{div}\phi(x)\,dx$$

which are continuous with respect to very weak topologies (in fact, with respect to the "distributional convergence" related to the space $\mathcal{D}'$ introduced in the previous section).
For instance, if $u_n \rightharpoonup u$ in $L^p(\Omega)$ for any $p \in [1, +\infty)$ (or weakly-$*$ for $p = \infty$), or even in $L^p(\Omega')$ for any $\Omega' \subset\subset \Omega$, then $L_\phi u_n \to L_\phi u$. But it follows that

$$L_\phi u = \lim_n L_\phi u_n \leq \liminf_n J(u_n)$$

and taking then the sup over all the smooth fields ϕ with $|\phi(x)| \leq 1$ everywhere, we deduce that

$$J(u) \leq \liminf_{n\to\infty} J(u_n) \tag{A.1}$$

that is, J is (sequentially) *lower semi-continuous* (l.s.c.) with respect to all the above mentioned topologies. [The idea is that a sup of continuous function is l.s.c.].
Convexity The second fundamental property of J which we deduce from Definition A.1 is its *convexity*: for any u_1, u_2 and $t \in [0, 1]$,

$$J(tu_1 + (1-t)u_2) \leq tJ(u_1) + (1-t)J(u_2). \tag{A.2}$$

It follows, again, because J is the supremum of the linear (hence convex) functions L_ϕ: indeed, one clearly has

$$L_\phi(tu_1 + (1-t)u_2) = tL_\phi(u_1) + (1-t)L_\phi(u_2) \leq tJ(u_1) + (1-t)J(u_2) \tag{A.3}$$

and taking the sup in the left-hand side yields (A.2).
Homogeneity It is obvious for the definition that for each u and $t > 0$,

$$J(tu) = tJ(u)$$

that is, J is positively *one homogeneous*.

A.1.3 Functions with bounded variation

We introduce the following definition:

Definition A.2. *The space BV(Ω) of functions with bounded variation is the set of functions $u \in L^1(\Omega)$ such that $J(u) < +\infty$, endowed with the norm $\|u\|_{BV(\Omega)} = \|u\|_{L^1(\Omega)} + J(u)$.*

This space is easily shown to be a Banach space. It is a natural (weak) "closure" of $W^{1,1}(\Omega)$. Let us state a few essential properties of this space.

Meyers-Serrin's approximation Theorem We first state a theorem which shows that BV function may be "well" approximated with smooth functions. This is a refinement of a classical theorem of Meyers and Serrin [39] for Sobolev spaces.

Theorem A.1. *Let $\Omega \subset \mathrm{R}^N$ be an open set and let $u \in BV(\Omega)$: then there exists a sequence $(u_n)_{n\geq 1}$ of functions in $C^\infty(\Omega) \cap W^{1,1}(\Omega)$ such that*

1. $u_n \to u \quad in\ L^1(\Omega)$
2. $J(u_n) = \int_\Omega |\nabla u_n(x)|dx \to J(u) = \int_\Omega |Du|$ *as* $n \to +\infty$

Let us recall that in Sobolev's spaces $W^{1,p}(\Omega)$, $p < \infty$, the thesis of this classical theorem is stronger, since one proves that $\|\nabla u_n - \nabla u\|_{L^p} \to 0$, while here one cannot expect $J(u_n - u) = \int_\Omega |Du_n - Du| \to 0$ as $n \to \infty$. This is easily illustrated by the following example: let $\Omega = (-1, 1)$, and $u(t) = -1$ if $t < 0, u(t) = 1$ if $t \geq 0$. Then, the sequence $u_n(t) = \tanh(n \times t)$ clearly converges to u, with

$$\int_{-1}^{1} u_n'(t)dt = 2\tanh(n) \to 2 = J(u)$$

as $n \to \infty$, but clearly $J(u_n - u) \approx 4$ for large n. In fact, it is clear if v is any smooth approximation of u such as shown on Figure A.1, then clearly the variation $J(u - v)$ of $w = u - v$ is given by

$$\begin{array}{ccccccc} |w(0^-) - w(-1)| & + & |w(0^+) - w(0^-)| & + & |w(1) - w(0^+)| & = \\ |v(0) - v(-1)| & + & 2 & + & |v(1) - v(0)| & \approx\ 4 \end{array}$$

and cannot be made arbitrarily small.

Rellich's compactness theorem The second important property of BV functions is the following compactness theorem:

Theorem A.2. *Let $\Omega \subset \mathrm{R}^N$ be a bounded domain with Lipschitz boundary, and let $(u_n)_{n\geq 1}$ be a sequence of functions in $BV(\Omega)$ such that $\sup_n \|u_n\|_{BV} < +\infty$. Then there exists $u \in BV(\Omega)$ and a subsequence $(u_{n_k})_{k\geq 1}$ such that $u_{n_k} \to u$ strongly in $L^1(\Omega)$ as $k \to \infty$.*

Sobolev's inequalities We observe here that the classical inequalities of Sobolev:

$$\|u\|_{L^{\frac{N}{N-1}}(\mathrm{R}^N)} \leq C \int_{\mathrm{R}^N} |Du| \tag{A.4}$$

if $u \in L^1(\mathrm{R}^N)$, and Poincaré-Sobolev:

$$\|u - m\|_{L^{\frac{N}{N-1}}(\mathrm{R}^N)} \leq C \int_{\mathrm{R}^N} |Du| \tag{A.5}$$

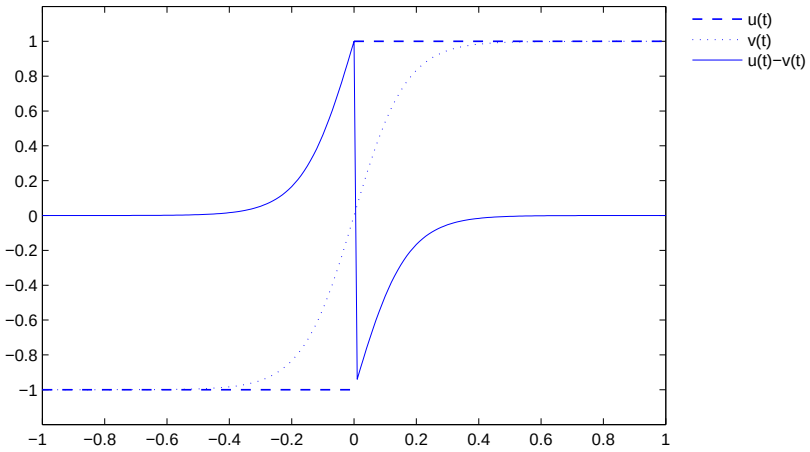

Figure A.1: *Smooth approximation of a step function.*

where Ω is bounded with Lipschitz boundary, and m is the average of u on Ω, valid for $W^{1,1}$ functions, clearly also hold for BV function as can be deduced from Theorem A.1

A.2 The perimeter. Sets with finite perimeter

A.2.1 Definition, and inequality

Definition A.3. *A measurable set $E \subset \Omega$ is a set of finite perimeter in Ω (or Caccioppoli set) if and only if $\chi_E \in BV(\Omega)$. The total variation $J(\chi_E)$ is the perimeter of E in Ω, denoted by $Per(E;\Omega)$. If $\Omega = \mathrm{R}^N$, we simply denote $Per(E)$.*

We observe that a "set" here is understood as a measurable set in R^N, and that this definition of the perimeter makes it depend on E only up to sets of zero Lebesgue measure. In general, in what follows, the sets we will consider will be rather equivalence classes of sets which are equal up to Lebesgue negligible sets.
The following inequality is an essential property of the perimeter: for any $A, B \subseteq \Omega$ sets of finite perimeter, we have

$$Per(A \cup B;\Omega) + Per(A \cap B;\Omega) \leq Per(A;\Omega) + Per(B;\Omega) \tag{A.6}$$

Proof. The proof is as follows: we can consider, invoking Theorem A.1, two sequences u_n, v_n of smooth functions, such that $u_n \to \chi_A$, $v_n \to \chi_B$, and

$$\int_\Omega |\nabla u_n(x)|dx \to Per(A;\Omega) \quad \text{and} \quad \int_\Omega |\nabla v_n(x)|dx \to Per(B;\Omega) \tag{A.7}$$

as $n \to \infty$. Then, it is easy to check that $u_n \vee v_n := \max\{u_n, v_n\} \to \chi_{A\cup B}$ as $n \to \infty$, while $u_n \wedge v_n := \min\{u_n, v_n\} \to \chi_{A\cap B}$ as $n \to \infty$. We deduce, using (A.1), that

$$Per(A \cup B; \Omega) + Per(A \cap B; \Omega) \leq \liminf_{n\to\infty} \int_\Omega |\nabla(u_n \vee v_n)| + |\nabla(u_n \wedge v_n)| dx. \quad \text{(A.8)}$$

But for almost all $x \in \Omega$, $|\nabla(u_n \vee v_n)(x)| + |\nabla(u_n \wedge v_n)(x) = |\nabla u_n(x)| + |\nabla v_n(x)|$, so that (A.6) follows from (A.7) and (A.8). □

A.2.2 The reduced boundary, and a generalization of Green's formula

It is shown that if E is a set of finite perimeter in Ω, then the derivative D_{χ_E} can be expressed as

$$D_{\chi_E} = \nu_E(x)\mathcal{H}^{N-1} \llcorner \partial^* E \quad \text{(A.9)}$$

where $\nu_E(x)$ and $\partial^* E$ can be defined as follows: $\partial^* E$ is the set of points x where the "blow-up" sets

$$E_\epsilon = \{y \in B(0,1) : x + \epsilon y \in E\}$$

converge as $\epsilon \to 0$ to a semi-space $P_{\nu_E(x)} = \{y : y \cdot \nu_E(x) \geq 0\} \cap B(0,1)$ in $L^1(B(0,1))$, in the sense that their characteristic functions converge, or in other words

$$|E_\epsilon \backslash P_{\nu_E(x)}| + |P_{\nu_E(x)} \backslash E_\epsilon| \to 0$$

as $\epsilon \to 0$. Here $|E|$ denotes the Lebesgue measure of the set E. This definition of the boundary simultaneously defines also the (inner) normal vector $\nu_E(x)$.
The set $\partial^* E$ is called the *reduced boundary* of E (the "true" definition is a bit more precise, but still (A.9) is true with our definition, see [3, Chapter 3]).
Equation (A.9) means that for any C^1 vector field ϕ, one has

$$\int_\Omega \operatorname{div} \phi(x) dx = -\int_{\partial^* E} \phi \cdot \nu_E(x) d\mathcal{H}^{N-1}(x) \quad \text{(A.10)}$$

which is a sort of generalization of Green's formula to sets of finite perimeter.
This generalization is useful as shows the following example: let $x_n \in (0,1)^2$, $n \geq 1$, be the sequence of rational points (in $\mathrm{Q}^2 \cap (0,1)^2$), and let $E = \bigcup_{n\geq 1} B(x_n, \epsilon 2^{-n})$ for some ϵ fixed.
Then one sees that E is an open, dense set in $(0,1)^2$. In particular its "classical"
E (topological) bx

$\sum_n 2\pi\epsilon 2^{-n} = \pi\epsilon$. Its "reduced boundary" is, up to intersections (which are negligible), the set

$$\partial^* E \approx \bigcup_{n\geq 1} \partial B(x_n, \epsilon 2^{-n}).$$

One shows that this "reduced boundary" is always, as in this example, a *rectifiable set*, that is, a set which can be almost entirely covered with a countable union of C^1 hypersurfaces, up to a set of Hausdorff $\mathcal{H}^{N-1}$ measure zero: there exist $(\Gamma_i)_{i\geq 1}$, hypersurfaces of regularity C^1, such that

$$\partial^* E \subset \mathcal{N} \cup \left(\bigcup_{i=1}^{\infty} \Gamma_i \right), \ \mathcal{H}^{N-1}(\mathcal{N}) = 0. \tag{A.11}$$

In particular, $\mathcal{H}^{N-1}$-a.e., the normal $\nu_E(x)$ is a normal to the surfaces(s) Γ_i such that $x \in \Gamma_i$.

A.2.3 The isoperimetric inequality

For $u = \chi_E$, equation (A.4) becomes the celebrated isoperimetric inequality:

$$|E|^{\frac{N-1}{N}} \leq CPer(E) \tag{A.12}$$

for all finite perimeter set E of bounded volume, with the best constant C reached by balls:

$$C^{-1} = N(\omega_N)^{1/N}$$

where $\omega_N = |B(0,1)|$ is the volume of the ball in R^N.

A.2.4 The coarea formula

Theorem A.3. *Let $u \in BV(\Omega)$: then for a.e. $s \in \mathrm{R}$, the set $\{u > s\}$ is a finite perimeter set in Ω, and one has*

$$J(u) = \int_\Omega |Du| = \int_{-\infty}^{+\infty} Per(\{u > s\}; \Omega) ds. \tag{CA}$$

It means that the total variation of a function is also the accumulated surfaces of all its level sets. For the proof see [3, 24]. Let us observe that:

- It is relatively simple if $u = p \cdot x$ is an affine function, defined for instance on a simplex T (or in fact any open set). Indeed, in this case, $J(u) = |T||p|$, and $\partial\{u > s\}$ are hypersurfaces $\{p \cdot x = s\}$, and it is not too difficult to compute the integral $\int_{\mathrm{R}} \mathcal{H}^{N-1}(\{p \cdot x = s\}) ds$;

- For a general $u \in BV(\Omega)$, we can approximate u with piecewise affine functions u_n with $\int_\Omega |\nabla u_n| dx \to J(u)$. Indeed, one can first approximate u with the smooth functions provided by Theorem A.1, and then these smooth functions by piecewise affine functions using the standard finite elements theory. Then, we will obtain using (A.1) and Fatou's lemma that $\int_{\mathrm{R}} Per(\{u > s\}; \Omega) ds \leq J(u)$;

- The reverse inequality $J(u) \leq \int_{\mathrm{R}} Per(\{u > s\}; \Omega) ds = \int_{\mathrm{R}} J(\chi_{\{u>s\}}) ds$, can easily be deduced by noticing that if $\phi \in C_c^\infty(\Omega)$ with $\|\phi\| \leq 1$, one has $\int_\Omega \mathrm{div}\, \phi dx = 0$, so that (using Fubini's theorem)

$$\int_\Omega u \mathrm{div}\, \phi dx = \int_{\{u>0\}} \int_0^{u(x)} ds \mathrm{div}\, \phi(x) dx \; - \int_{\{u<0\}} \int_{u(x)}^0 ds \mathrm{div}\, \phi(x) dx \; =$$
$$\int_0^\infty \int_\Omega \chi_{\{u>s\}}(x) \mathrm{div}\, \phi(x)\, dx ds \; - \int_{-\infty}^0 \int_\Omega (1 - \chi_{\{u>s\}}(x)) \mathrm{div}\, \phi(x)\, dx ds \; =$$
$$\int_{-\infty}^\infty \int_{\{u>s\}} \mathrm{div}\, \phi(x)\, dx ds \leq \int_{-\infty}^\infty Per(\{u > s\}; \Omega) ds$$

  and taking the sup over all admissible ϕ's in the leftmost term.

Remark: observe that (A.6) also follows easily from (CA), indeed, let $u = \chi_A + \chi_B$, then $J(u) \leq J(\chi_A) + J(\chi_B) = Per(A; \Omega) + Per(B; \Omega)$, while for (CA) we get that

$$J(u) = \int_0^2 Per(\{\chi_A + \chi_B > s\}; \Omega) ds = Per(A \cup B; \Omega) + Per(A \cap B; \Omega).$$

A.3 The derivative of a BV function

We mention an essential result on the measure Du, defined for any $u \in BV(\Omega)$ by

$$\int \phi(x) \cdot Du(x) = - \int u(x) \mathrm{div}\, \phi(x)$$

for any smooth enough vector field ϕ with compact support. As mentioned in Section A.1.1, it is a bounded Radon measure. A derivation theorem due to Radon and Nikodym (and a refined version due to Besicovitch) shows that such a measure can be decomposed with respect to any positive Radon measure μ into:

$$Du = f(x) d\mu + \nu \tag{A.13}$$

where μ-a.e.

$$f(x) = \lim_{\rho \to 0} \frac{Du(B(x, \rho))}{\mu(B(x, \rho))}$$

(and in particular the theorem states that the limit exists a.e.), $f \in L^1_\mu(\Omega)$, that is, $\int_\Omega |f| d\mu < +\infty$, and $\nu \perp \mu$, which means that there exists a Borel set $E \subset \Omega$ such that $|\nu|(\Omega \backslash E) = 0$, $\mu(E) = 0$.

If the function $u \in W^{1,1}(\Omega)$, then $Du = \nabla u(x)dx$, with ∇u the "weak gradient" a vector-valued function in $L^1(\Omega; \mathrm{R}^N)$. Hence, the decomposition (A.13) with $\mu = dx$ (the Lebesgue measure), holds with $f = \nabla u$ and $\nu = 0$, and one says that Du is "absolutely continuous" with respect to Lebesgue's measure. This is not true anymore for a generic function $u \in BV(\Omega)$. One has

$$Du = \nabla u(x)dx + D^s u$$

where the *singular part* $D^s u$ vanishes if and only if $u \in W^{1,1}$, and $\nabla u \in L^1(\Omega; \mathrm{R}^N)$ is the "approximate gradient" of u.

The singular part can be further decomposed. Let us call J_u the *jump set* of u, defined as follows:

Definition A.4. *Given $u \in BV(\Omega)$, we say that $x \in J_u$, if and only if there exist $u_-(x), u_+(x) \in \mathrm{R}$ with $u_-(x) \neq u_+(x)$, and $\nu_u(x) \in \mathrm{R}^N$ a unit vector such that the functions, defined for $y \in B(0,1)$ for $\epsilon > 0$ small enough*

$$y \mapsto u(x + \epsilon y)$$

converge as $\epsilon \to 0$, in $L^1(B(0,1))$, to the function

$$y \mapsto u_-(x) + (u_+(x) - u_-(x))\chi_{\{y \cdot \nu_u(x) \geq 0\}}$$

which takes value $u_+(x)$ in the half space $\{y \cdot \nu_u(x) \geq 0\}$ and $u_-(x)$ in the other half space $\{y \cdot \nu_u(x) < 0\}$.

In particular this is consistent with our definition of $\partial^* E$ in Section A.2: $\partial^* E = J_{\chi_E}$, with $(\chi_+)(x) = 1$, $(\chi_-)(x) = 0$ and $\nu_{\chi_E}(x) = \nu_E$. The triple (u_-, u_+, ν_u) is almost unique: it is unique up to the permutation $(u_+, u_-, -\nu_u)$. For a scalar function u, the canonical choice is to take $u_+ > u_-$, whereas for vectorial BV functions, one must fix some arbitrary rule.

One can show that J_u is a rectifiable set, in fact, it is a countable union of rectifiable sets since one can always write

$$J_u \subseteq \bigcup_{n \neq m} \partial^* \{u > s_n\} \cap \partial^* \{u > s_m\},$$

for some countable, dense sequence $(s_n)_{n \geq 1}$: the jump set is where two different level sets meet.

One then has the following fundamental result:

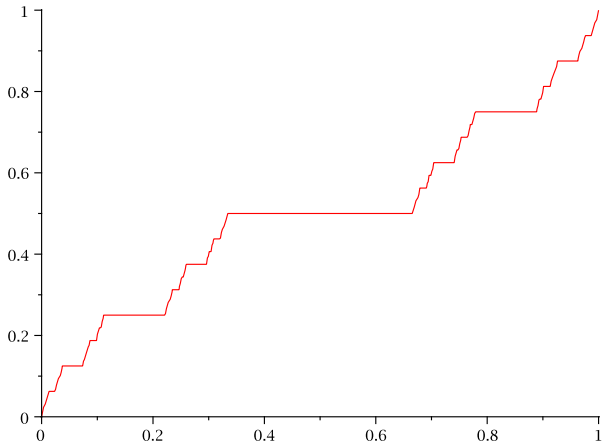

Figure A.2: *The "devil staircase" or Cantor-Vitali function.*

Theorem A.4 (Federer-Volpert)**.** *Let $u \in BV(\Omega)$: then one has*

$$Du = \nabla u(x)dx + Cu + (u_+(x) - u_-(x))\nu_u(x)d\mathcal{H}^{N-1} \llcorner J_u$$

where Cu is the "Cantor part" of Du, which is singular with respect to the Lebesgue measure, and vanishes on any set E with $\mathcal{H}^{N-1}(E) < +\infty$. In other words, for any $\phi \in C_c^1(\Omega; \mathrm{R}^N)$,

$$-\int_\Omega u(x)\mathrm{div}\,\phi(x)dx = \int_\Omega \nabla u(x)\cdot\phi(x)dx + \int_\Omega \phi(x)\cdot Cu(x) + \int_{J_u}(u_+(x)-u_-(x))\phi(x)\cdot\nu_u(x)dx. \tag{A.14}$$

Observe that (A.14) is a generalized version of (A.10).

As we have seen, an example of a function with absolutely continuous derivative is given by any function $u \in W^{1,1}(\Omega)$ (or more obviously $u \in C^1(\overline{\Omega})$).

An example of function with derivative a pure jump is given by $u = \chi_E$, E a Caccioppoli set (see Section A.2). A famous example of a function with derivative purely Cantorian is the Vitali-Cantor function, obtained as follows: $\Omega = (0,1)$ and we let $u_0(t) = t$, and for any $n \geq 0$,

$$u_{n+1}(t) = \begin{cases} \frac{1}{2}u_n(3t) & 0 \leq t \leq \frac{1}{3} \\ \frac{1}{2} & \frac{1}{3} \leq t \leq \frac{2}{3} \\ \frac{1}{2}(u_n(3t-2)+1) & \frac{2}{3} \leq t \leq 1 \end{cases}$$

Then, one checks that

$$\sup_{(0,1)} |u_{n+1} - u_n| = \frac{1}{2}\sup_{(0,1)} |u_n - u_{n-1}| = \frac{1}{2^n} \times \frac{1}{6}$$

so that $(u_n)_{n\geq 1}$ is a Cauchy sequence and converges uniformly to some function u. The function (see Figure A.2) is constant on each interval in the complement of the triadic Cantor set, which has zero measure in $(0,1)$. Hence, almost everywhere, its classical derivative exists and is zero. One can deduce that the derivative Du is singular with respect to Lebesgue's measure. On the other hand, it is continuous as a uniform limit of continuous functions, hence Du has no jump set. In fact, $Du = Cu$, which in this case, is the measure $\mathcal{H}^{\ln 2/\ln 3} \llcorner C / \mathcal{H}^{\ln 2/\ln 3}(C)$.

Appendix B

Details on the multigrid architecture

We describe here the main features of the adaptive mesh refinement technique that has been implemented in order to achieve three main results: optimized usage of available computing resources, better resolution of the liquid-solid interface (particularly useful for the modeling of the contact angle hysteresis), the possibility to resolve realistic asperities (micron sized pillars) on the solid surface.

Static refinement has been performed near the solid surface. Dynamic refinement is performed near the liquid-vapor interface, whose position is a-priori unknown, driven by the computed value of ϕ. We performed refinement over the computational nodes where $0.05 \leq \phi \leq 0.95$, at a decreasing frequency rate following the convergence of the gradient flow (see (2.11)).

Following [36] and [58], we used an interpolation technique preserving the second order accuracy of the finite difference approximation of the Laplacian across a level boundary. The Laplacian is then described through the fluxes of the phase function ϕ. In each coordinate direction, say x for simplicity, we put:

$$\left(\frac{\partial^2 \phi}{\partial x^2}\right)_i = \left(\delta\phi_{i+\frac{1}{2}} - \delta\phi_{i-\frac{1}{2}}\right)/h, \tag{A.1}$$

where h is as usual the grid spacing, and

$$\delta\phi_{i+\frac{1}{2}} = \frac{1}{h}\left(\phi_{i+1} - \phi_i\right) \tag{A.2}$$

$$\delta\phi_{i-\frac{1}{2}} = \frac{1}{h}\left(\phi_i - \phi_{i-1}\right). \tag{A.3}$$

Fluxes across the interfaces between areas of the computational domain at different size-grid level are computed using *ghost cells*: an extra-layer of nodes, placed along

the coarse-fine boundary regions, in which the ϕ values have to be calculated in a proper way (as we are going to explain) in order to use them in the seven-points stencil of "real" cells. In particular two cases are possible, depending on whether one considers a point on the coarse or on the fine part of the separation plane. Let us consider the first case (see fig. B.1). The requirement is that fluxes entering and exiting from the fine/coarse interface must balance, therefore one obtains:

$$\left(\frac{\partial^2\phi}{\partial x^2}\right)_i = \left(\delta\phi_{i+\frac{1}{2}} - \delta\phi^*_{i-\frac{1}{2}}\right)/h^c, \tag{A.4}$$

where

$$\delta\phi^*_{i-\frac{1}{2}} = \frac{1}{2}\left(\delta\phi^f_{up} + \delta\phi^f_{down}\right) \tag{A.5}$$

$$\delta\phi^f_{up/down} = \frac{1}{hf}\left(\phi^{triquad} - \phi^f\right). \tag{A.6}$$

The superscripts ^{c} and ^{f} refer to the coarse and fine quantities respectively. The label *triquad* denotes the fact that the ghost cells of the finer level are computed through a triquadratic (i.e. quadratic in each coordinate direction) interpolation as described in Figure B.1 and B.2.

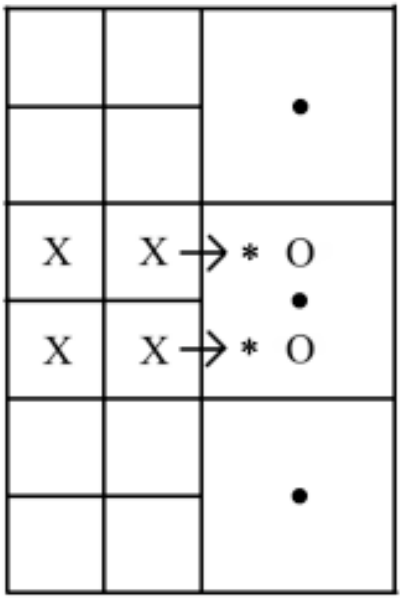

Figure B.1: *A 2D scheme for the interpolation across a coarse-fine boundary. The values corresponding to the positions labeled by O are obtained through quadratic interpolation applied to the values in the black points. These new values together with those in X positions are interpolated to produce the values in *, the ghost cells of this fine level. The arrows represents the top and bottom fluxes.*

In the second case the ghost cells can be used directly to compute the Laplacian for the finer level, because the triquadratic interpolation guarantees the desired accuracy. In particular places (such as corners), we obtain the same result repeating the procedure, but shifting the stencil for the interpolation as shown in fig. B.2.

The advantages of this method over the simple linear interpolation can be seen directly on the simulations: in the second case errors accumulate on the level interfaces and cannot be recovered. The following argument taken from [36], explains the superiority of quadratic interpolation, which guarantees second order accuracy. The finite difference approximation of the Laplacian implies a division by h^2, and so the accuracy of a p interpolation drops to h^{p-2} (for a quadratic interpolation it is known that $p = 3$). When this process is performed only in a set of codimension one (the interfaces), one order of accuracy is gained obtaining globally an error of $O(h^{p-1})$.

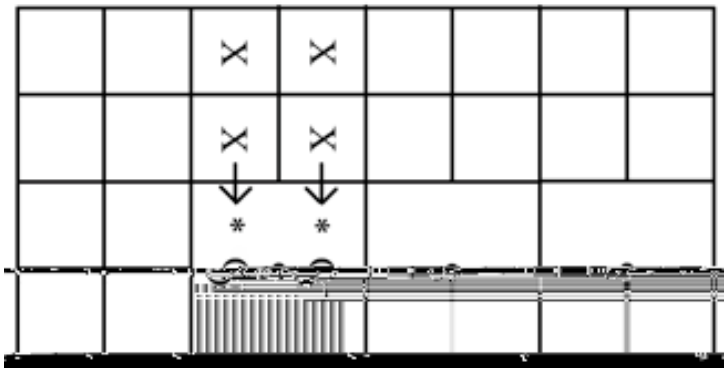

Figure B.2: *The stencil for the first interpolation is shifted in presence of a corner in the coarse-fine boundary.*

We recall that, in view of the stability estimate (2.12), the maximal stable time step decreases with the mesh size. Since time updating has to be synchronized across the various levels, this has the unpleasant consequence that we cannot advance the solution on the coarser area using the maximum dt allowed by (2.12), but we are forced to use the smaller dt that guarantees stability at the finer level.

Bibliography

[1] G. Alberti, A. DeSimone: *Wetting of rough surfaces: a homogenization approach*. Proc. R. Soc. A 461, 79–97, (2005)

[2] G. Alberti, A. DeSimone: *Quasistatic evolution of sessile drops and contact angle hysteresis*. Arch. Rat. Mech. Anal., in press (2011)

[3] l. Ambrosio, N. Fusco, D. Pallara: *Functions of bounded variation and free discontinuity problems*. The Clarendom Press Oxford University Press. New York, (2000)

[4] U. M. Ascher, S. J. Ruuth, B. Wetton: *Implicit-Explicit Methods for Partial Differential Equations*. SIAM J. Numer. Anal. 32, 797–823, (1995)

[5] V.E. Badalassi, H.D. Ceniceros, S. Banerjee: *Computation of multiphase systems with phase field models*. J. Comp. Phys. 190, 371–397, (2003)

[6] W. Bao, Q. Du: *Computing the ground state solution of Bose-Einstein condensates by a normalized gradient flow*. SIAM J. Sci. Comp. 25, No 5, 1674–1697, (2004)

[7] M. Berger, I. Rigoutsos: *An Algorithm for Point Clustering and Grid Generation*. IEEE Transactions Systems, Man and Cybernetics, 21 (5), 1278–1286, (1991)

[8] R.L. Burden, G.W. Hedstrom: *The distribution of the eigenvalues of the discrete Laplacian* BIT 12, 475–488, (1972)

[9] A. Braides: Γ-*convergence for Beginners*. Oxford Lecture series in Mathematics and its Applications 22 (2002)

[10] L. A. Caffarelli: *The obstacle problem revisited*, J. Fourier Anal. Appl., Volume 4, 383–402, (1998)

[11] L. Caffarelli, A. Mellet: *Capillary Drops: contact angle hysteresis and sticking drops*. Calc. Var. PDE 29, 141–160, (2007)

[12] A. Carre, M. E. R. Shanahan: *Drop motion on an inclined plane and evaluation of hydrophobic treatments to glass*. J. Adhesion 49, 177–185 (1995)

[13] M. Callies, D. Quéré: *On water repellency*. Soft Matter 1, 55–61, (2005)

[14] H. Ceniceros, A. Roma: *A non stiff, adaptive mesh refinement-based methodfor the Cahn-Hilliard equation*. J. Comput. Phys, 225(2), 1849–1862, 2007.

[15] A. Chambolle, V. Caselles, M. Novaga, D. Cremers, T. Pock: *An introduction to Total Variation for Image Analysis*. Radon Series Comp. Appl. Math. 9, 1–78, ©De Gruyter, (2010)

[16] P.-G. De Gennes, F. Brochard-Wyart, D. Quéré: *Capillarity and Wetting Phenomena: Drops, Bubbles, Pearls, Waves*, Springer, (2004)

[17] J.E. Dennis JR., R. B. Schnabel: *Numerical methods for Unconstrained Optimization and Nonlinear Equations*, 1983 by Prentice-Hall, Inc, Englewood Cliffs, New Jersey 07632

[18] A. DeSimone, L. Fedeli, A. Turco: *A phase field approach to wetting and contact angle hysteresis phenomena*. IUTAM Symposium on Variational Concepts with Applications to the Mechanics of Materials, K. Hackl (ed.), IUTAM Bookseries 21, 51–63, Springer Science + Business Media B.V., (2010)

[19] A. DeSimone, N. Grunewald, F. Otto: *A new model for contact angle hysteresis*. Networks and Heterogeneous Media 2, 211–225, (2007)

[20] P. Deufflhard: *Newton Methods for Nonlinear Problems*. Springer Series in Computational Mathematics, Springer-Verlag Berlin heidelberg (2004)

[21] E. B. Dussan: *On the ability of drops or bubbles to stick to non-horizontal surfaces of solids*. J. Fluid Mech. 151, 1–20, (1985)

[22] J. Eckstein, D. P. Bertsekas: *On the Douglas-Rachford splitting method and the proximal point algorithm for maximal monotone operators*, Math. Programming, Volume 55, (1992)

[23] E. Esser: *Applications of Lagrangian-Based Alternating Direction Methods and Connections to Split Bergman*, (2009)

[24] L. C. Evans, R. F. Gariepy: *Measure theory and fine properties of functions.* CRC Press, Boca Raton, FL, 1992

[25] H. Federer:*Geometric measure theory.* Springer-Verlag New York Inc., New York, (1969)

[26] R. Finn: *Equilibrium Capillary Surfaces*, Springer, (1986)

[27] R. Finn; *Some properties of capillary surfaces*, Milan J. Math., Volume 70, 1–23, (2002)

[28] H. Garcke, B. Nestler, B. Stoth: *A multi-phase-field concept: numerical simulations of moving phase boundaries and multiple junctions*. SIAM J. Appl. Math. 60, 295–315, (1999)

[29] H. Hemmerich. *The diffuse interface approach in Material Science. Thermodynamic concepts and applications of phase-field models.* Springer-Verlag Berlin Heidelberg, (2003)

[30] D. Jamet, O. Lebaigue, N. Coutris and J.M. Delhaye: *The second gradient method for the direct numerical simulation of liquid-vapor flows with phase change.* J. Comp. Phys. 169, 624–651, (2001)

[31] T. Koishi, K. Yasuokac, S. Fujikawab, T. Ebisuzakid, X. Zenge: *Coexistence and transition between Cassie and Wenzel state on pillared hydrophobic surface.* Proc. Nat. Acad. Science U.S.A 106, 8435–8440, (2009)

[32] A. Lafuma, D. Quéré: *Superhydrophobic states.* Nature Materials 2, 457–460, (2003)

[33] P. Germain, Q.S. Nguyen and P. Suquet: *Continuum Thermodynamics.* ASME Trans. J. Appl. Mech. 105, 1010-1020, (1983)

[34] L. Lapidus, G. F. Pinder: *Numerical Solution of Partial Differential equations in Science and Engineering*, Wiley, (1982)

[35] P.L. Lions, B. Mercier: *Splitting Algorithms for the Sum of Two Nonlinear Operators*, SIAM Journal on Numerical Analysis, Volume 16, 964–979, (1979)

[36] D. F. Martin, K. L. Cartwright: *Solving Poisson's Equation using Adaptive Mesh Refinement.* Technical Report M96/66 Univ. of California, Berkeley Electronic Research Lab, (1996)

[37] G.A. Maugin: *The Thermomechanics of Plasticty and Fracture.* Cambridge University Press, (1992)

[38] S. F. McCormick: *Multilevel Adaptive Methods for Partial Differential Equations.* SIAM, Philadelphia, PA (1989)

[39] N. Meyers, J. Serrin: $H = W$. Proc. Nat. Acad. Sci. USA, 51: 1055–1056, (1964)

[40] A. Mielke: *Evolution of rate-independent systems.* Handbook of differential equations. Evolutionary equations. Vol. II, 461-559, Edited by C.M. Dafermos and E. Fereisl. (2005)

[41] L. Modica: *Gradient Theory of phase transition with boundary contact energy.* Ann. Inst. H. Poincaré Anal. Non Linéaire 5, 497 (1987)

[42] J. M. Ortega, W. C. Rheinboldt; *Iterative Solution of Nonlinear Equations in Several Variabless.* Academic Press, New York and London (1970)

[43] M. Pernice, R. D. Hornung: *Newton-Krylov-FAC methods for problems discretized on locally refined grids.* Comput. Visual Sci. 8(2), 107–118, (2005)

[44] L.M. Pismen and Y. Pomeau: *Disjoining potential and spreading of thin liquid layers in the diffuse-interface model coupled to hydrodynamics.* Phys. Rev. E 62, (2000)

[45] *Consistency, stability, a priori and a posteriori errors for Petrov-Galerkin methods applied to nonlinear problems.* Numer. Math. 69: 213–231 (1994)

[46] T. Qian, X. Wang and P. Shieng: *A variational approach to moving contact line hydrodynamics.* J. Fluid Mech. 564, 333-360, (2006)

[47] D. Quéré: *Wetting and Roughness.* Annu. Rev. Mater. Res. 38, 71–99, (2008)

[48] J.S. Rowlinson, B. Widom: *Molecular Theory of Capillarity*, Dover Edition, (2002)

[49] Y. Saad: *Iterative Methods for Sparse Linear Systems.* 2nd Edition, SIAM, (2003)

[50] S. Schaffer: *A Semicoarsening multigrid method for elliptic partial differential equations with highly discontinuous and anisotropic coeffcients.* SIAM, J. Sci. Comput., Vol 20, No 1, 228–242 (1998)

[51] P. Seppecher: *Moving contact lines in the Cahn-Hilliard theory*. Int. J. Engng. Sci. 34, 977–992, (1996)

[52] J.C. Simo and T.J.R. Hughes: *Computational Inelasticity*. Springer-Verlag, (1998)

[53] J. C. Strikwerda: *Finite Difference Schemes and PDE*, SIAM (2004)

[54] J. E. Taylor: *Boundary regularity for solutions to various capillarity and free boundary problems*, Comm. Partial Differential Equations, Volume 2, 323–357, (1977)

[55] B. Torby: *Energy Methods.* Advanced Dynamics for Engineers. HRW Series in Mechanical Engineering. United States of America, CBS College Publishing.

[56] A. Turco, F. Alouges, A. DeSimone: *Wetting on rough surfaces and contact angle hysteresis: numerical experiments based on a phase field model*. ESAIM: M2AN 43, 1027–1044, (2009)

[57] A. Turco: PhD Thesis *http://digitallibrary.sissa.it/handle/1963/3405*

[58] S. Wise, J. Kim, J. Lowengrub: *Solving the regularized, strongly anisotropic Cahn-Hilliard equation by an adaptive nonlinear multigrid method*. J. Comput. Phys. 226, 414–446, (2007)

[59] SAMRAI, Structure Adaptive Mesh Refinement Application Infrastructure, *https://computation.llnl.gov/casc/SAMRAI/*

[60] H. Yang, A. Buguin, J.M. Taulemesse, K. Kaneko, S. Mery, A. Bergeret, P. Keller: *Micron-Sized Main-Chain Liquid Crystalline Elastomer Actuators with Ultralarge Amplitude Contractions*, J. Am. Chem. Soc.,131 (41), 1500015004, (2009)